Classical Particle Simulations with the PSC code

Hartmut Ruhl,
RUB
Bochum, Germany

An introduction into the PSC

Contents

Chapter 1

Synopsis

The intent of this chapter is a self-contained presentation of recent advances in the field of intense laser-plasma interaction via particle simulations. The numerical tool provided is the Plasma Simulation Code (PSC), which is available as an open source software. See section 8 for more details. Since it is the intent of this chapter to introduce into the fascinating new capabilities of classical particle simulations, we have refrained from the idea of providing elaborate benchmarking simulations with other codes as well as consistency and accuracy tests for the PSC. We refer the interested reader to the PSC web-site at http://www.THE-PSC.com, where extensive test results are provided.

The numerical methods applied in the field represent the most important aspect of this chapter. Hence, we have decided to explain the standard numerical methods in the field of laser-plasmas in some detail. The same methods are also employed in the PSC. The interested reader can find further information in the literature cited in section 4.

The power of modern simulation tools is best illustrated with the help of examples that represent state of the art problems in the field. Some of these problems are the generation of energetic electrons and ions with the help of the radiation field of the laser, strong quasi-steady electric and magnetic fields, large currents and energy flows, and the conversion of the irradiated laser energy into collective and collisional plasma heating. Since most of the addressed topics are highly non-linear, excessive use of computer simulations has been made early on in the field. The standard numerical method are classical particle simulations as described in this chapter. It is the hope that this text can provide a useful introduction into the numerical methods applied in the field and raise interest in the physics of intense laser-matter interaction.

The chapter is structured as follows: Section 2 gives an introduction into the field of intense laser plasma physics. Section 3 states the governing equations of intense laser-plasma interaction, which are the Vlasov-Boltzmann equations combined with Maxwell's equations in three spatial and momentum dimensions. Section 4 describes the numerical schemes that are used in the PSC to solve Maxwell's equations, the Vlasov equations, and the Vlasov-Boltzmann equations. The concept of quasi-particles is introduced. The numerical collision model is outlined. Section 5 explains details of the PSC and the required run-time environment for the code. Section 6 is devoted to an introduction into basic phenomena of non-linear plasma optics and intense laser-matter interaction. Important physics issues of intense laser beam propagation through an under-critical plasma are investigated. The physics of intense laser absorption in a sharp-edged plasma is reviewed. For selected problems computer simulations with the PSC are presented. A detailed description of the setup of the PSC is given for each example. Copies of the source code for the simulated examples

are provided at the PSC web-site at http://www.THE-PSC.com. Section 7 summarizes the most important aspects of this chapter. Section 8 discusses the intent and present status of the open source project PSC.

Chapter 2

Introduction

The science of intense laser-matter interaction is a rapidly progressing field in modern physics and optical technology. Over the last three decades laser peak power and intensity have made extreme progress due to a number of technological breakthroughs [1]. Two important ones are mode-locking and the chirped pulse amplification scheme of the laser radiation [2]. Chirped pulse amplification makes use of dispersive beam delay lines which stretch the laser radiation in time. Amplification and final compression of the radiation yields high intensity gains. High power laser media used today are KrF with the wavelength $\lambda = 0.248$ μm, Ti:Sapphire with $\lambda = 0.84$ μm, Nd:Glass with $\lambda = 1.053$ μm, and CO_2 with $\lambda = 10.6$ μm. Details of intense radiation generation and related issues are given in [1, 3, 4].

Peak intensities reached by present day lasers are in the range of $I = 10^{21}$ Wcm^{-2}. The electric field at this laser intensity is of the order of 10^{14} V/m and thus significantly exceeds the field strength felt by an electron in atoms which is only $E_{au} = 5.0 \cdot 10^{11}$ V/m in the ground state of hydrogen. Hence, the barrier suppression threshold I_{BSI} [5] for outer electrons is exceeded and rapid field ionization takes place. The electrons of the plasma can be accelerated to relativistic energies by the laser field. As soon as the kinetic energy of the electrons exceeds the ionization barrier ϵ_I of bound electrons the matter will be further ionized by collisions [6]. Simultaneously collisional heating and heat transport take place. While at moderate laser intensities both can be described, with limitations, by formulas derived by Spitzer [7] and Braginskii [8], they pose open questions for ultra-high laser irradiation for which the electron mean free path exceeds the depth of the heat front in the plasma obtained from Spitzer theory. Transport at ultra-high irradiation is presently subject to intense investigations [9, 10, 11, 12, 13, 14]. In this regime classical collective plasma excitations and collision-less processes become important and may eventually dominate the laser-matter interaction.

Intense laser radiation brings novel applications within reach. One is particle acceleration to high energies on short spatial scales in wakefields [15]. Others are fast ion generation in exploding atomic clusters [16] and laser generated space charge fields [17], nuclear reactions [18, 19, 20, 21], brilliant ultra-short X-ray sources [22], the generation of high harmonics [23, 24, 25], fast ignition of nuclear fusion targets by anomalous transport in laser plasmas [26], the generation of positrons [27], and experimental plasma astrophysics [28, 29, 30], to mention a few.

Let us consider the most important set of laser-plasma parameters that characterize laser-plasma properties. The first is the ratio of the plasma density n to the laser critical density n_c. If the plasma density is equal to the critical density the laser frequency ω is equal to the electron plasma frequency $\omega_p = (e^2 n/\epsilon_0 m_e)^{1/2}$, where e denotes the electron charge and

m_e the electron mass. This means that $\omega_p/\omega = (n/n_c)^{1/2}$ holds. A plasma with $\omega_p/\omega < 1$ is called under-critical or under-dense. This plasma is transparent for the laser radiation. Depending on the plasma density the group velocity $v_g = \partial\omega/\partial k$ of the laser radiation can be close to the speed of light c. Plasma with $\omega_p/\omega > 1$ is called over-critical or over-dense. The laser radiation cannot penetrate deeply into over-dense plasma. The penetration depth is approximately the classical skin length $l_s = c/\omega_p$. The second parameter of relevance in a plasma is the dimensionless amplitude a of the laser field. It is defined by $a = v_{os}/c$, where v_{os} is the electron oscillation velocity given by $v_{os} = eE_0/m_e\omega$. The quantity E_0 denotes the vacuum field strength of the laser radiation. The quantity a characterizes relativistic plasma effects. Finally, the third parameter is the ratio v_{th}/c characterizing the initial plasma temperature, where v_{th} denotes the thermal velocity $v_{th} = (k_B T_e/m_e)^{1/2}$ and T_e is the plasma temperature. The parameters mentioned above describe the collective properties of a plasma, i.e. the coherent response of the plasma to applied electric and magnetic fields. Additional parameters become important if non-collective plasma properties are essential, e.g. collisions.

The value of a that characterizes the onset of relativistic effects in laser plasma is obtained by solving the equations of motion for an electron interacting with a linearly polarized plane electromagnetic wave. We find for an electron that is at rest before the wave arrives [31]

$$\epsilon = \frac{1}{2} m_e c^2 a^2 , \qquad \vec{p}_\perp = m_e c\, \vec{a}_\perp , \qquad p_\parallel = \frac{1}{2} m_e c\, a^2 , \tag{2.1}$$

where ϵ is the electron energy, $\vec{p}_\perp$ the momentum normal to the propagation direction of the wave, $\vec{p}_\parallel$ the momentum in propagation direction, and $\vec{a}_\perp = e\vec{A}_\perp/m_e\, c$. The quantity $\vec{A}_\perp$ is given by $\vec{A}_\perp = \vec{E}_\perp/\omega$. For $a > 2$ the electron energy exceeds the electron rest mass. For this case the electron motion in the wave is relativistic. It is seen that the longitudinal momentum $p_\parallel$ becomes larger than the lateral momentum $p_\perp$ for $a > 2$. Laser intensities are called relativistic if the dimensionless amplitude a exceeds unity. For intensities of $I = 10^{21}$ Wcm^{-2} the dimensionless amplitude is $a \approx 27$. For ultra-intense laser radiation the ratio ω_p/ω has to be corrected. For circular polarization it becomes $\omega_p/\omega = (n/\gamma n_c)^{1/2}$, where $\gamma = (1 + a^2)^{1/2}$ holds.

Prominent features of nonlinear optics in a laser plasma at high intensities are relativistic self-focusing and magnetic guiding of the laser radiation. Relativistic self-focusing has been first described by Askar'yan [32]. Magnetic self-guiding has been described by [33]. The origin of relativistic self-focusing is a nonlinear change of the refractive index η of the plasma due to the relativistic mass gain of the oscillating electrons in the intense laser field. In addition, the plasma density n is modified by the ponderomotive force of the laser radiation. The power threshold for relativistic self-focusing is given by [34, 35, 36]

$$P_c = \frac{2m_e^2 c^5 \omega^2}{e^2 \omega_p^2} \approx 17\, \frac{\omega^2}{\omega_p^2}\ \text{GW} . \tag{2.2}$$

The criterion (2.2) is valid for laser beams but not for short laser pulses. Since the threshold for relativistic self-focusing is a power threshold the laser beam can split into filaments in case the laser power exceeds the critical power significantly [37, 38]. Simulations of intense laser beam propagation through under-critical plasma show that relativistic self-focusing can enhance the laser intensity ten-fold. In addition, the focused beam is asymmetric in the plane normal to the direction of propagation. Electrons accelerated inside the laser beam generate currents that lead to a quasi-steady magnetic field due to

$$\vec{\nabla} \times \vec{B} = -\frac{en}{\epsilon_0 c^2}\, \vec{v} , \tag{2.3}$$

where v denotes the fluid velocity of the electrons and where it has been assumed that there is no contribution from the ion background in the plasma. The essence of magnetic self-guiding is that the electrons interact with the magnetic field leading to modifications of the refractive index which in turn is capable of enhancing laser beam energy transport.

In addition to relativistic self-focusing other nonlinear plasma optical phenomena can be observed at high intensities. One is laser beam self-modulation for sufficiently long laser pulses [39, 40, 41, 42, 43]. Laser beam self-modulation is an instability that redistributes the laser energy in longitudinal as well as lateral beam directions. The modulation length of the instability is $2\pi/k_p = 2\pi c/\omega_p$. The origin of laser beam self-modulation is stimulated Raman forward-scattering. Raman scattering is one of the fastest plasma instabilities [44]. Laser self-modulation due to Raman forward scattering plays an important role for laser wakefield acceleration [45, 46, 47].

While long intense laser pulses in under-dense plasma self-modulate due to the Raman instability ultra-short laser pulses in under-critical plasma generate wakefields in a classical sense. These are collective plasma excitations that occur in the wake of the short laser pulse. For sufficiently low intensities a perturbation analysis demonstrates the essence of the wakefield mechanism. We assume that the laser pulse represented by a_p propagates with the group velocity v_g. The plasma considered is cold. In one spatial dimension we immediately write from fluid equations [44]

$$\begin{aligned} \partial_t \delta n_e &= -n_e \partial_x v_x \ , \\ \partial_t v_x &= -\frac{e}{m_e} E_x + a_p - \nu v_x \ , \\ \partial_x E_x &= -\frac{e}{\epsilon_0} \delta n_e \ , \end{aligned} \tag{2.4}$$

where $a_p = a_p(x - v_g t)$. To account for plasma damping the collision frequency ν has been introduced. Solving for the density perturbation yields

$$\delta n_e(x,t) = -i n_e \int d\omega \ \frac{\omega}{v_g^2} \ a_p\left(\frac{\omega}{v_g}\right) \ \frac{e^{i\frac{\omega}{v_g}[x - v_g t]}}{(\omega - \omega_p + i0.5\ \nu)\,(\omega + \omega_p + i0.5\ \nu)} \ . \tag{2.5}$$

From δn_e the electrostatic wakefield is obtained. The phase velocity of the wakefield is the group velocity of the laser pulse which is close to c. Hence, wakefields can in principal be used to accelerate electrons to high energies. That wakefields are indeed capable of accelerating electrons is shown with the help of kinetic simulations. In case large numbers of accelerated electrons become faster than the phase velocity of the wakefield wave-breaking sets in. Wakefield generation in more than one dimension is accompanied by magnetic field generation due to the electron current in the wakefield [48]. According to (2.3) magnetic fields generated by laser induced electron currents may be associated with fluid vortices given by

$$\vec{\nabla} \times \vec{v} \approx \frac{\epsilon_0 c^2}{en} \ \Delta \vec{B} \ . \tag{2.6}$$

The vortices in the fluid, in the electrostatic wakefield, and in the magnetic field propagate and decay very slowly. They remain in the plasma for a long time after the laser pulse has left the plasma already [49].

While laser radiation can propagate in plasma if $\omega_p/\omega < 1$ holds it decays over a length comparable with the collision-less skin length l_s if $\omega_p/\omega > 1$ holds. If the radiation pressure $P_I = I/c$ of the laser pulse exceeds the thermal pressure $P_{th} = n k_B T_e$ of the plasma the

density profile at the critical density is steepened leading to a sharp boundary. If the duration of the laser irradiation is sufficiently long a shock front is generated [9] and laser hole boring sets in [50]. At high intensities the shock velocity v_s is mainly related to the radiation pressure P_I. It is approximately given by

$$v_s = \sqrt{\frac{\kappa}{\kappa - 1}\ (1+R)\ \frac{I}{c\rho_i}}\ , \tag{2.7}$$

where ρ_i denotes the ion mass density, R the reflection coefficient for the laser radiation, and κ the shock compression [51].

One important aspect of intense laser-plasma interaction is the absorption of laser energy, a complex and highly nonlinear process. Many of the applications mentioned previously rely on high energy deposition and well-behaved energy transport in many times over-critical plasma. In order to address laser absorption in solid targets Price *et al.* [52] performed absorption measurements for a variety of target materials. Their findings were that collisional absorption was needed to explain the experimental data below an intensity of $I = 10^{17}$ Wcm^{-2} since different target material gave different absorption. However, for $I > 10^{17}$ Wcm^{-2} absorption became universal in the sense that it did not depend significantly on the target material anymore. The fraction of laser light absorbed was about 10%. Their interpretation for this observation was a reduction of collisions in the plasma due to plasma heating. Theoretical investigations by Rozmus *et al.* [53] support this viewpoint. However, absorption obtained in solid targets with more intense laser radiation was found to be much higher than 10%. One of the many experiments is reported in [54]. In an effort to explain these observations Wilks *et al.* investigated absorption properties of plasma in more than one spatial dimension with the help of numerical simulations. They found good absorption. Parametric studies of deformed plasma films showed that good absorption is associated with plasma-interface deformation [9]. In order to describe absorption in over-critical plasma the gradient length $L = n/|\vec{\nabla} n|$ of the plasma interface at the critical surface and parameters characterizing target geometry have to be introduced. Knowing the direction of the density gradient the relative orientation of the laser polarization with respect to the plane spanned by the pulse propagation direction and the density gradient can be defined. If the polarization is normal to this plane the laser light is called p-polarized. In the other case it is s-polarized.

On a general basis three different regimes of collision-less collective laser absorption in over-critical plasma can be distinguished. The first is resonance absorption. Resonance absorption relies on resonantly excited plasma oscillations at the critical density for sufficiently long density gradients L [55, 56, 57]. The plasma oscillations at the critical surface excite plasma waves that can carry laser energy away. The second are plasma interface oscillations at steep plasma gradients called vacuum heating or not-so-resonant resonance absorption in literature [25, 58, 59, 60, 61]. Here, plasma electrons pulled out of the critical surface by the laser radiation are accelerated and eventually reenter the plasma. This way they loose their phase relation with the laser driver and absorb laser energy. Collective plasma motion as well as single particle aspects play a role in this regime. Finally anomalous skin absorption or the anomalous skin effect has to be mentioned. The original idea dates back to Weibel [62]. Skin absorption is a purely kinetic effect unlike the other regimes mentioned. Its contribution to absorption is quite small for typical parameters of a laser plasma. Another purely kinetic effect believed to have some impact on absorption is $\vec{j} \times \vec{B}$-heating [63]. The essence of both absorption mechanisms is non-adiabaticity in a skin layer of length l_s. The anomalous skin effect proposed by Weibel [62] contributes to absorption if the mean passage time of an electron through the skin layer of depth l_s is smaller than the laser cycle time.

This means $v_{th}/(l_s\omega) > 1$. Electrons subject to $\vec{j} \times \vec{B}$-heating [63] are believed to loose their phase relation with the driver due to ponderomotive acceleration.

The general observation is that collective non-kinetic plasma excitations are at the origin of effective high laser absorption. In planar targets only a few of these modes can be excited due to limitations from geometry. In addition, it has been observed that at high laser intensities absorption drops in planar targets [58, 61]. The explanation for this seems to be a further suppression of collective plasma oscillations. The situation is quite different for interaction regimes with more spatial degrees of freedom. Absorption in that case is high and robust. It only weakly depends on laser intensity [9, 54].

Ultimately, high laser absorption cannot be understood without transport properties of the laser plasma since both feed back on each other. Transport in laser plasma is a highly non-linear process. The question arises how energetic electrons generated in the ponderomotively steepened critical plasma interface penetrate into the bulk plasma. The relevant physical issues are return current generation, return current inhibition [14], and magnetic field generation [64, 65, 66, 67, 68, 69]. The need for return current generation in bulk plasma can be understood from energy balance considerations [14]. The reasoning is simple. Under the assumption that the absorbed laser energy is converted into fast electrons that propagate into the plasma a magnetic field is generated. The total energy of the latter could easily exceed the absorbed laser energy without a return current [14]. The presence of the return current limits the magnetic field strength to values consistent with energy conservation. Furthermore, only due to return current generation transport of high energy currents in the plasma is possible. However, there is a second limitation known as the Alfven current limit $I_A = 17000\,\beta_A\gamma_A$ [A], where $\beta_A = v/c$, $\gamma_A = 1/(1-\beta_A^2)^{1/2}$, and v denotes the velocity of the flow in the electron current filament. The current limit I_A is obtained from the requirement that electrons in the current filament are not allowed to turn around inside the current filament due to their gyro-motion. It is an open question at present what the impact of the Alfven current limit on transport is [9, 12, 13].

Since temperatures of intense laser generated plasma are typically very high quantum correlations can be mostly neglected. Hence, the physics of laser-plasma interaction is described by classical nonlinear transport equations coupled with Maxwell fields to very good accuracy. The extremely non-linear nature of most of the phenomena involved in intense laser-matter interaction and their mutual feed-back hardly allow analytical treatment. However, due to the advent of novel numerical schemes, due to the development of complex computer codes that include most aspects of super-intense laser-plasma interaction, and finally due to massively parallel high power computing platforms further progress is possible. Computer simulations performed in the field of kinetic plasma transport as presented in this text belong to the largest simulations in the field and are mostly based on classical particle methods.

Chapter 3

The physics model

Intense laser radiation interacting with matter at relativistic intensities ($a > 1$) is capable of generating plasma far away from equilibrium. A promising approach to describe the non-linear, kinetic nature of the interaction are plasma models based on the fully relativistic Vlasov-Boltzmann equations combined with Maxwell's equations. Details are introduced in the following sections.

3.1 Governing equations

We consider a plasma consisting of electrons and ions, which are represented by distribution functions $f_k(\vec{x}, \vec{p}, t)$. The distribution functions f_k give the probability of finding particles os sort k in a given volume of phase space. We assume that the electrons and ions in the plasma under consideration interact via electromagnetic radiation and binary collisions. Hence, an appropriate description of the plasma is based on the following set of transport equations, which for brevity are stated in covariant form [70]

$$p_k^\mu \frac{\partial f_k}{\partial x^\mu} + m_k F_k^\mu \frac{\partial f_k}{\partial p_k^\mu} = \sum_{l=n,e,i} \int \frac{d^3 p_l}{p_l^0} F_{kl} \int d\Omega_\psi \, \sigma^{kl}(s,\psi) \, \left(f_k^{'} f_l^{'} - f_k f_l \right) . \quad (3.1)$$

The quantity $d\Omega_\psi$ is an element of solid angle between $\vec{p}_k^{\,'}$ and $\vec{p}_k$ and $\sigma^{kl}(s,\psi)$ denotes the invariant cross section. The relative velocity between particles k and l is given by

$$v_{kl} = \frac{c F_{kl}}{p_k^0 p_l^0} = \sqrt{(\vec{v}_k - \vec{v}_l)^2 - \frac{1}{c^2} (\vec{v}_k \times \vec{v}_l)^2} . \quad (3.2)$$

The force on the charged particles in the plasma is the Lorentz force given by

$$F_k^\mu = \frac{q_k}{m_k c} F^{\mu\nu} p_{k\nu} . \quad (3.3)$$

Maxwell's equations are represented as

$$\frac{\partial}{\partial x^\mu} F^{\mu\nu} = \frac{j^\nu}{c\epsilon_0} , \qquad \frac{\partial}{\partial x^\mu} \tilde{F}^{\mu\nu} = 0 , \quad (3.4)$$

where

$$j^\nu = \sum_{k=n,e,i} q_k \int d^4 p \, 2\Theta(p_0) \, \delta(p^2 - m_k^2 c^2) \, c p^\nu \, f_k . \quad (3.5)$$

Equivalently, Eqn. (3.1) can be rewritten in three vector notation

$$\left(\partial_t + \vec{v}_k\partial_{\vec{x}} + q_k\left[\vec{E} + \vec{v}_k \times \vec{B}\right]\partial_{\vec{p}_k}\right)\ f_k \qquad (3.6)$$
$$= \sum_{l=n,e,i}\int d^3p_l\ v_{kl}\ \int d\Omega_\psi\ \sigma^{kl}(s,\psi)\ \left(f_k^{'}f_l^{'} - f_kf_l\right)\ .$$

Maxwell equations become

$$\partial_t\vec{E} = c^2\vec{\nabla}\times\vec{B} - \vec{j}/\epsilon_0\ , \qquad (3.7)$$
$$\partial_t\vec{B} = -\vec{\nabla}\times\vec{E}\ , \qquad (3.8)$$
$$\partial_t\rho = -\vec{\nabla}\cdot\vec{j}\ . \qquad (3.9)$$

The charge and current densities in three notation are given by

$$\rho = q_e\int d^3p_e f_e + q_i\int d^3p_i f_i\ , \qquad (3.10)$$
$$\vec{j} = q_e\int d^3p_e\vec{v}_e f_e + q_i\int d^3p_i\vec{v}_i f_i\ .$$

3.2 The Boltzmann collision operator

For binary scattering events we obtain [70]

$$C_{kl} = \int\frac{d^3p_l}{p_l^0}\int\frac{d^3p_k^{'}}{p_k^{0\,'}}\int\frac{d^3p_l^{'}}{p_l^{0\,'}}\ \left(W_{klk'l'}\ f_k^{'}f_l^{'} - W_{k'l'kl}\ f_kf_l\right)\ , \qquad (3.11)$$

where the transition amplitude is given by

$$W_{k'l'kl} = \frac{e_k^2e_l^2m_k^2m_l^2c^2}{4\pi^2\epsilon_0^2}\ |M_{k'l'kl}|^2\ \delta^4\left(p_k^{'} + p_l^{'} - p_k - p_l\right) \qquad (3.12)$$
$$= s\,\sigma^{kl}(s,\psi)\,\delta^4\left(p_k^{'} + p_l^{'} - p_k - p_l\right)$$

with the invariant cross section

$$\sigma^{kl}(s,\psi) = \frac{e_k^2e_l^2m_k^2m_l^2c^2}{4\pi^2\epsilon_0^2\,s}\ |M_{k'l'kl}|^2\ , \qquad (3.13)$$

where $s = p_t^2$ and $p_t = p_k + p_l$. The quantities p_k and p_l are the pre-collisional momenta whereas $p_k^{'}$ and $p_l^{'}$ denote the post-collisional momenta. The binary transition matrix elements are denoted by $|M_{k'l'kl}|$.

Introducing Equation (3.12) into Equation (3.11) and integrating over $\vec{p}_l^{\,'}$ we obtain $\vec{p}_l^{\,'} = \vec{p}_t - \vec{p}_k^{\,'}$. Since the final momentum $p_l^{'}$ has to be on the mass shell we find $(p_t - p_k^{'})^2 = m_l^2c^2$ from which we obtain $s + (m_k^2 - m_l^2)c^2 = 2p_k^{'}\cdot p_t$. The quantities m_k and m_l are the pre-collision rest masses of the colliding particles. We find

$$\delta\left(p_k^{0\,'} + p_l^{0\,'} - p_k^0 - p_l^0\right) = \frac{p_k^{0\,'}p_l^{0\,'}}{p_t^0|\vec{p}_k^{\,'}| - |\vec{p}_t|p_k^{0\,'}\cos\psi}\ \delta\left(|\vec{p}_k^{\,'}| - \mathcal{F}_{kl}\right)\ , \qquad (3.14)$$

where

$$\mathcal{F}_{kl} = \frac{\mathcal{I}\ |\vec{p}_t|\cos\psi}{2\left(s + \vec{p}_t^{\,2}\sin^2\psi\right)} + \sqrt{\left(\frac{\mathcal{I}\ |\vec{p}_t|\cos\psi}{2\left(s + \vec{p}_t^{\,2}\sin^2\psi\right)}\right)^2 + \frac{\mathcal{I}^2 - 4\ m_k^2c^2\ p_t^{02}}{4\left(s + \vec{p}_t^{\,2}\sin^2\psi\right)}} \qquad (3.15)$$

with $\mathcal{I} = s + (m_k^2 - m_l^2)c^2$. The angle ψ denotes the angle between $\vec{p}_t$ and $\vec{p}_k^{\,'}$. Making use of Equation (3.14) we obtain

$$C_{kl} = \frac{e_k^2 e_l^2 m_k^2 m_l^2 c^2}{4\pi^2 \epsilon_0^2} \int \frac{d^3 p_l}{p_l^0} \int d\Omega_\psi \, \frac{|\vec{p}_k^{\,'}|^2}{p_t^0 |\vec{p}_k^{\,'}| - |\vec{p}_t| p_k^{0\,'} \cos\psi} \times |M_{k\,'l\,'kl}|^2 \left(f_k^{\,'} f_l^{\,'} - f_k f_l \right) , \tag{3.16}$$

where $|\vec{p}_k^{\,'}| = \mathcal{F}_{kl}$ holds. The quantity $d\Omega_\psi$ denotes an element of solid angle between $\vec{p}_t$ and $\vec{p}_k^{\,'}$. As an example the transition matrix elements for elastic binary collisions are given [71],

$$\begin{aligned} |M_{k\,'l\,'kl}|^2 &= \frac{1}{4} \sum_{s_k^{'} s_l^{'} s_k s_l} \left| \bar{u}_k^{\,'} \gamma_\mu u_k \, \frac{1}{t + i\epsilon} \, \bar{u}_l^{\,'} \gamma^\mu u_l \right|^2 \\ &= \frac{(p_l^{\,'} \cdot p_k^{\,'})(p_l \cdot p_k) + (p_l^{\,'} \cdot p_k)(p_l \cdot p_k^{\,'})}{2 m_k^2 m_l^2 c^4 t^2} \\ &\quad - \frac{m_k^2 c^2 (p_l^{\,'} \cdot p_l) + m_l^2 c^2 (p_k^{\,'} \cdot p_k) - 2 m_k^2 m_l^2 c^4}{2 m_k^2 m_l^2 c^4 t^2} , \end{aligned} \tag{3.17}$$

where $t = (p_k - p_k^{\,'})^2$ holds. The pre- and post-collision masses in Eqn. (3.17) are the same. To perform the angle integration implied in Equation (3.16) we introduce a coordinate system whose polar axis is parallel to $\vec{p}_t$. With the help of this vector and the $\vec{e}_z$-direction

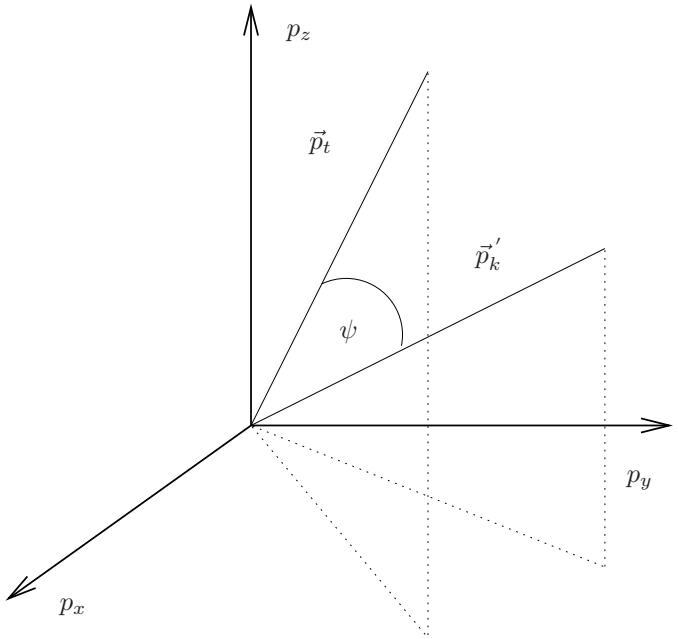

Figure 3.1: Angle integration in the collision operator. The momentum $\vec{p}_k^{\,'}$ is the integration variable. The polar axis of the new coordinate system is parallel to $\vec{p}_t$. The element of solid angle in the new coordinate system is given by $d\Omega_\psi = d\nu \, d\psi \sin\psi$.

we form a triple set of mutually perpendicular vectors, the remaining two of which are $\vec{p}_t \times \vec{e}_z$

and $\vec{p}_t \times (\vec{e}_z \times \vec{p}_t)$ with magnitudes $|\vec{p}_t|$, $|\vec{p}_t| \sin\theta$ and $|\vec{p}_t|^2 \sin\theta$. The quantities $|\vec{p}_t|$, θ and ϕ denote the polar coordinates of $\vec{p}_t$. The integration over $\vec{p}_k^{\,'}$ can now be carried out. In the new frame the element of solid angle is $d\Omega_\psi = d\nu d\psi \sin\psi$ (see Figure 3.1). We find

$$\begin{aligned} \vec{p}_k^{\,'} &= |\vec{p}_k^{\,'}| \cos\psi \begin{pmatrix} \sin\theta\cos\phi \\ \sin\theta\sin\phi \\ \cos\theta \end{pmatrix} + |\vec{p}_k^{\,'}| \sin\psi \sin\nu \begin{pmatrix} \sin\phi \\ -\cos\phi \\ 0 \end{pmatrix} \\ &\quad -|\vec{p}_k^{\,'}| \sin\psi \cos\nu \begin{pmatrix} \cos\theta\cos\phi \\ -\cos\theta\sin\phi \\ \sin\theta \end{pmatrix} \end{aligned} \tag{3.18}$$

and

$$\vec{p}_t = |\vec{p}_t| \begin{pmatrix} \sin\theta\cos\phi \\ \sin\theta\sin\phi \\ \cos\theta \end{pmatrix} . \tag{3.19}$$

Equations (3.15), (3.16), (3.17), (3.18), and (3.19) give the general form of the binary Boltzmann collision operator in an arbitrary frame.

The simplest derivation is obtained with the help of the center of mass frame, where we have $\vec{p}_t = 0$ and $s = p_t^{02}$. Equation (3.14) becomes

$$\frac{1}{p_k^{'0} p_l^{'0}} \, \delta\left(p_k^0 + p_l^0 - p_k^{'0} - p_l^{'0}\right) = \frac{1}{|\vec{p}_k^{\,'}|\sqrt{s}} \, \delta\left(|\vec{p}_k^{\,'}| - \frac{F_{kl}}{\sqrt{s}}\right) , \tag{3.20}$$

where the invariant flux F_{kl} is obtained from Equation (3.15)

$$\begin{aligned} F_{kl} &= \frac{1}{2} \sqrt{s\,(s - 2[m_k^2 + m_l^2]c^2) + [m_k^2 - m_l^2]^2 c^4} \\ &= \sqrt{(p_k \cdot p_l)^2 - m_k^2 m_l^2 c^4} \, . \end{aligned} \tag{3.21}$$

Next we integrate Equation (3.11) over $\vec{p}_l^{\,'}$ and $\vec{p}_k^{\,'}$ making use of Eqn. (3.12). With the help of Equation (3.20) we obtain

$$\frac{c}{p_k^0} \, C_{kl} = \int d^3 p_l \; v_{kl} \int d\Omega_\psi \; \sigma^{kl}(s,\psi) \; \left(f_k^{\,'} f_l^{\,'} - f_k f_l\right) , \tag{3.22}$$

as has been stated in the introduction. The quantity $d\Omega_\psi$ now represents an element of solid angle between $\vec{p}_k$ and $\vec{p}_k^{\,'}$. The quantities $\vec{p}_k^{\,'}$ and ψ are the post collisional momentum in the center of mass frame and the scattering angle between $\vec{p}_k^{\,'}$ and $\vec{p}_k$ in the latter. Explicitly they are given by

$$|\vec{p}_k^{\,'}| = \frac{F_{kl}}{\sqrt{s}} \, , \qquad \cos\psi = 1 + \frac{s \cdot t}{2F_{kl}^2} \, . \tag{3.23}$$

In the PSC we do not integrate the Boltzmann equation directly. Details of the numerical approach to the integration of the Boltzmann collision operator used in the PSC are outlined in section 4.4.

3.3 The collision integral for immobile ions

As an instructive example we calculate the collision integral Eqn. (3.16) for immobile ions ($m_i \gg m_e$) and derive an expression for the electron-ion collision frequency in the non-relativistic limit.

Assuming that the ions are at rest initially and do not change momentum during the electron-ion collision process the relation $|\vec{p}_e^{\,'}| = |\vec{p}_e|$ is obtained with the help of Eqn. (3.14). We find for the collision operator

$$C_{ei} \;=\; \frac{e_e^2 e_i^2 m_e^2}{4\pi^2\epsilon_0^2}\; n_i\; |\vec{p}_e| \int d\Omega_\psi \;\; |M_e|^2 \;\left(f_e^{\,'} - f_e\right) \;, \tag{3.24}$$

where the transition matrix elements for a statically shielded potential are given by Eqn. (3.17). We have

$$|M_e|^2 \;=\; \frac{p_e^{02}}{m_e^2 c^2 \left|\sum_{ij} q_i q_j \epsilon_{ij}\,(0,\vec{q})\right|^2} \;\left[1 - \frac{\vec{p}_e^{\,2}}{p_e^{02}} \sin^2\frac{\psi}{2}\right] \tag{3.25}$$

with

$$\epsilon_{ij}\,(0,\vec{q}) \;=\; \delta_{ij}\left(1 + \frac{\hbar^2}{\lambda_D^2 |\vec{q}|^2}\right) \;, \qquad \vec{q} = \vec{p}_e^{\,'} - \vec{p}_e \;, \tag{3.26}$$

where λ_D denotes the plasma Debye length. We obtain for the invariant cross section

$$\sigma^{ei}(\psi) \;=\; \frac{e_e^2 e_i^2 m_e^2}{4\pi^2\epsilon_0^2}\;|M_e|^2 = \frac{e_e^2 e_i^2}{64\pi^2\epsilon_0^2}\;\frac{p_e^2\left(1-\sin\frac{\psi}{2}\right) + m_e^2 c^2}{\left(p_e^2\,\sin^2\frac{\psi}{2} + \frac{\hbar^2}{4\lambda_D^2}\right)^2} \;. \tag{3.27}$$

Stating the invariant cross section in the non-relativistic limit $\vec{p}_e^{\,2} \ll p_e^{02}$ we find

$$\sigma^{ei}(\psi) \;\approx\; \frac{e_e^2 e_i^2}{64\pi^2\epsilon_0^2 m_e^2}\;\frac{1}{\left(v_e^2\,\sin^2\frac{\psi}{2} + \frac{\hbar^2}{4m_e^2\,\lambda_D^2}\right)^2} \;. \tag{3.28}$$

In case of negligible static shielding ($\epsilon_{ij}(0,\vec{q}) = \delta_{ij}$), we get in the limit of small scattering angles,

$$\sigma^{ei}(\psi) \;\approx\; \frac{e_e^2 e_i^2}{4\pi^2\epsilon_0^2 m_e^2\, v_e^4\,\psi^4} \;. \tag{3.29}$$

With the help of (3.24) we can derive a simple electron-ion collision frequency. We first expand the distribution function $f_e^{\,'}$ in Equation (3.24) up to first order in terms of the electron momentum transfer. We find

$$f_e^{\,'} \approx f_e + \left(\vec{p}_e^{\,'} - \vec{p}_e\right)\cdot\partial_{\vec{p}_e} f_e \;. \tag{3.30}$$

Making use of Eqns. (3.29) and (3.30) and neglecting the relativistic corrections in Eqn. (3.25) we obtain for the collision operator (3.24) the following approximation

$$C_{ei} \;\approx\; -\,\frac{p_e^0}{c}\;\nu_{ei}(\vec{v}_e)\;\vec{p}_e\cdot\frac{\partial f_e}{\partial\vec{p}_e} \;, \tag{3.31}$$

where

$$\nu^{ei}(v_e) \;=\; \frac{e_e^2 e_i^2 n_i}{4\pi\epsilon_0^2 m_e^2 v_e^3}\;\ln\frac{\psi_{max}}{\psi_{min}} \;. \tag{3.32}$$

The collision operator (3.31) leads to friction in the electron fluid. The interested reader is referred to the extensive literature in the field of electron stopping in plasma [72, 73].

Chapter 4

The numerical approach

Modern investigations of intense laser-plasma interaction rely extensively on numerical computation due to the non-linearities and geometries implied in the problems.

In recent years one numerical approach to solve the Maxwell-Vlasov-Boltzmann equations has gained great attention. The method is known as the Monte-Carlo Particle-In-Cell (MCPIC) approach. In this chapter a description of the MCPIC method used in the PSC code is given. The MCPIC method makes use of a mesh to represent the Maxwell fields and of finite elements or quasi-particles to represent the distribution function. A second mesh is required to define an interaction range for colliding particles. In many modern codes as the PSC both meshes are the same because they overlap for a large range of parameters. However, there is no physical reason that requires that both girds are the same. On the contrary, Maxwell fields at high plasma densities may need a mesh that is much finer than the one required for collisions.

4.1 Normalization

For numerical calculations normalized quantities are used. A convenient way to normalize the Vlasov equation and Maxwell equations is obtained with the help of the laser frequency ω, the speed of light c, and the plasma wavelength $\lambda_D = c/\omega$. The following dimensionless parameters are used

$$\tilde{t} \;=\; \omega t\,, \qquad \tilde{\vec{x}} = \frac{\vec{x}}{\lambda_D}\,, \qquad \tilde{\vec{p}^{\,k}} = \frac{\vec{p}^{\,k}}{m^k c}\,. \tag{4.1}$$

To normalize the field amplitudes, charge and current densities the quantities E_0, B_0, ρ_0, and j_0 are introduced

$$\vec{E} \;\to\; \frac{\vec{E}}{E_0}\,, \qquad \vec{B} \to \frac{\vec{B}}{B_0}\,, \qquad \vec{j} \to \frac{\vec{j}}{j_0}\,, \qquad \rho \to \frac{\rho}{\rho_0}\,. \tag{4.2}$$

In the following dimensionless quantities are not indicated explicitly. In dimensionless units Eqns. (3.7) are given by

$$\partial_t \vec{E} \;=\; \vec{\nabla} \times \vec{B} - \vec{j}\,, \tag{4.3}$$

$$\partial_t \vec{B} \;=\; -\vec{\nabla} \times \vec{E}\,, \tag{4.4}$$

$$\partial_t \rho \;=\; -\vec{\nabla} \cdot \vec{j}\,, \tag{4.5}$$

where for consistency

$$B_0 \;=\; \frac{E_0}{c}\,, \qquad j_0 = \epsilon_0 \omega E_0\,, \qquad \rho_0 = \epsilon_0 \omega B_0\,. \tag{4.6}$$

For the normalization of the Vlasov-Boltzmann equation (3.6), the charge and current densities (3.10), the parameters Q, M, T, v_{os}, ω_p, f_0, and σ_0 are introduced where Q denotes an arbitrary charge, M an arbitrary mass, T an arbitrary temperature, v_{os} an oscillation velocity with charge Q and mass M, ω_p the plasma frequency for the density n_0, mass M, and temperature T, f_0 the normalization of the distribution function, and σ_0 the normalization of the cross section σ. It follows

$$\begin{aligned}\left(\partial_t + \vec{v}\cdot\partial_{\vec{x}} + \frac{q^k\,M}{Q\,m^k}\eta\left[\vec{E} + \vec{v}\times\vec{B}\right]\partial_{\vec{p}}\right) f_k \\ = \sum_l \int d^3p^l\, v^{kl} \int d\Omega_k\, \sigma\, \left(f_k^{'} f_l^{'} - f_k f_l\right)\end{aligned} \tag{4.7}$$

and

$$\rho_k \;=\; \frac{q^k\,m^{k3}}{QM^3}\int d^3p\, f_k\,, \qquad \vec{j}_k = \frac{q^k\,m^{k3}}{QM^3}\int d^3p\,\vec{v}\, f_k\,, \tag{4.8}$$

where for consistency

$$\eta = \frac{v_{os}}{c}\,, \qquad v_{os} = \frac{QE_0}{M\omega}\,, \qquad f_0 = \frac{\eta}{\alpha^2}\,\frac{n_0}{M^3c^3}\,, \qquad \sigma_0 = \frac{\alpha^2 M^3}{\eta\, m^{l3}}\,\frac{\omega}{n_0 c} \tag{4.9}$$

hold. The final step consists in normalizing the initial distribution function. For illustration it is assumed that it is given by a Maxwellian. Introducing the temperature t^k it is found

$$\begin{aligned} f_k \;&=\; \frac{\alpha^2}{\eta}\,\frac{M^3}{m^{k3}}\,D_k\,n_k\,\exp\left[-\frac{m^k\,T}{Mt^k\beta^2}\left(\sqrt{1+\vec{p}^2}-1\right)\right]\,, \\ D_k^{-1} \;&=\; \int d^3p\,\exp\left[-\frac{m^k\,T}{M\,t^k\,\beta^2}\left(\sqrt{1+\vec{p}^2}-1\right)\right]\,, \end{aligned} \tag{4.10}$$

where

$$\alpha \;=\; \frac{\omega_p}{\omega}\,, \qquad \beta = \frac{v_t}{c}\,, \qquad \omega_p = \sqrt{\frac{Q^2\,n_0}{\epsilon_0\,M}}\,, \qquad v_t = \sqrt{\frac{k_B T}{M}}\,. \tag{4.11}$$

The quantities Q, M, and T are free parameters. They are used to guarantee the correct normalization in case of zero charge, mass or temperature. A convenient choice for Q is the electron charge, for M the electron mass, and for T a temperature of 1 keV.

4.2 Maxwell's equations

In this section the Finite-Difference-Time-Domain (FDTD) numerical scheme for the integration of Maxwell equations (4.3), (4.4), and (4.5) is described.

4.2.1 The FDTD scheme

The starting point are the Maxwell's equations in 3D in normalized units

$$\begin{aligned} \partial_t E_x &= (\partial_y B_z - \partial_z B_y) - j_x \ , \\ \partial_t E_y &= (\partial_z B_x - \partial_x B_z) - j_y \ , \\ \partial_t E_z &= (\partial_x B_y - \partial_y B_x) - j_z \end{aligned} \tag{4.12}$$

and

$$\begin{aligned} \partial_t B_x &= -\partial_y E_z + \partial_z E_y \ , \\ \partial_t B_y &= -\partial_z E_x + \partial_x E_z \ , \\ \partial_t B_z &= -\partial_x E_y + \partial_y E_x \end{aligned} \tag{4.13}$$

and

$$\partial_t \rho = -\partial_x j_x - \partial_y j_y - \partial_z j_z \ . \tag{4.14}$$

Next the discretization of spatial derivatives is introduced

$$\vec{\nabla}^- F^n_{jkl} = \left(\frac{F^n_{jkl} - F^n_{j-1kl}}{\Delta x}, \frac{F^n_{jkl} - F^n_{jk-1l}}{\Delta y}, \frac{F^n_{jkl} - F^n_{jkl-1}}{\Delta z} \right) \ , \tag{4.15}$$

$$\vec{\nabla}^+ F^n_{jkl} = \left(\frac{F^n_{j+1kl} - F^n_{jkl}}{\Delta x}, \frac{F^n_{jk+1l} - F^n_{jkl}}{\Delta y}, \frac{F^n_{jkl+1} - F^n_{jkl}}{\Delta z} \right) \ , \tag{4.16}$$

where $F^n_{jkl} = F\left(j\Delta x, k\Delta y, l\Delta z, n\Delta t\right)$. The step sizes along the coordinate directions and time are denoted by Δx, Δy, Δz, and Δt. The field F represents each of the field components of $\vec{E}$ and $\vec{B}$ with the properties

$$\vec{\nabla}^- \cdot \vec{\nabla}^- \times \vec{F}^{\,n}_{jkl} = 0 \ , \qquad \vec{\nabla}^+ \cdot \vec{\nabla}^+ \times \vec{F}^{\,n}_{jkl} = 0 \ . \tag{4.17}$$

The discrete Maxwell equations now read

$$\frac{\vec{E}^{n+\frac{1}{2}}_{jkl} - \vec{E}^{n-\frac{1}{2}}_{jkl}}{\Delta t} = \vec{\nabla}^- \times \vec{B}^{\,n}_{jkl} - \vec{j}^{\,n}_{jkl} \ , \tag{4.18}$$

$$\frac{\vec{B}^{n+1}_{jkl} - \vec{B}^{n}_{jkl}}{\Delta t} = -\vec{\nabla}^+ \times \vec{E}^{n+\frac{1}{2}}_{jkl} \ , \tag{4.19}$$

$$\frac{\rho^{n+\frac{3}{2}}_{jkl} - \rho^{n+\frac{1}{2}}_{jkl}}{\Delta t} = -\vec{\nabla}^- \cdot \vec{j}^{\,n+1}_{jkl} \ , \tag{4.20}$$

where

$$\vec{E}^{n+\frac{1}{2}}_{jkl} = \left((E_x)^{n+\frac{1}{2}}_{j+\frac{1}{2}kl}, (E_y)^{n+\frac{1}{2}}_{jk+\frac{1}{2}l}, (E_z)^{n+\frac{1}{2}}_{jkl+\frac{1}{2}} \right) \ , \tag{4.21}$$

$$\vec{B}^{n}_{jkl} = \left((B_x)^{n}_{jk+\frac{1}{2}l+\frac{1}{2}}, (B_y)^{n}_{j+\frac{1}{2}kl+\frac{1}{2}}, (B_z)^{n}_{j+\frac{1}{2}k+\frac{1}{2}l} \right) \ , \tag{4.22}$$

$$\vec{j}^{\,n+1}_{jkl} = \left((j_x)^{n+1}_{j+\frac{1}{2}kl}, (j_y)^{n+1}_{jk+\frac{1}{2}l}, (j_z)^{n+1}_{jkl+\frac{1}{2}} \right) \ . \tag{4.23}$$

In the Vlasov solver the fields at half time steps are needed. Hence, we split Maxwell's equations as follows

$$\vec{E}^{\,n+\frac{1}{2}}_{jkl} - \vec{E}^{\,n}_{jkl} = \frac{\Delta t}{2} \left(\vec{\nabla}^- \times \vec{B}^{\,n}_{jkl} - \vec{j}^{\,n}_{jkl} \right) \ , \tag{4.24}$$

$$\vec{B}_{jkl}^{\,n+\frac{1}{2}} - \vec{B}_{jkl}^{\,n} = -\frac{\Delta t}{2}\,\vec{\nabla}^{+} \times \vec{E}_{jkl}^{\,n+\frac{1}{2}}\ , \tag{4.25}$$

$$\frac{\rho_{jkl}^{\,n+\frac{3}{2}} - \rho_{jkl}^{\,n+\frac{1}{2}}}{\Delta t} = -\,\vec{\nabla}^{-} \cdot \vec{j}_{jkl}^{\,n+1}\ , \tag{4.26}$$

$$\vec{B}_{jkl}^{\,n+1} - \vec{B}_{jkl}^{\,n+\frac{1}{2}} = -\frac{\Delta t}{2}\,\vec{\nabla}^{+} \times \vec{E}_{jkl}^{\,n+\frac{1}{2}}\ , \tag{4.27}$$

$$\vec{E}_{jkl}^{\,n+1} - \vec{E}_{jkl}^{\,n+\frac{1}{2}} = \frac{\Delta t}{2}\left(\vec{\nabla}^{-} \times \vec{B}_{jkl}^{\,n+1} - \vec{j}_{jkl}^{\,n+1}\right)\ . \tag{4.28}$$

In order to complete the scheme the initial and boundary conditions as well as the charge and current densities must be specified. We will describe this in the next sections. The stability and dispersion properties of the numerical scheme given here will not be discussed. It is know as the FDTD scheme in the literature. The interested reader may find some more details in [84].

4.2.2 Periodic boundary conditions

To simulate infinite systems with a finite number of cells periodic boundary conditions are convenient. We assume that the boundaries of the cubic simulation box in x, y, and z are located at $x_1 = i1n\,\Delta x$, $x_2 = i1x\,\Delta x$, $y_1 = i2n\,\Delta y$, $y_2 = i2x\,\Delta y$, $z_1 = i3n\,\Delta z$, and $z_2 = i3x\,\Delta z$. For periodic boundary conditions we find for the electric fields along x

$$\begin{aligned}
&(E_x)_{i1n-\frac{1}{2},k,l} = (E_x)_{i1x+\frac{1}{2},k,l}\ , \qquad (E_x)_{i1x+\frac{3}{2},k,l} = (E_x)_{i1n+\frac{1}{2},k,l}\ , \\
&(E_y)_{i1n-1,k+\frac{1}{2},l} = (E_y)_{i1x,k+\frac{1}{2},l}\ , \qquad (E_y)_{i1x+1,k+\frac{1}{2},l} = (E_y)_{i1n,k+\frac{1}{2},l}\ , \\
&(E_z)_{i1n-1,k,l+\frac{1}{2}} = (E_z)_{i1x,k,l+\frac{1}{2}}\ , \qquad (E_z)_{i1x+1,k,l+\frac{1}{2}} = (E_z)_{i1n,k,l+\frac{1}{2}}\ .
\end{aligned} \tag{4.29}$$

Analogously, for periodic boundary conditions along y we find

$$\begin{aligned}
&(E_x)_{j+\frac{1}{2},i2n-1,l} = (E_x)_{j+\frac{1}{2},i2x,l}\ , \qquad (E_x)_{j+\frac{1}{2},i2x+1,l} = (E_x)_{j+\frac{1}{2},i2n,l}\ , \\
&(E_y)_{j,i2n-\frac{1}{2},l} = (E_y)_{j,i2x+\frac{1}{2},l}\ , \qquad (E_y)_{j,i2x+\frac{3}{2},l} = (E_y)_{j,i2n+\frac{1}{2},l}\ , \\
&(E_z)_{j,i2n-1,l+\frac{1}{2}} = (E_z)_{j,i2x,l+\frac{1}{2}}\ , \qquad (E_z)_{j,i2x+1,l+\frac{1}{2}} = (E_z)_{j,i2n,l+\frac{1}{2}}\ ,
\end{aligned} \tag{4.30}$$

and for periodic boundary conditions along z

$$\begin{aligned}
&(E_x)_{j+\frac{1}{2},k,i3n-1} = (E_x)_{j+\frac{1}{2},k,i3x}\ , \qquad (E_x)_{j+\frac{1}{2},k,i3x+1} = (E_x)_{j+\frac{1}{2},k,i3n}\ , \\
&(E_y)_{j,k+\frac{1}{2},i3n-1} = (E_y)_{j,k+\frac{1}{2},i3x}\ , \qquad (E_y)_{j,k+\frac{1}{2},i3x+1} = (E_y)_{j,k+\frac{1}{2},i3n}\ , \\
&(E_z)_{j,k,i3n-\frac{1}{2}} = (E_z)_{j,k,i3x+\frac{1}{2}}\ , \qquad (E_z)_{i1x+1,k,i3x+\frac{3}{2}} = (E_z)_{j,k,i3n+\frac{1}{2}}\ .
\end{aligned} \tag{4.31}$$

Similar relations hold for the magnetic field.

4.2.3 Radiating boundary conditions

Maxwell's equations (4.12) and (4.13) can be recast in the following form

$$\partial_t\,(E_x \pm B_y) \pm \partial_z\,(E_x \pm B_y) = \pm\partial_x E_z + \partial_y B_z - j_x \tag{4.32}$$

$$\partial_t\,(E_y \mp B_x) \pm \partial_z\,(E_y \mp B_x) = \pm\partial_y E_z - \partial_x B_z - j_y \tag{4.33}$$

$$\partial_t\,(E_x \mp B_z) \pm \partial_y\,(E_x \mp B_z) = \pm\partial_x E_y - \partial_z B_y - j_x \tag{4.34}$$

$$\partial_t\,(E_z \pm B_x) \pm \partial_y\,(E_z \pm B_x) = \pm\partial_z E_y + \partial_x B_y - j_z \tag{4.35}$$

$$\partial_t\,(E_y \pm B_z) \pm \partial_x\,(E_y \pm B_z) = \pm\partial_y E_x + \partial_z B_x - j_y \tag{4.36}$$

$$\partial_t\,(E_z \mp B_y) \pm \partial_x\,(E_z \mp B_y) = \pm\partial_z E_x - \partial_y B_x - j_z \tag{4.37}$$

It is possible to use Eqns. (4.32) to (4.37) for a definition of so-called radiating boundaries. Equations (4.32) and (4.33) can be interpreted as forward and backward propagating waves along z in vacuum if the components E_z and B_z disappear. With the help of Eqns. (4.18) we find for the S- and P-polarized waves propagating in the positive (+) and negative (−) directions along z

$$\begin{aligned} 2S^n_{j+\frac{1}{2},k,l} &= (E_x)^n_{j+\frac{1}{2},k,l} \pm (B_y)^n_{j+\frac{1}{2},k,l} \qquad (4.38)\\ &= (E_x)^{n-\frac{1}{2}}_{j+\frac{1}{2},k,l} + \frac{\Delta t}{2\Delta y}\left((B_z)^n_{j+\frac{1}{2},k+\frac{1}{2},l} - (B_z)^n_{j+\frac{1}{2},k-\frac{1}{2},l}\right)\\ &\quad -\frac{\Delta t}{2\Delta z}\left((B_y)^n_{j+\frac{1}{2},k,l+\frac{1}{2}} - (B_y)^n_{j+\frac{1}{2},k,l-\frac{1}{2}}\right)\\ &\quad \pm\frac{1}{2}\left((B_y)^n_{j+\frac{1}{2},k,l+\frac{1}{2}} + (B_y)^n_{j+\frac{1}{2},k,l-\frac{1}{2}}\right) - \frac{\Delta t}{2}(j_x)^n_{j+\frac{1}{2},k,l}\ ,\\ 2P^n_{j,k+\frac{1}{2},l} &= (E_y)^n_{j,k+\frac{1}{2},l} \mp (B_x)^n_{j,k+\frac{1}{2},l} \qquad (4.39)\\ &= (E_y)^{n-\frac{1}{2}}_{j,k+\frac{1}{2},l} + \frac{\Delta t}{2\Delta z}\left((B_x)^n_{j,k+\frac{1}{2},l+\frac{1}{2}} - (B_x)^n_{j,k+\frac{1}{2},l-\frac{1}{2}}\right)\\ &\quad -\frac{\Delta t}{2\Delta x}\left((B_z)^n_{j+\frac{1}{2},k+\frac{1}{2},l} - (B_z)^n_{j-\frac{1}{2},k+\frac{1}{2},l}\right)\\ &\quad \mp\frac{1}{2}\left((B_x)^n_{j,k+\frac{1}{2},l+\frac{1}{2}} + (B_x)^n_{j,k+\frac{1}{2},l-\frac{1}{2}}\right) - \frac{\Delta t}{2}(j_y)^n_{j,k+\frac{1}{2},l}\ . \end{aligned}$$

The required field components at the left boundary are those that contain the index $l-1/2$ with $l = i3n-1$. We find

$$\begin{aligned} (B_y)^n_{j+\frac{1}{2},k,l-\frac{1}{2}} &= \frac{1}{1+\frac{\Delta t}{\Delta z}}\Big[4S^n_{j+\frac{1}{2},k,l} - 2(E_x)^{n-\frac{1}{2}}_{j+\frac{1}{2},k,l} \qquad (4.40)\\ &\quad -\frac{\Delta t}{\Delta y}\left((B_z)^n_{j+\frac{1}{2},k+\frac{1}{2},l} - (B_z)^n_{j+\frac{1}{2},k-\frac{1}{2},l}\right)\\ &\quad -\left(1-\frac{\Delta t}{\Delta z}\right)(B_y)^n_{j+\frac{1}{2},k,l+\frac{1}{2}}\\ &\quad +\Delta t\,(j_x)^n_{j+\frac{1}{2},k,l}\Big]\\ (B_x)^n_{j,k+\frac{1}{2},l-\frac{1}{2}} &= \frac{1}{1+\frac{\Delta t}{\Delta z}}\Big[-4P^n_{j,k+\frac{1}{2},l} + 2(E_y)^{n-\frac{1}{2}}_{j,k+\frac{1}{2},l} \qquad (4.41)\\ &\quad -\frac{\Delta t}{\Delta x}\left((B_z)^n_{j+\frac{1}{2},k+\frac{1}{2},l} - (B_z)^n_{j-\frac{1}{2},k+\frac{1}{2},l}\right)\\ &\quad -\left(1-\frac{\Delta t}{\Delta z}\right)(B_x)^n_{j,k+\frac{1}{2},l+\frac{1}{2}}\\ &\quad -\Delta t\,(j_y)^n_{j,k+\frac{1}{2},l}\Big]\ . \end{aligned}$$

At the right boundary the required field components are those that contain the index $l+1/2$ with $l = i3x+1$. We obtain

$$\begin{aligned} (B_y)^n_{j+\frac{1}{2},k,l+\frac{1}{2}} &= \frac{1}{1+\frac{\Delta t}{\Delta z}}\Big[-4S^n_{j+\frac{1}{2},k,l} + 2(E_x)^{n-\frac{1}{2}}_{j+\frac{1}{2},k,l} \qquad (4.42)\\ &\quad +\frac{\Delta t}{\Delta y}\left((B_z)^n_{j+\frac{1}{2},k+\frac{1}{2},l} - (B_z)^n_{j+\frac{1}{2},k-\frac{1}{2},l}\right)\\ &\quad -\left(1-\frac{\Delta t}{\Delta z}\right)(B_y)^n_{j+\frac{1}{2},k,l-\frac{1}{2}} \end{aligned}$$

$$
\begin{aligned}
& -\Delta t\,(j_x)^n_{j+\frac{1}{2},k,l}\Big] \\
(B_x)^n_{j,k+\frac{1}{2},l+\frac{1}{2}} &= \frac{1}{1+\frac{\Delta t}{\Delta z}}\Big[4P^n_{j,k+\frac{1}{2},l} - 2(E_y)^{n-\frac{1}{2}}_{j,k+\frac{1}{2},l} \\
& +\frac{\Delta t}{\Delta x}\left((B_z)^n_{j+\frac{1}{2},k+\frac{1}{2},l} - (B_z)^n_{j-\frac{1}{2},k+\frac{1}{2},l}\right) \\
& -\left(1-\frac{\Delta t}{\Delta z}\right)(B_x)^n_{j,k+\frac{1}{2},l-\frac{1}{2}} \\
& +\Delta t\,(j_y)^n_{j,k+\frac{1}{2},l}\Big]\ .
\end{aligned}
\tag{4.43}
$$

The functions S and P represent arbitrary functions for the incident laser pulse, where S stands for the electric field component of the laser along x and P for the one along y. Equations (4.34) and (4.35) can be used to define radiating boundaries along y. We obtain

$$
\begin{aligned}
2S^n_{j+\frac{1}{2},k,l} &= (E_x)^n_{j+\frac{1}{2},k,l} \mp (B_z)^n_{j+\frac{1}{2},k,l} \\
&= (E_x)^{n-\frac{1}{2}}_{j+\frac{1}{2},k,l} + \frac{\Delta t}{2\Delta y}\left((B_z)^n_{j+\frac{1}{2},k+\frac{1}{2},l} - (B_z)^n_{j+\frac{1}{2},k-\frac{1}{2},l}\right) \\
& -\frac{\Delta t}{2\Delta z}\left((B_y)^n_{j+\frac{1}{2},k,l+\frac{1}{2}} - (B_y)^n_{j+\frac{1}{2},k,l-\frac{1}{2}}\right) \\
& \mp\frac{1}{2}\left((B_z)^n_{j+\frac{1}{2},k+\frac{1}{2},l} + (B_z)^n_{j+\frac{1}{2},k-\frac{1}{2},l}\right) - \frac{\Delta t}{2}(j_x)^n_{j+\frac{1}{2},k,l}\ ,
\end{aligned}
\tag{4.44}
$$

$$
\begin{aligned}
2P^n_{j,k,l+\frac{1}{2}} &= (E_z)^n_{j,k,l+\frac{1}{2}} \pm (B_x)^n_{j,k,l+\frac{1}{2}} \\
&= (E_z)^{n-\frac{1}{2}}_{j,k,l+\frac{1}{2}} + \frac{\Delta t}{2\Delta x}\left((B_y)^n_{j+\frac{1}{2},k,l+\frac{1}{2}} - (B_y)^n_{j-\frac{1}{2},k,l+\frac{1}{2}}\right) \\
& -\frac{\Delta t}{2\Delta y}\left((B_x)^n_{j,k+\frac{1}{2},l+\frac{1}{2}} - (B_x)^n_{j,k-\frac{1}{2},l+\frac{1}{2}}\right) \\
& \pm\frac{1}{2}\left((B_x)^n_{j,k+\frac{1}{2},l+\frac{1}{2}} + (B_x)^n_{j,k-\frac{1}{2},l+\frac{1}{2}}\right) - \frac{\Delta t}{2}(j_z)^n_{j,k,l+\frac{1}{2}}\ .
\end{aligned}
\tag{4.45}
$$

The required field components at the left boundary are those that contain the index $k-1/2$ with $k = i2n-1$

$$
\begin{aligned}
(B_z)^n_{j+\frac{1}{2},k-\frac{1}{2},l} &= \frac{1}{1+\frac{\Delta t}{\Delta y}}\Big[-4S^n_{j+\frac{1}{2},k,l} + 2(E_x)^{n-\frac{1}{2}}_{j+\frac{1}{2},k,l} \\
& -\frac{\Delta t}{\Delta z}\left((B_y)^n_{j+\frac{1}{2},k,l+\frac{1}{2}} - (B_y)^n_{j+\frac{1}{2},k,l-\frac{1}{2}}\right) \\
& -\left(1-\frac{\Delta t}{\Delta y}\right)(B_z)^n_{j+\frac{1}{2},k+\frac{1}{2},l} \\
& +\Delta t\,(j_x)^n_{j+\frac{1}{2},k,l}\Big]
\end{aligned}
\tag{4.46}
$$

$$
\begin{aligned}
(B_x)^n_{j,k-\frac{1}{2},l+\frac{1}{2}} &= \frac{1}{1+\frac{\Delta t}{\Delta y}}\Big[4P^n_{j,k,l+\frac{1}{2}} - 2(E_z)^{n-\frac{1}{2}}_{j,k,l+\frac{1}{2}} \\
& -\frac{\Delta t}{\Delta x}\left((B_y)^n_{j+\frac{1}{2},k,l+\frac{1}{2}} - (B_y)^n_{j-\frac{1}{2},k,l+\frac{1}{2}}\right) \\
& -\left(1-\frac{\Delta t}{\Delta y}\right)(B_x)^n_{j,k+\frac{1}{2},l+\frac{1}{2}} \\
& +\Delta t\,(j_z)^n_{j,k,l+\frac{1}{2}}\Big]\ .
\end{aligned}
\tag{4.47}
$$

At the right boundary we have to look for the index $k+1/2$ with $k=i2x+1$. We obtain

$$\begin{aligned}
(B_z)^n_{j+\frac{1}{2},k+\frac{1}{2},l} &= \frac{1}{1+\frac{\Delta t}{\Delta y}}\Big[4S^n_{j+\frac{1}{2},k,l}-2(E_x)^{n-\frac{1}{2}}_{j+\frac{1}{2},k,l} \qquad (4.48)\\
&\quad +\frac{\Delta t}{\Delta z}\left((B_y)^n_{j+\frac{1}{2},k,l+\frac{1}{2}}-(B_y)^n_{j+\frac{1}{2},k,l-\frac{1}{2}}\right)\\
&\quad -\left(1-\frac{\Delta t}{\Delta y}\right)(B_z)^n_{j+\frac{1}{2},k-\frac{1}{2},l}\\
&\quad -\Delta t\,(j_x)^n_{j+\frac{1}{2},k,l}\Big]\\
(B_x)^n_{j,k+\frac{1}{2},l+\frac{1}{2}} &= \frac{1}{1+\frac{\Delta t}{\Delta y}}\Big[-4P^n_{j,k,l+\frac{1}{2}}+2(E_z)^{n-\frac{1}{2}}_{j,k,l+\frac{1}{2}} \qquad (4.49)\\
&\quad +\frac{\Delta t}{\Delta x}\left((B_y)^n_{j+\frac{1}{2},k,l+\frac{1}{2}}-(B_y)^n_{j-\frac{1}{2},k,l+\frac{1}{2}}\right)\\
&\quad -\left(1-\frac{\Delta t}{\Delta y}\right)(B_x)^n_{j,k-\frac{1}{2},l+\frac{1}{2}}\\
&\quad -\Delta t\,(j_z)^n_{j,k,l+\frac{1}{2}}\Big]\ .
\end{aligned}$$

Equations (4.36) and (4.37) can be used to define radiating boundaries along x. Similar considerations apply

$$\begin{aligned}
2S^n_{j,k+\frac{1}{2},l} &= (E_y)^n_{j,k+\frac{1}{2},l}\pm(B_z)^n_{j,k+\frac{1}{2},l} \qquad (4.50)\\
&= (E_y)^{n-\frac{1}{2}}_{j,k+\frac{1}{2},l}+\frac{\Delta t}{2\Delta z}\left((B_x)^n_{j,k+\frac{1}{2},l+\frac{1}{2}}-(B_x)^n_{j,k+\frac{1}{2},l-\frac{1}{2}}\right)\\
&\quad -\frac{\Delta t}{2\Delta x}\left((B_z)^n_{j+\frac{1}{2},k+\frac{1}{2},l}-(B_z)^n_{j-\frac{1}{2},k+\frac{1}{2},l}\right)\\
&\quad \pm\frac{1}{2}\left((B_z)^n_{j+\frac{1}{2},k+\frac{1}{2},l}+(B_z)^n_{j-\frac{1}{2},k+\frac{1}{2},l}\right)-\frac{\Delta t}{2}(j_y)^n_{j,k+\frac{1}{2},l}\ ,\\
2P^n_{j,k,l+\frac{1}{2}} &= (E_z)^n_{j,k,l+\frac{1}{2}}\mp(B_y)^n_{j,k,l+\frac{1}{2}} \qquad (4.51)\\
&= (E_z)^{n-\frac{1}{2}}_{j,k,l+\frac{1}{2}}+\frac{\Delta t}{2\Delta x}\left((B_y)^n_{j+\frac{1}{2},k,l+\frac{1}{2}}-(B_y)^n_{j-\frac{1}{2},k,l+\frac{1}{2}}\right)\\
&\quad -\frac{\Delta t}{2\Delta y}\left((B_x)^n_{j,k+\frac{1}{2},l+\frac{1}{2}}-(B_x)^n_{j,k-\frac{1}{2},l+\frac{1}{2}}\right)\\
&\quad \mp\frac{1}{2}\left((B_y)^n_{j+\frac{1}{2},k,l+\frac{1}{2}}+(B_y)^n_{j-\frac{1}{2},k,l+\frac{1}{2}}\right)-\frac{\Delta t}{2}(j_z)^n_{j,k,l+\frac{1}{2}}\ .
\end{aligned}$$

The required field components at the left boundary are those that contain the index $j-1/2$ with $j=i1n-1$

$$\begin{aligned}
(B_z)^n_{j-\frac{1}{2},k+\frac{1}{2},l} &= \frac{1}{1+\frac{\Delta t}{\Delta x}}\Big[4S^n_{j,k+\frac{1}{2},l}-2(E_y)^{n-\frac{1}{2}}_{j,k+\frac{1}{2},l} \qquad (4.52)\\
&\quad -\frac{\Delta t}{\Delta z}\left((B_x)^n_{j,k+\frac{1}{2},l+\frac{1}{2}}-(B_x)^n_{j,k+\frac{1}{2},l-\frac{1}{2}}\right)\\
&\quad -\left(1-\frac{\Delta t}{\Delta x}\right)(B_z)^n_{j+\frac{1}{2},k+\frac{1}{2},l}\\
&\quad -\Delta t\,(j_y)^n_{j,k+\frac{1}{2},l}\Big]\\
(B_y)^n_{j-\frac{1}{2},k,l+\frac{1}{2}} &= \frac{1}{1+\frac{\Delta t}{\Delta x}}\Big[-4P^n_{j,l,k+\frac{1}{2}}+2(E_z)^{n-\frac{1}{2}}_{j,k,l+\frac{1}{2}} \qquad (4.53)
\end{aligned}$$

$$
\begin{aligned}
&+\frac{\Delta t}{\Delta y}\left((B_x)^n_{j,k+\frac{1}{2},l+\frac{1}{2}}-(B_x)^n_{j,k-\frac{1}{2},l+\frac{1}{2}}\right)\\
&-\left(1-\frac{\Delta t}{\Delta x}\right)(B_y)^n_{j+\frac{1}{2},k,l+\frac{1}{2}}\\
&+\Delta t\,(j_z)^n_{j,k,l+\frac{1}{2}}\Big]\ .
\end{aligned}
$$

At the right boundary we have to look for index $j+1/2$ with $j=i1x+1$ yielding

$$
\begin{aligned}
(B_z)^n_{j+\frac{1}{2},k+\frac{1}{2},l} &= \frac{1}{1+\frac{\Delta t}{\Delta x}}\Big[-4S^n_{j,k+\frac{1}{2},l}+2(E_y)^{n-\frac{1}{2}}_{j,k+\frac{1}{2},l} \qquad (4.54)\\
&-\frac{\Delta t}{\Delta z}\left((B_x)^n_{j,k+\frac{1}{2},l+\frac{1}{2}}-(B_x)^n_{j,k+\frac{1}{2},l-\frac{1}{2}}\right)\\
&-\left(1-\frac{\Delta t}{\Delta x}\right)(B_z)^n_{j-\frac{1}{2},k+\frac{1}{2},l}\\
&+\Delta t\,(j_y)^n_{j,k+\frac{1}{2},l}\Big]\\
(B_y)^n_{j+\frac{1}{2},k,l+\frac{1}{2}} &= \frac{1}{1+\frac{\Delta t}{\Delta x}}\Big[4P^n_{j,l,k+\frac{1}{2}}-2(E_z)^{n-\frac{1}{2}}_{j,k,l+\frac{1}{2}} \qquad (4.55)\\
&+\frac{\Delta t}{\Delta y}\left((B_x)^n_{j,k+\frac{1}{2},l+\frac{1}{2}}-(B_x)^n_{j,k-\frac{1}{2},l+\frac{1}{2}}\right)\\
&-\left(1-\frac{\Delta t}{\Delta x}\right)(B_y)^n_{j-\frac{1}{2},k,l+\frac{1}{2}}\\
&-\Delta t\,(j_z)^n_{j,k,l+\frac{1}{2}}\Big]\ .
\end{aligned}
$$

The modules **PIC_msa.f** and **PIC_msb.f** solve Maxwell equations, where **PIC_msa.f** promotes the field solution by half a time step. The module **PIC_msb.f** integrates the solution by another half time step to complete a full time step. This way the Maxwell fields are available at integer time steps. The module **PIC_msa.f** defines the radiating boundary conditions. Both modules call **PIC_pex.f**, **PIC_pey.f**, and **PIC_pez.f**, which are communication routines. As is evident from the discussions in sections 4.2.2 periodic boundary conditions require access to distributed data. Hence, they are naturally defined in the communication modules **PIC_pex.f**, **PIC_pey.f**, and **PIC_pez.f**. There are flags that are set in the initialization routine **INIT_param.f** to select the desired boundary conditions. Details are explained in section 5.1.

4.3 The Vlasov equation

The Maxwell equations as given in section 4.2 require the knowledge of current and charge densities. In the PSC they are obtained from the integration of the Vlasov-Boltzmann equation. To explain details we now look at the Vlasov equation.

4.3.1 The distribution function

The Vlasov equation (4.7) is best integrated along the particle trajectories. The starting point is a finite element approximation to the distribution function f_k. We have

$$
f_k(\vec{x},\vec{p},t) = \frac{n_0}{N_c}\sum_{i=1}^{N_k}\phi(\vec{x},\vec{x}_i^{\,k}(t))\,\frac{\xi(\vec{p},\vec{p}_i^{\,k}(t))}{\Pi_{j=1}^3\Delta p_j}\ , \qquad (4.56)
$$

where n_0 is the background plasma density, N_c is an arbitrary number that determines the density of a quasi-particle given by n_0/N_c, and N_k is the total number of quasi-particles of population k. The form factors ϕ and ξ are piecewise linear functions given by

$$\phi(\vec{x},\vec{x}_i^{\,k}) = \Pi_{j=1}^3 S_j(x_j, x_{ij}^k(t)) \,, \tag{4.57}$$

$$\xi(\vec{p},\vec{p}_i^{\,k}) = \Pi_{j=1}^3 S_j(p_j, p_{ij}^k(t)) \,, \tag{4.58}$$

where

$$S_j(x_j, x_{ij}^k) = \begin{cases} 1 - \left| \frac{x_j - x_{ij}^k}{\Delta x_j} \right| & , \; x_{ij}^k - \Delta x_j \le x_j \le x_{ij}^k + \Delta x_j \\ 0 & , \text{ else} \end{cases} \,. \tag{4.59}$$

and

$$S_j(p_j, p_{ij}^k) = \begin{cases} 1 - \left| \frac{p_j - p_{ij}^k}{\Delta p_j} \right| & , \; p_{ij}^k - \Delta p_j \le p_j \le p_{ij}^k + \Delta p_j \\ 0 & , \text{ else} \end{cases} \,. \tag{4.60}$$

The Δx_j and Δp_j define the size of the cells in phase space. As is evident the position and momentum of the i-th particle of sort k are denoted by $\vec{x}_i^{\,k}$ and $\vec{p}_i^{\,k}$. For the weight of the form factors given in Eqns. (4.57) and (4.58) one obtains

$$\int_V d^3x \, \phi(\vec{x},\vec{x}_i^{\,k}) = \Pi_{j=1}^3 \Delta x_j \,, \qquad \int d^3p \, \xi(\vec{p},\vec{p}_i^{\,k}) = \Pi_{j=1}^3 \Delta p_j \,. \tag{4.61}$$

The Particle-In-Cell (PIC) method uses finite size form factors in configuration space and δ-functions in momentum space to represent the distribution functions. Hence, we seek an approximation for f_k in the limit $\Delta p_j \to 0$. We obtain for the normalized distribution function (4.10)

$$f_k(\vec{x},\vec{p},t) = \frac{\alpha^2}{\eta} \frac{M^3}{m_k^3} \frac{1}{N_c} \sum_{i=1}^{N_k} \phi(\vec{x} - \vec{x}_i^{\,k}(t)) \, \delta^3(\vec{p} - \vec{p}_i^{\,k}(t)) \,, \tag{4.62}$$

where $\delta^3(\vec{p} - \vec{p}_i^{\,k})$ is the three-dimensional Delta function. We need to distribute the quasi-particles in configuration space in a way that the initial distribution function Eqn. (4.10) is approximated with good accuracy. There are no clear criteria of how best to do this. We choose to locate the quasi-particles at start time either on the mesh points of the Maxwell grid or at equidistant locations between the mesh points. To obtain the correct plasma density we use the initial normalized density $n_k(\vec{x}_i)$, for which $0 \le n_k(\vec{x}_i) \le 1$ holds. Each quasi-particle contributes the constant weight $1/N_c$ to $n_k(\vec{x}_i)$. About $N_c \, n_k(\vec{x}_i)$ quasi-particles are required to approximate $n_k(\vec{x}_i)$ at $\vec{x}_i$.

In addition to position information also a value for momentum has to be assigned to each quasi-element. Hence, the final step consists of finding an approximation for the particle distribution in momentum space as given by Eqn. (4.10). To generate particles according to a Maxwellian momentum distribution we select three uniformly distributed random numbers $0 \le P_i^k < 1$, $0 \le Q_i^k < 1$, and $0 \le R_i^k < 1$ for each quasi-particle i of sort k. With the help of P_i^k, Q_i^k, and R_i^k the quasi-particle momentum vector $\vec{p}_i^{\,k}$ can be written as

$$p_{xi}^k = p_i^k \, \sin\theta_i^k \, \cos\phi_i^k \,, \tag{4.63}$$

$$p_{yi}^k = p_i^k \, \sin\theta_i^k \, \sin\phi_i^k \,, \tag{4.64}$$

$$p_{zi}^k = p_i^k \, \cos\theta_i^k \,, \tag{4.65}$$

where the spherical coordinates ϕ_i^k, θ_i^k, and p_i^k are given by

$$\phi_i^k = 2\pi\, P_i^k \;, \tag{4.66}$$

$$\theta_i^k = \arccos(1 - 2Q_i^k) \;, \tag{4.67}$$

and

$$\frac{\int_0^{p_i^k} dr\, r^2\, \exp\left[-A\,\left(\sqrt{1+r^2}-1\right)\right]}{\int_0^{\infty} dr\, r^2\, \exp\left[-A\,\left(\sqrt{1+r^2}-1\right)\right]} = R_i^k \;, \qquad A = \frac{m_k\, T}{M\, t_k\, \beta^2} \;. \tag{4.68}$$

Equation (4.68) cannot be solved analytically for the momentum p_i^k. However, it can be approximated for large p_i^k. For the generation of non-relativistic Gaussian deviates the Box-Muller method can be applied. With the help of two uniformly distributed random numbers $0 \le P_i^k < 1$ and $0 \le Q_i^k < 1$ two new random numbers with Gaussian deviate can be generated. We find for the new random numbers p_{xi}^{k1} and p_{xi}^{k2} with Gaussian distribution representing the momenta p_{xi}^k

$$\left(\begin{array}{c} p_{xi}^{k1} \\ p_{xi}^{k2} \end{array}\right) = \sqrt{-\frac{1}{A}\,\ln\left(1-P_i^k\right)} \left(\begin{array}{c} \cos 2\pi Q_i^k \\ \sin 2\pi Q_i^k \end{array}\right) \;. \tag{4.69}$$

The same applies for the remaining momentum directions. The finite element representation of the distribution function Eqn. (4.10) is now complete.

4.3.2 Equations of motion

Next we derive the equations of motion for the quasi-elements. To derive them we make use of the non-relativistic Vlasov equation in physical units for simplicity. We multiply the Vlasov equation by $\vec{v}$ and integrate over the velocity space. We obtain

$$\begin{aligned} \partial_t \int d^3v\, \vec{v}\, f_k + \frac{\partial}{\partial x_l} \int d^3v\, v_l\, \vec{v}\, f_k \\ - \int d^3v\, \frac{\partial}{\partial v_l} \left(\frac{q}{m}\,[\vec{E} + \vec{v}\times\vec{B}]_l\, \vec{v}\right)\, f_k = 0 \;, \end{aligned} \tag{4.70}$$

where the distribution function f_k is given by Eqn. (4.62). Inserting f_k into Eqn. (4.70) while neglecting sort labels we find

$$\begin{aligned} \sum_{i=1}^{N_k} \left(\dot{\vec{x}}_i \cdot \frac{\partial\phi(\vec{x},\vec{x}_i)}{\partial\vec{x}_i} + \vec{v}_i \cdot \frac{\partial\phi(\vec{x},\vec{x}_i)}{\partial\vec{x}}\right)\, \vec{v}_i \\ + \sum_{i=1}^{N_k} \left(\dot{\vec{v}}_i - \frac{q}{m}\,[\vec{E} + \vec{v}_i\times\vec{B}]\right)\, \phi(\vec{x},\vec{x}_i) = 0 \;. \end{aligned} \tag{4.71}$$

Integration over the volume V of a single cell and taking into account that ϕ is symmetric in its arguments yield the desired equations of motion for the quasi-particles. They are

$$\frac{d\vec{x}_i}{dt} = \vec{v}_i \;, \tag{4.72}$$

$$\frac{d\vec{v}_i}{dt} = \frac{1}{\Pi_{l=1}^3 \Delta x_l} \int_V d^3x\, \phi(\vec{x}-\vec{x}_i)\, \vec{F}(\vec{x},t) \;, \tag{4.73}$$

$$\vec{F}(\vec{x},t) = \frac{q}{m}\,[\vec{E}(\vec{x},t) + \vec{v}_i \times \vec{B}(\vec{x},t)] \;. \tag{4.74}$$

Hence, an approximate solution for the Vlasov part of Eqn. (4.7) is obtained by propagating quasi-particles according to Newton's equations (4.72) and (4.73) with a Lorentz force. It is instructive to evaluate Eqn. (4.73) for the form factors of the quasi-particles given by Eqn. (4.59). For this it is necessary to state the force distribution around the mesh points. For simplicity and without lack of generality we restrict our considerations to 1D and only to one force component. We assume that the force distribution around the mesh point x_j is

$$F(x,t_n) = \left\{ \begin{array}{cc} F_j^n & x_j - \frac{\Delta x}{2} \le x \le x_j + \frac{\Delta x}{2} \\ 0 & else \end{array} \right. . \tag{4.75}$$

In the following we assume that $x_j - \Delta x/2 \le x_i \le x_j + \Delta x/2$ holds. This means that x_j is the grid point closest to x_i. Figure 4.1 illustrates the details. Under this provision the

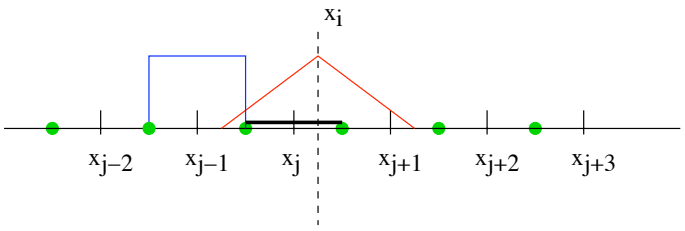

Figure 4.1: The figure shows the overlap between the distributed force and the form factor of a quasi-particle with a triangular shape. The force distribution is indicated by the rectangle and the quasi-particle by the triangle. The x_j's denote the nodes at which the electric and magnetic fields are defined. The position of the quasi-particle is x_i. The electric and magnetic fields reside on staggered grids in case the FDTD scheme is used. The bold line indicates the cell on the field grid the particle is in. The thick dots define the grid that is used to localize the particles.

form factor of the quasi-particle at x_i overlaps with the forces distributed around the nodes x_{j-1}, x_j, and x_{j+1}. Hence, there is a contribution to the integral (4.73) for each of the these nodes. We obtain for Eqn. (4.73)

$$\begin{aligned} \left.\frac{dv_i}{dt}\right|_{t_n} &= \frac{1}{\Delta x}\left[\int_{x_i-\Delta x}^{x_{j-1}+\frac{\Delta x}{2}} dx\, F_{j-1}^n \left(1-\frac{x_i-x}{\Delta x}\right)\right. \\ &+ \int_{x_j-\frac{\Delta x}{2}}^{x_i} dx\, F_j^n \left(1-\frac{x_i-x}{\Delta x}\right) + \int_{x_i}^{x_j+\frac{\Delta x}{2}} dx\, F_j^n \left(1-\frac{x-x_i}{\Delta x}\right) \\ &\left. + \int_{x_{j+1}-\frac{\Delta x}{2}}^{x_i+\Delta x} dx\, F_{j+1}^n \left(1-\frac{x-x_i}{\Delta x}\right)\right] . \end{aligned} \tag{4.76}$$

Performing the integrations we find

$$\begin{aligned} \left.\frac{dv_i}{dt}\right|_{t_n} &= \frac{1}{2}\, F_{j-1}^n \left(\frac{1}{2}+\frac{x_j-x_i}{\Delta x}\right)^2 \\ &+ F_j^n \left(\frac{3}{4}-\frac{(x_j-x_i)^2}{\Delta x^2}\right) \\ &+ \frac{1}{2}\, F_{j+1}^n \left(\frac{1}{2}-\frac{x_j-x_i}{\Delta x}\right)^2 . \end{aligned} \tag{4.77}$$

Equation (4.77) show that a particular interpolation scheme for the force equation has to be applied for a given choice of the form factor of quasi-particles. We now return to dimensionless variables and integrate the equations of motion for the quasi-particles. We find, neglecting particle labels,

$$\begin{aligned}
\frac{dp_x}{dt} &= \frac{q_k\,M}{Q\,m_k}\eta\ \left(E_x + v_y B_z - v_z B_y\right)\ , \\
\frac{dp_y}{dt} &= \frac{q_k\,M}{Q\,m_k}\eta\ \left(E_y + v_z B_x - v_x B_z\right)\ , \\
\frac{dp_z}{dt} &= \frac{q_k\,M}{Q\,m_k}\eta\ \left(E_z + v_x B_y - v_y B_x\right)\ .
\end{aligned} \tag{4.78}$$

The integration of equations (4.72) up to second order accuracy is obtained by first integrating (4.72) for half a time step up to first oder accuracy

$$\begin{aligned}
x\left(t+\frac{\Delta t}{2}\right) &= x(t) + \frac{\Delta t}{2}\,v_x(t)\ , \\
y\left(t+\frac{\Delta t}{2}\right) &= y(t) + \frac{\Delta t}{2}\,v_y(t)\ , \\
z\left(t+\frac{\Delta t}{2}\right) &= z(t) + \frac{\Delta t}{2}\,v_z(t)\ .
\end{aligned} \tag{4.79}$$

Next, the momentum integration is performed up to second order accuracy

$$\begin{aligned}
p_x\left(t+\Delta t\right) &= p_x\left(t\right) + \frac{q_k\,M}{Q\,m_k}\eta\,\Delta t\left[E_x\left(t+\frac{\Delta t}{2}\right)\right. \\
&\quad \left. + v_y\left(t+\frac{\Delta t}{2}\right) B_z\left(t+\frac{\Delta t}{2}\right) - v_z\left(t+\frac{\Delta t}{2}\right) B_y\left(t+\frac{\Delta t}{2}\right)\right]\ , \\
p_y\left(t+\Delta t\right) &= p_y\left(t\right) + \frac{q_k\,M}{Q\,m_k}\eta\,\Delta t\left[E_y\left(t+\frac{\Delta t}{2}\right)\right. \\
&\quad \left. + v_z\left(t+\frac{\Delta t}{2}\right) B_x\left(t+\frac{\Delta t}{2}\right) - v_x\left(t+\frac{\Delta t}{2}\right) B_z\left(t+\frac{\Delta t}{2}\right)\right]\ , \\
p_z\left(t+\Delta t\right) &= p_z\left(t\right) + \frac{q_k\,M}{Q\,m_k}\eta\,\Delta t\left[E_z\left(t+\frac{\Delta t}{2}\right)\right. \\
&\quad \left. + v_x\left(t+\frac{\Delta t}{2}\right) B_y\left(t+\frac{\Delta t}{2}\right) - v_y\left(t+\frac{\Delta t}{2}\right) B_x\left(t+\frac{\Delta t}{2}\right)\right]\ .
\end{aligned} \tag{4.80}$$

Finally, equations (4.72) are integrated again over half a time step with first order accuracy. However, now the velocities $\vec{v}(t+\Delta t)$ are known yielding overall integration up to second order accuracy

$$\begin{aligned}
x(t+\Delta t) &= x\left(t+\frac{\Delta t}{2}\right) + \frac{\Delta t}{2}\,v_x(t+\Delta t)\ , \\
y(t+\Delta t) &= y\left(t+\frac{\Delta t}{2}\right) + \frac{\Delta t}{2}\,v_y(t+\Delta t)\ , \\
z(t+\Delta t) &= z\left(t+\frac{\Delta t}{2}\right) + \frac{\Delta t}{2}\,v_z(t+\Delta t)\ .
\end{aligned} \tag{4.81}$$

(4.82)

It is now convenient to introduce the following variables [84]

$$\begin{aligned} p_{x/y/z}(t) &= p^-_{x/y/z} - \frac{1}{2}\frac{q_k\,M}{Q\,m_k}\eta\;\Delta t E_{x/y/z}\left(t+\frac{\Delta t}{2}\right)\;, \\ p_{x/y/z}(t+\Delta t) &= p^+_{x/y/z} + \frac{1}{2}\frac{q_k\,M}{Q\,m_k}\eta\;\Delta t E_{x/y/z}\left(t+\frac{\Delta t}{2}\right)\;, \end{aligned} \tag{4.83}$$

where $p_{x/y/z}$ denotes the momenta p_x, p_y, and p_z. A similar convention applies to the electric field. Inserting Equations (4.83) into Equations (4.80) yields

$$\begin{aligned} p^-_x - p^+_x &= -\frac{q_k\,M}{Q\,m_k}\eta\;\Delta t v_y B_z + \frac{q_k\,M}{Q\,m_k}\eta\;\Delta t v_z B_y\;, \\ p^-_y - p^+_y &= -\frac{q_k\,M}{Q\,m_k}\eta\;\Delta t v_z B_x + \frac{q_k\,M}{Q\,m_k}\eta\;\Delta t v_x B_z\;, \\ p^-_z - p^+_z &= -\frac{q_k\,M}{Q\,m_k}\eta\;\Delta t v_x B_y + \frac{q_k\,M}{Q\,m_k}\eta\;\Delta t v_y B_x\;, \end{aligned} \tag{4.84}$$

where we find up to first order accuracy in Δt

$$v_{x/y/z} = \frac{p^+_{x/y/z} + p^-_{x/y/z}}{2\sqrt{1+\left(\frac{p^+_x+p^-_x}{2}\right)^2+\left(\frac{p^+_y+p^-_y}{2}\right)^2+\left(\frac{p^+_z+p^-_z}{2}\right)^2}}\;. \tag{4.85}$$

Thus it follows that

$$\begin{aligned} p^-_x - p^+_x &= -\tau_z(p^+_y + p^-_y) + \tau_y(p^+_z + p^-_z)\;, \\ p^-_y - p^+_y &= -\tau_x(p^+_z + p^-_z) + \tau_z(p^+_x + p^-_x)\;, \\ p^-_z - p^+_z &= -\tau_y(p^+_x + p^-_x) + \tau_x(p^+_y + p^-_y)\;, \end{aligned} \tag{4.86}$$

where τ_x, τ_y and τ_z are defined as

$$\tau_{x/y/z} = \frac{\frac{q_k\,M}{Q\,m_k}\eta\;\Delta t B_{x/y/z}}{2\sqrt{1+\left(\frac{p^+_x+p^-_x}{2}\right)^2+\left(\frac{p^+_y+p^-_y}{2}\right)^2+\left(\frac{p^+_z+p^-_z}{2}\right)^2}}\;. \tag{4.87}$$

Solving for $\vec{p}^{\,+}$ yields

$$\begin{pmatrix} p^+_x \\ p^+_y \\ p^+_z \end{pmatrix} = \mathcal{A}\begin{pmatrix} p^-_x \\ p^-_y \\ p^-_z \end{pmatrix}\;, \tag{4.88}$$

where

$$\mathcal{A} = \begin{pmatrix} \frac{1+\tau_x^2-\tau_y^2-\tau_z^2}{1+\vec{\tau}^2} & \frac{2\tau_x\tau_y+2\tau_z}{1+\vec{\tau}^2} & \frac{2\tau_x\tau_z-2\tau_y}{1+\vec{\tau}^2} \\ \frac{2\tau_x\tau_y-2\tau_z}{1+\vec{\tau}^2} & \frac{1-\tau_x^2+\tau_y^2-\tau_z^2}{1+\vec{\tau}^2} & \frac{2\tau_y\tau_z+2\tau_x}{1+\vec{\tau}^2} \\ \frac{2\tau_x\tau_z+2\tau_y}{1+\vec{\tau}^2} & \frac{2\tau_y\tau_z-2\tau_x}{1+\vec{\tau}^2} & \frac{1-\tau_x^2-\tau_y^2+\tau_z^2}{1+\vec{\tau}^2} \end{pmatrix}\;. \tag{4.89}$$

Equation (4.89) represents a rotation. Therefore it is found up to first order accuracy,

$$\left(\frac{p^+_x+p^-_x}{2}\right)^2+\left(\frac{p^+_y+p^-_y}{2}\right)^2+\left(\frac{p^+_z+p^-_z}{2}\right)^2 = p_x^{-2}+p_y^{-2}+p_z^{-2}\;. \tag{4.90}$$

The updated distribution function is obtained by summing over all quasi-particles representing f_k.

4.3.3 Periodic boundary conditions

After having discussed periodic boundary conditions for the electromagnetic fields in section 4.2.2 we consider periodic boundary conditions for the particles. Periodic boundary conditions leave the momenta of the particles unchanged while their positions change. Let p_{ix}, p_{iy}, p_{iz} denote the x, y, z-components of the momentum of the i-th particle and x_i, y_i, and z_i its position. The positions of the reflecting walls are at $x = x_{min}$, $y = y_{min}$, $z = z_{min}$, $x = x_{max}$, $y = y_{max}$, and $z = z_{max}$. Periodic boundary conditions mean that for $x_i < x_{min}$ the particle has left the simulation box at the left side and re-appears at the right wall:

$$\begin{aligned} x_i &\rightarrow x_i + x_{max} - x_{min} + \Delta x\ , \qquad y_i \rightarrow y_i\ , \qquad z_i \rightarrow z_i\ , \\ p_{ix} &\rightarrow p_{ix}\ , \qquad p_{iy} \rightarrow p_{iy}\ , \qquad p_{iz} \rightarrow p_{iz}\ . \end{aligned} \tag{4.91}$$

whereas $x_i > x_{max}$

$$\begin{aligned} x_i &\rightarrow x_i - x_{max} + x_{min} - \Delta x\ , \qquad y_i \rightarrow y_i\ , \qquad z_i \rightarrow z_i\ , \\ p_{ix} &\rightarrow p_{ix}\ , \qquad p_{iy} \rightarrow p_{iy}\ , \qquad p_{iz} \rightarrow p_{iz}\ . \end{aligned} \tag{4.92}$$

Similarly, for $y_i < y_{min}$

$$\begin{aligned} x_i &\rightarrow x_i\ , \qquad y_i \rightarrow y_i + y_{max} - y_{min} + \Delta y\ , \qquad z_i \rightarrow z_i\ , \\ p_{ix} &\rightarrow p_{ix}\ , \qquad p_{iy} \rightarrow p_{iy}\ , \qquad p_{iz} \rightarrow p_{iz}\ . \end{aligned} \tag{4.93}$$

and for $y_i > y_{max}$

$$\begin{aligned} x_i &\rightarrow x_i\ , \qquad y_i \rightarrow y_i - y_{max} + y_{min} - \Delta y\ , \qquad z_i \rightarrow z_i\ , \\ p_{ix} &\rightarrow p_{ix}\ , \qquad p_{iy} \rightarrow p_{iy}\ , \qquad p_{iz} \rightarrow p_{iz}\ . \end{aligned} \tag{4.94}$$

Finally, for $z_i < z_{min}$

$$\begin{aligned} x_i &\rightarrow x_i\ , \qquad y_i \rightarrow y_i\ , \qquad z_i \rightarrow z_i + z_{max} - z_{min} + \Delta z\ , \\ p_{ix} &\rightarrow p_{ix}\ , \qquad p_{iy} \rightarrow p_{iy}\ , \qquad p_{iz} \rightarrow p_{iz}\ . \end{aligned} \tag{4.95}$$

and for $z_i > z_{max}$

$$\begin{aligned} x_i &\rightarrow x_i\ , \qquad y_i \rightarrow y_i\ , \qquad z_i \rightarrow z_i - z_{max} + z_{min} - \Delta z\ , \\ p_{ix} &\rightarrow p_{ix}\ , \qquad p_{iy} \rightarrow p_{iy}\ , \qquad p_{iz} \rightarrow p_{iz}\ . \end{aligned} \tag{4.96}$$

4.3.4 Reflecting boundary conditions

Reflecting boundary conditions are defined by inverting the momenta of quasi-particles at the reflecting wall in the direction normal to the wall. The position of the quasi-particles is also changed. Let p_{ix}, p_{iy}, p_{iz} denote the x, y, z-components of the momentum of the i-th particle and x_i, y_i, and z_i its position. The positions of the 6 reflecting planar walls are $x = x_{min}$, $y = y_{min}$, $z = z_{min}$, $x = x_{max}$, $y = y_{max}$, and $z = z_{max}$. Reflecting boundary conditions mean that for $x_i < x_{min}$ we have to replace

$$\begin{aligned} x_i &\rightarrow 2\,x_{min} - x_i\ , \qquad y_i \rightarrow y_i\ , \qquad z_i \rightarrow z_i\ , \\ p_{ix} &\rightarrow -p_{ix}\ . \qquad p_{iy} \rightarrow p_{iy}\ , \qquad p_{iz} \rightarrow p_{iz}\ . \end{aligned} \tag{4.97}$$

whereas for $x_i > x_{max}$

$$\begin{aligned} x_i &\rightarrow 2\,x_{max} - x_i\ , \qquad y_i \rightarrow y_i\ , \qquad z_i \rightarrow z_i\ , \\ p_{ix} &\rightarrow -p_{ix}\ . \qquad p_{iy} \rightarrow p_{iy}\ , \qquad p_{iz} \rightarrow p_{iz}\ . \end{aligned} \tag{4.98}$$

For $y_i < y_{min}$ holds

$$\begin{aligned} x_i &\rightarrow x_i \;, \qquad y_i \rightarrow 2\,y_{min} - y_i \;, \qquad z_i \rightarrow z_i \;, \\ p_{ix} &\rightarrow p_{ix} \;. \qquad p_{iy} \rightarrow -p_{iy} \;, \qquad p_{iz} \rightarrow p_{iz} \;. \end{aligned} \tag{4.99}$$

and for $y_i > y_{max}$

$$\begin{aligned} x_i &\rightarrow x_i \;, \qquad y_i \rightarrow 2\,y_{max} - y_i \;, \qquad z_i \rightarrow z_i \;, \\ p_{ix} &\rightarrow p_{ix} \;. \qquad p_{iy} \rightarrow -p_{iy} \;, \qquad p_{iz} \rightarrow p_{iz} \;. \end{aligned} \tag{4.100}$$

Finally, for $z_i < z_{min}$

$$\begin{aligned} x_i &\rightarrow x_i \;, \qquad y_i \rightarrow y_i \;, \qquad z_i \rightarrow 2\,z_{min} - z_i \;, \\ p_{ix} &\rightarrow p_{ix} \;. \qquad p_{iy} \rightarrow p_{iy} \;, \qquad p_{iz} \rightarrow -p_{iz} \;. \end{aligned} \tag{4.101}$$

and for $z_i > z_{max}$

$$\begin{aligned} x_i &\rightarrow x_i \;, \qquad y_i \rightarrow y_i \;, \qquad z_i \rightarrow 2\,z_{min} - z_i \;, \\ p_{ix} &\rightarrow p_{ix} \;. \qquad p_{iy} \rightarrow p_{iy} \;, \qquad p_{iz} \rightarrow -p_{iz} \;. \end{aligned} \tag{4.102}$$

The reflecting boundary conditions are not yet implemented in a charge conserving way in the PSC. This is left for the future. The module **PIC_move_part.f** solves the Vlasov equation. The module calls **PIC_pex.f**, **PIC_pey.f**, and **PIC_pez.f** in which the boundary conditions are defined.

4.4 The Vlasov-Boltzmann equation

Up to now we have described the collective propagation of the particle distribution functions f_k under the action of the Lorentz force. Now we take binary collisions into account. We will see that the direct integration of the Boltzmann collision operator requires of the order N^2 operations, where N is the total number of quasi-particles used to represent the distribution functions. Hence, the direct integration of the Vlasov-Boltzmann equation becomes quickly impractical. In the following subsections we present a collision model based on finite phase space elements that retains as many features of the Vlasov-Boltzmann equation given in section 3.2 as is possible while the number of operations required to perform binary collisions scales as N. The model is based on a Monte-Carlo algorithm and essentially consists of rules for selecting representative pairs of colliding quasi-particles, of rules for determining the frequency between collisions, and of rules for the associated scattering parameters obeying energy and momentum conservation.

4.4.1 Equations of motion

In section 4.3.2 we have derived equations of motion for quasi-particles that represented the Vlasov equation. For the collision model similar equations of motion for quasi-particles representing the Vlasov-Boltzmann equation are required. We start our considerations by making use of the Boltzmann collision integral for immobile ions given by Eqn. (3.24). We find in three notation

$$\frac{c}{p_e^0}\,C_{ei} \;=\; n_i\,|\vec{v}|\int d\Omega_\psi\;\sigma_{ei}(s,\psi)\;\left(f_e^{\,\prime}-f_e\right)\;. \tag{4.103}$$

Next, we multiply the Vlasov-Boltzmann equation by the momentum $\vec{p}$ and integrate over momentum space, which yields

$$\begin{aligned}\partial_t \int d^3p\, \vec{p}\, f_e + \frac{\partial}{\partial x_l} \int d^3p\, v_l\, \vec{p}\, f_e \\ - \int d^3p\, \frac{\partial}{\partial v_l} \left(q\, [\vec{E} + \vec{v} \times \vec{B}]_l\, \vec{p} \right)\, f_e \\ = n_i \int d\Omega_\psi \int d^3p\, \sigma_{ei}(s,\psi)\, \vec{p}|\vec{v}|\, \left(f_e^{'} - f_e \right) .\end{aligned} \tag{4.104}$$

Inserting Eqn. (4.62) into Eqn. (4.104) and performing the momentum integrations it follows

$$\begin{aligned}\sum_{j=1}^{N_k} \left(\dot{\vec{x}}_j \cdot \frac{\partial \phi(\vec{x},\vec{x}_j)}{\partial \vec{x}_j} + \vec{v}_j \cdot \frac{\partial \phi(\vec{x},\vec{x}_j)}{\partial \vec{x}} \right) \vec{p}_j \\ + \sum_{j=1}^{N_k} \left(\dot{\vec{p}}_j - q\, [\vec{E} + \vec{v}_j \times \vec{B}] \right)\, \phi(\vec{x},\vec{x}_j) \\ = \sum_{j=1}^{N_k} n_i\, |\vec{v}_j| \int d\Omega_\psi\, \sigma_{ei}(s,\psi)\, \left(\vec{p}_j^{\,'} - \vec{p}_j \right)\, \phi(\vec{x},\vec{x}_j) .\end{aligned} \tag{4.105}$$

The collision operator in Eqn. (4.105) can be further simplified. Performing the integration over scattering angles we find

$$\begin{aligned}n_i\, |\vec{v}_j| \int d\Omega_\psi\, \sigma_{ei}(s,\psi)\, \left(\vec{p}_j^{\,'} - \vec{p}_j \right)\, \phi(\vec{x},\vec{x}_j) \\ = -\frac{e_e^2 e_i^2\, \vec{p}_j}{4\pi\epsilon_0^2\, m_e^2\, v_j^3}\, \ln \frac{\psi_{max}}{\psi_{min}}\, \phi(\vec{x},\vec{x}_j)\, n_i(\vec{x},t) .\end{aligned} \tag{4.106}$$

For quasi-particles that are symmetric in their arguments, the equations of motion, which now contain an additional drag term due to collisions, become

$$\frac{d\vec{x}_j}{dt} = \vec{v}_j , \tag{4.107}$$

$$\begin{aligned}\frac{d\vec{p}_j}{dt} = \frac{1}{\Pi_{l=1}^3 \Delta x_l} \left[q \int_V d^3x\, \phi(\vec{x} - \vec{x}_j)\, [\vec{E}(\vec{x},t) + \vec{v}_j \times \vec{B}(\vec{x},t)] \right. \\ \left. - \frac{e_e^2 e_i^2\, \vec{p}_j}{4\pi\epsilon_0^2\, m_e^2\, v_j^3}\, \ln \frac{\psi_{max}}{\psi_{min}} \int_V d^3x\, \phi(\vec{x} - \vec{x}_j)\, n_i(\vec{x},t) \right] .\end{aligned} \tag{4.108}$$

Equation (4.108) shows that the collision frequency enters the equations of motion for the quasi-particles. An explicit representation for Eqn. (4.108) as the one given by Eqn. (4.76) can be calculated.

We now consider the nonlinear fully relativistic Vlasov-Boltzmann equation given by

$$\frac{df_k}{dt} = \sum_l \frac{2 - \delta_{kl}}{2} \int d^3p_l\, v^{kl} \int d\Omega_\psi\, \sigma^{kl}(s,\psi)\, \left(f_k^{'} f_l^{'} - f_k f_l \right) . \tag{4.109}$$

After multiplication of both sides with $\vec{p}_i^{\,k}$, insertion of the finite element representations for f_k and f_l and integration over the momentum space d^3p^k we obtain

$$\sum_{i=1}^{N_k} \left(\dot{\vec{x}}_i^{\,k} \cdot \frac{\partial \phi(\vec{x},\vec{x}_i^{\,k})}{\partial \vec{x}_i^{\,k}} + \vec{v}_i^{\,k} \cdot \frac{\partial \phi(\vec{x},\vec{x}_i^{\,k})}{\partial \vec{x}} \right) \vec{p}_i^{\,k} \tag{4.110}$$

$$+\sum_{i=1}^{N_k}\left(\dot{\vec{p}}_i^{\,k}-q\left[\vec{E}+\vec{v}_i^{\,k}\times\vec{B}\right]\right)\,\phi(\vec{x},\vec{x}_i^{\,k})$$
$$=\sum_l\frac{n_0}{N_c}\left(1-\frac{\delta_{kl}}{2}\right)\sum_{i,j=1}^{N_kN_l}v_{ij}^{kl}\int d\Omega_\psi\,\sigma_{ij}^{kl}(s,\psi)\,\left(\vec{p}_i^{\,\prime k}-\vec{p}_i^{\,k}\right)\,\phi(\vec{x},\vec{x}_i^{\,k})\,\phi(\vec{x},\vec{x}_j^{\,l})\;,$$

where $i\neq j$ is implied for the double summations. Integrating over d^3x and requiring symmetric form factors of the quasi-particles we find

$$\frac{d\vec{x}_i^{\,k}}{dt} = \vec{v}_i^{\,k}\;, \tag{4.111}$$
$$\frac{d\vec{p}_i^{\,k}}{dt} = \frac{1}{\Pi_{n=1}^3\Delta x_n}\left[q\int_V d^3x\,\phi(\vec{x}-\vec{x}_i^{\,k})\,[\vec{E}(\vec{x},t)+\vec{v}_i^{\,k}\times\vec{B}(\vec{x},t)]\right. \tag{4.112}$$
$$+\sum_l\left(1-\frac{\delta_{kl}}{2}\right)\sum_{j=1}^{N_l}v_{ij}^{kl}\int d\Omega_\psi\,(\vec{p}_i^{\,\prime k}-\vec{p}_i^{\,k})\,\sigma_{ij}^{kl}(s,\psi)$$
$$\left.\times\frac{n_0}{N_c}\int_V d^3x\,\phi(\vec{x}-\vec{x}_i^{\,k})\,\phi(\vec{x}-\vec{x}_j^{\,l})\right]\;.$$

With the kinematic relations given by Eqns. (3.15) and (3.18) we have a complete set of equations. However, the direct solution of Eqns. (4.111) and (4.112) is not practical without further simplifications since it requires of the order $N_k\cdot N_l$ operations.

4.4.2 The collisional model

First collision models for particle codes, as is the PSC, have been devised in [74, 75]. Here we try to motivate a similar collision model that requires of the order N operations following closely Eqn. (4.112). As the latter equation shows it is necessary to determine particle pairs that overlap in a given spatial cell of the grid in order to have collisional interaction. The integral over the volume V in Eqn. (4.112) can be evaluated. However, for reasons of simplicity we assume that

$$\frac{1}{\Pi_{n=1}^3\Delta x_n}\int_V d^3x\,\phi(\vec{x}-\vec{x}_i^{\,k})\,\phi(\vec{x}-\vec{x}_j^{\,l}) = \begin{cases}1\;, & \vec{x}_i,\vec{x}_j\in V\\ 0\;, & else\end{cases}\;. \tag{4.113}$$

holds. We assume further that the number of particles of sorts k and l, for which Eqn. (4.113) is fulfilled, are N_{ck} and N_{cl}.

To find quasi-particles that belong to the same cell we assign the cell number the particle is in to each particle. Next, we assume that the simultaneous interaction of all $N_{ck}\cdot N_{cl}$ possible collision pairs can be approximated by the interaction of a few randomly selected representative particle pairs. To find random colliding pairs, uniformly distributed random permutations of particle labels are generated. After that particles are assigned to their cells and pairs are selected in consecutive order. Their post-collision momenta are determined with the help of the kinematic relations of relativistic binary collisions. Collisions between different species are assumed to occur successively. We also assume that particle acceleration and collisions do not occur at the same time as is implied by Eqns. (4.111) and (4.112) but can be decoupled. After these approximations we obtain for the mean field part (mf) of the equations of motion

$$\left.\frac{d\vec{x}_i^{\,k}}{dt}\right|_{\rm mf} = \vec{v}_i^{\,k}\;, \tag{4.114}$$

$$\left.\frac{d\vec{p}_i^{\,k}}{dt}\right|_{\rm mf} \;=\; \frac{q}{\Pi_{n=1}^3 \Delta x_n}\int_V d^3x\,\phi(\vec{x}-\vec{x}_i^{\,k})\,[\vec{E}(\vec{x},t)+\vec{v}_i^{\,k}\times\vec{B}(\vec{x},t)]\;. \qquad (4.115)$$

To assign particle pairs for the Monte-Carlo method we assume without lack of generality that $k \neq l$ and $N_{cl} < N_{ck}$ hold. We select N_{ck} colliding particle pairs of sorts k and l such that each of the N_{cl} particles of sort l is assigned to as few particles of sort k as is possible while each of the N_{ck} particles of sort k is assigned to exactly one particle of sort l. The situation is illustrated in Fig. 4.2. We assume that the corresponding collision events

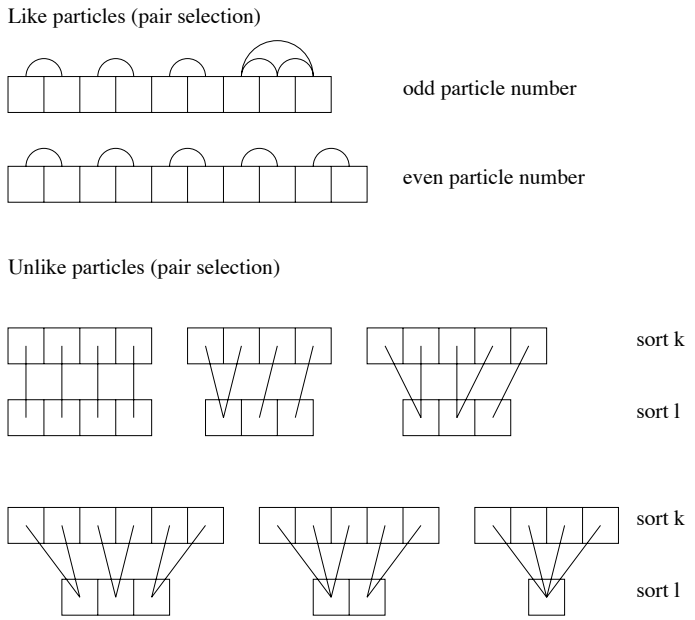

Figure 4.2: The figure shows collision pairs for like particles ($k = l$) and unlike particles ($k \neq l$). For like particles two cases have to be considered. Case one is for an odd number of particles. The pairing rules are shown in the figure. Since the last three particles undergo twice as many collisions than the others the corresponding collision frequencies are divided by two. Case two holds for an even number of particles and is also depicted in the figure. Pairing rules are more complicated for a combination of like and unlike particles. Rather than giving the general algorithm used in PSC we show a few representative examples from which the general case can be derived using the explanations given in the text into consideration.

between selected particle pairs are representative for all possible collisions N_{ck} particles of sort k can undergo with N_{cl} particles of sort l. An illustration is given in Fig. 4.3, where all possible particle pairs for collisions between $N_{ck} = 8$ electrons (small disks) and $N_{cl} = 4$ ions (large disks) are depicted. The assumption is that all $8 \cdot 4 = 32$ scattering events between electrons and ions can be represented by only four representative scattering events indicated by particle pairs that are linked by bold solid lines in the figure. Since in reality the binary interaction of N_{ck} particles of sort k and N_{cl} particles of sort l results in many successive, however independent, small angle scattering events, we assume that the cumulative square momentum change Δp_i^{k2} for the i-th particle of sort k has a Gaussian distribution, the width of which is approximately given by $p_i^{k2}\,\nu_{ij}^{kl}\,\Delta t$. Here $\vec{p}_i^{\,k}$ is the initial momentum of the i-th

particle of sort k and ν_{ij}^{kl} the collision frequency between the latter and the j-th particle of sort l, while Δt is the time increment at which the simulation proceeds. Further details follow later.

Let us now assume that $k = l$ holds. In this case only of the order $N_{ck}/2$ colliding pairs are selected as is implied by Eqn. (4.112). Again multiple pair assignments for quasi-particles have to be avoided whenever possible. We distinguish between the cases of even and odd particle numbers N_{ck}. In the case when N_{ck} is even there are no multiple pair assignments for individual particles. If, however, N_{ck} is odd there are a few. Details are given in Fig. 4.2. The pair selection method described here leads to the order of N operations for collisions in the code.

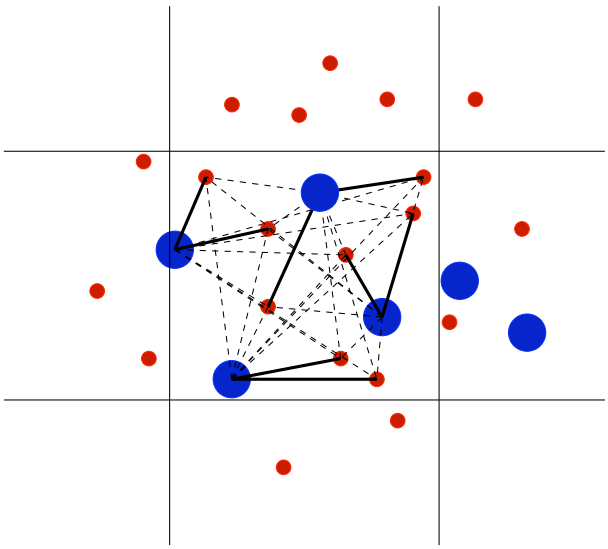

Figure 4.3: The figure shows electron-ion pairing in an elementary cell of the grid that holds $N_{ck} = 8$ electrons (small disks) and $N_{cl} = 4$ ions (large disks). Representative particle pairs are connected by bold solid lines. They are obtained with the help of the selection rules for colliding particle pairs. The change of momentum between the representative electron-ion pairs due to collisions is enhanced by a factor of four because each electron would form pairs with three other ions in a complete Boltzmann collision process. All possible electron-ion pairs are linked by solid and dashed lines in the figure.

As discussed we need to find an approximation for the rate of change of the mean square particle momenta p_i^{k2} with time. Recalling our earlier discussion we find

$$\left.\frac{d\vec{p}_i^{\,k}}{dt}\right|_{\rm bin} = \sum_l \left(1 - \frac{\delta_{kl}}{2}\right) \sum_{j=1}^{N_{cl}} \frac{n_0}{N_c}\, v_{ij}^{kl} \int d\Omega_\psi \,(\vec{p}_i^{\,\prime k} - \vec{p}_i^{\,k})\, \sigma_{ij}^{kl}(s,\psi)\;, \qquad (4.116)$$

where $i = 1, ..., N_{ck}$ holds. We now consider the case $k \neq l$ and $N_{cl} < N_{ck}$. For each particle $i = 1, ..., N_{ck}$ we assign a unique randomly selected partner in a way that each particle $j = 1, ..., N_{cl}$ has as few multiple pair assignments as is possible. This way we obtain $m = 1, ..., N_{ck}$ particle pairs. We assume that each pair $m = 1, ..., N_{ck}$ is representative for

all $N_{cl}-1$ abandoned particle pairs in Eqn. (4.116). We further assume that all selected collisions can be carried out successively. This means that the post-collisional momenta of collision process one can become the pre-collision momenta of the successive collision process two. The scattering angles, however, are assumed to be uncorrelated. Equation (4.116) then becomes

$$\left.\frac{d\vec{p}_m^{\,k}}{dt}\right|_{\rm bin} = \frac{N_{cl}\,n_0}{N_c}\,v_{mm}^{kl}\int d\Omega_\psi\,(\vec{p}_m^{\,'k}-\vec{p}_m^{\,k})\,\sigma_{mm}^{kl}(s,\psi) \tag{4.117}$$

for all possible combinations k and l. To proceed we transform into the center of mass frame of the particle pair m under consideration and calculate the differential cross section. With the help of Eqns. (3.13) and (3.17) we find in the non-relativistic limit $m_k c \gg |\vec{p}^{\,k}|$ and $m_l c \gg |\vec{p}^{\,l}|$

$$\sigma_{mm}^{kl}(s,\psi) = \frac{e_k^2 e_l^2}{64\pi^2\epsilon_0^2\,m_R^2\,(v_{mm}^{kl})^4\,\sin^4\frac{\psi}{2}}\,, \tag{4.118}$$

where the relations

$$v_{mm}^{kl}=|\vec{v}_m^{\,k}-\vec{v}_m^{\,l}|\,,\qquad m_R=\frac{m_k m_l}{m_k+m_l} \tag{4.119}$$

hold. The remaining angle integrations can be carried out. With the help of Eqns. (3.18) and (3.19) we find

$$\int d\nu\,(\vec{p}_m^{\,'k}-\vec{p}_m^{\,k}) = 2\pi\,\vec{p}_m^{\,k}\,(\cos\psi-1)\ . \tag{4.120}$$

Performing the angle integration over ψ we obtain for the rate of change of the momentum $\vec{p}_m^{\,k}$ in the small scattering angle limit

$$\frac{d\vec{p}_m^{\,k}}{dt} = -\frac{N_{cl}\,n_0}{N_c}\,\frac{e_k^2 e_l^2}{4\pi\epsilon_0^2\,m_R^2\,(v_{mm}^{kl})^3}\,\ln\left(\frac{\psi_{min}}{\psi_{max}}\right)\,\vec{p}_m^{\,k}\,. \tag{4.121}$$

The angles ψ_{min} and ψ_{max} are cut-off angles that are required because the integral over ψ in Eqn. (4.116) diverges. The logarithm in Eqn. (4.121) is the so-called Coulomb logarithm. An open question is, which value has to be taken for the latter. Frequently $\ln(\psi_{max}/\psi_{min}) = \ln(v/wb_\perp)$ is used, where $w=\max(\omega_{pe},\omega)$, $v=\sqrt{v_{th}^2+v_{os}^2}$, and $b_\perp$ is the impact parameter for perpendicular deflection. The oscillation velocity v_{os}^2 has to be cut off at about $4\,v_{th}^2$. For a detailed discussion see [76, 77, 78]. We currently keep the Coulomb logarithm constant in the PSC. Multiplying Eqn. (4.121) with $\vec{p}_m^{\,k}$ and performing the time integration for small time intervals Δt implies

$$\frac{\Delta p_m^{k2}}{p_m^{k2}} = 2\,\nu_{mm}^{kl}\Delta t \tag{4.122}$$

for the square momentum change of the particle under consideration [1]. We have defined the collision frequency between the m-th particle of sort k and the m-th particle of sort l as

$$\nu_{mm}^{kl} = \frac{N_{cl}\,n_0}{N_c}\,\frac{e_k^2 e_l^2}{4\pi\,\epsilon_0^2\,m_R^2\,(v_{mm}^{kl})^3}\,\ln\left(\frac{\psi_{max}}{\psi_{min}}\right)\,. \tag{4.123}$$

[1] The time interval Δt is strictly speaking the one in the center of mass frame. However, we do not distinguish between center of mass frame time and lab frame time in the PSC

It is important to note that the particle density required to calculate the collision frequency ν_{mm}^{kl} in the numerical code is $N_{cl}\, n_0/N_c$, where $N_{cl} < N_{ck}$ must hold. For $k \neq l$ and $N_{ck} < N_{cl}$ we have to exchange labels k and l. For $k = l$ we have to replace N_{cl} by $N_{ck}/2$. Since all particle momenta have to be represented in the lab frame we have to boost into the center of mass frame of the selected colliding pairs, perform the collisions and boost back into the lab frame.

4.4.3 Scattering angles for Rutherford scattering

We assume that $\Delta p_m^k \ll p_m^k$ holds for each scattering event, where $\vec{p}_m^{\,k}$ is the center of mass frame momentum of the m-th particle of sort k undergoing collisions with particles of sort l. Then, the momentum deflection Δp_m^k calculated in section 4.4.2 can be used as an approximation to the magnitude of the momentum deflection normal to $\vec{p}_m^{\,k}$. As a consequence, an approximation to the deflection angle ψ for a small angle scattering event is given by $\tan(\psi/2) \approx \Delta p_m^k / 2p_m^k$.

We assume that the deflections $\Delta p_m^k = 2p_m^k \tan\psi/2$ have a Gaussian distribution normal to $\vec{p}_m^{\,k}$, the width of which is given by Δp_m^{k2} derived in Eqn. (4.122). Since $\Delta\vec{p}_m^{\,k}$ is normal to $\vec{p}_m^{\,k}$, two parameters are required to determine $\Delta\vec{p}_m^{\,k}$. They are the length Δp_m^k and the angle ν about $\vec{p}_m^{\,k}$. Substituting $r = \nu$ and $s = \Delta p_m^k$ we find for the scattering probabilities P_ψ and Q_ν

$$P_\psi = \frac{1}{2\pi\, p_m^{k2}\, \nu_{mm}^{kl} \Delta t} \int_0^{2\pi} dr \int_0^{2\, p_m^k\, \tan\frac{\psi}{2}} ds\, s\, \exp\left(-\frac{s^2}{2\, p_m^{k2}\, \nu_{mm}^{kl} \Delta t}\right) , \quad (4.124)$$

$$Q_\nu = \frac{1}{2\pi\, p_m^{k2}\, \nu_{mm}^{kl} \Delta t} \int_0^{\nu} dr \int_0^{\infty} ds\, s\, \exp\left(-\frac{s^2}{2\, p_m^{k2}\, \nu_{mm}^{kl} \Delta t}\right) . \quad (4.125)$$

Integration and resolving for ν and ψ leads to

$$\nu = 2\,\pi\, Q_\nu , \qquad \psi = 2\, \tan^{-1}\left(\sqrt{-\frac{\nu_{mm}^{kl}\, \Delta t}{2}\, \ln\left(1 - P_\psi\right)}\right) , \quad (4.126)$$

where $0 \leq P_\psi < 1$ and $0 \leq Q_\nu < 1$ hold and the collision frequencies are given by Eqn. (4.123). For large scattering angles we assume a uniform angle distribution

$$P_\psi = \frac{1}{4\pi} \int_0^{2\pi} dr \int_0^{\psi} ds\, \sin s , \qquad Q_\nu = \frac{1}{4\pi} \int_0^{\nu} dr \int_0^{\pi} ds\, \sin s , \quad (4.127)$$

resulting in

$$\nu = 2\,\pi\, Q_\nu , \qquad \psi = \cos^{-1}\left(1 - 2\, P_\psi\right) , \quad (4.128)$$

where again $0 \leq Q_\nu < 1$ and $0 \leq P_\psi < 1$ hold.

4.4.4 Relativistic binary kinematics

The numerical collision model in section 4.4.2 can only be correct if the particles selected randomly for collisions are scattered into the correct phase space elements. We now derive the kinematics of binary scattering events in a covariant frame work. In what follows we drop all labels that are not required. The colliding particles retain the labels 1 and 2. In the following we transform into the center of mass frame, determine the scattering angles

in the latter, and finally transform back into the lab system. The pre-collision momenta in the CM-frame are

$$\begin{aligned} p_{01}^{cm} &= \sqrt{m_1^2 c^2 + |\vec{p}|^2}\,, \\ \vec{p}_1^{\,cm} &= \vec{p}_1 + (\gamma - 1)\,(\vec{p}_1 \cdot \vec{n})\,\vec{n} - \gamma\,\vec{\beta}\,p_{01}\,, \\ p_{02}^{cm} &= \sqrt{m_2^2 c^2 + |\vec{p}|^2}\,, \\ \vec{p}_2^{\,cm} &= -\vec{p}_1^{\,cm}\,, \end{aligned} \tag{4.129}$$

where

$$|\vec{p}| \;=\; \frac{1}{2\sqrt{s}}\sqrt{\left(s - (m_1^2 + m_2^2)\,c^2\right)^2 - 4\,m_1^2 m_2^2\,c^4}\,. \tag{4.130}$$

The pre-collision masses of the colliding particles are m_1 and m_2 and $s = (p_1 + p_2)^2$, where p_1 and p_2 denote the pre-collision four momenta in the lab frame. For $\vec{\beta}$, $\vec{n}$, and γ we find

$$\vec{\beta} = \frac{\vec{p}_1 + \vec{p}_2}{p_{01} + p_{02}}\,, \qquad \vec{n} = \frac{\vec{\beta}}{|\vec{\beta}|} \qquad \gamma = \frac{1}{\sqrt{1 - \beta^2}}\,, \tag{4.131}$$

where $\vec{\beta}$ is the normalized center of mass frame velocity. To define the post-collision momenta we introduce a right-handed coordinate system depicted in Fig. 3.1, the z-axis of which is along $\vec{p}_1^{\,cm}$. We find for all three coordinate axes

$$\vec{e}_1 = \frac{\vec{p}_1^{\,cm}}{|\vec{p}_1^{\,cm}|}\,, \qquad \vec{e}_2 = \frac{\vec{p}_1^{\,cm} \times \vec{e}_z}{|\vec{p}_1^{\,cm} \times \vec{e}_z|}\,, \qquad \vec{e}_3 = \frac{(\vec{p}_1^{\,cm} \times \vec{e}_z) \times \vec{p}_1^{\,cm}}{|(\vec{p}_1^{\,cm} \times \vec{e}_z) \times \vec{p}_1^{\,cm}|}\,. \tag{4.132}$$

We select two scattering angles ν and ψ as is indicated in Fig. 4.4. They are determined with the help of the event generators Eqns. (4.126) for small scattering angles or (4.128) for large ones. If $s \geq (m_3 c + m_4 c)^2$ holds, where m_3 and m_4 denote the post-collision masses of the particles, we can calculate the post-collision momenta in the CM-frame variables. We obtain

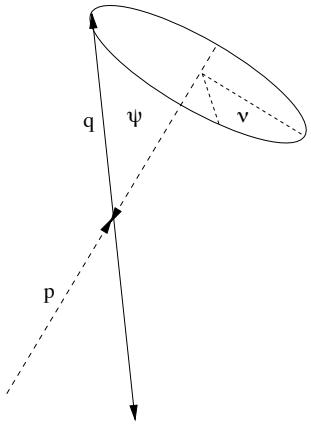

Figure 4.4: Pre- and post collision momenta $\vec{p}$ and $\vec{q}$ in the center of mass system. The angles ψ and ν are determined with the help of random numbers as explained in section 4.4.3.

$$
\begin{aligned}
p_{03}^{cm} &= \sqrt{m_3^2 c^2 + |\vec{q}|^2}\,, \\
\vec{p}_3^{\,cm} &= |\vec{q}|\,\cos\psi \vec{e}_1 + |\vec{q}|\,\sin\psi\,\sin\nu\,\vec{e}_2 + |\vec{q}|\,\sin\psi\,\cos\nu\,\vec{e}_3\,, \\
p_{04}^{cm} &= \sqrt{m_4^2 c^2 + |\vec{q}|^2}\,, \\
\vec{p}_4^{\,cm} &= -\vec{p}_3^{\,cm}\,,
\end{aligned}
\tag{4.133}
$$

where q is given by

$$
|\vec{q}| = \frac{1}{2\sqrt{s}}\sqrt{\left(s-(m_3^2+m_4^2)\,c^2\right)^2 - 4\,m_3^2 m_4^2\,c^4}\,. \tag{4.134}
$$

Finally we transform back into the lab-frame and obtain

$$
\begin{aligned}
p_{03} &= \gamma\,\left(\vec{p}_{03}^{\,cm} + \vec{\beta}\cdot\vec{p}_3^{\,cm}\right)\,, \\
\vec{p}_3 &= \vec{p}_3^{\,cm} + (\gamma-1)\,(\vec{p}_3^{\,cm}\cdot\vec{n})\,\vec{n} + \gamma\,\vec{\beta}\,p_{03}^{cm}\,, \\
p_{04} &= \gamma\,\left(\vec{p}_{04}^{\,cm} + \vec{\beta}\cdot\vec{p}_4^{\,cm}\right)\,, \\
\vec{p}_4 &= \vec{p}_4^{\,cm} + (\gamma-1)\,(\vec{p}_4^{\,cm}\cdot\vec{n})\,\vec{n} + \gamma\,\vec{\beta}\,p_{04}^{cm}\,.
\end{aligned}
\tag{4.135}
$$

At this point we have the post-collision momenta in the lab frame again. Note that the masses of the colliding particles can change freely. However, energy and momentum are conserved.

4.4.5 Required time resolution and grid size

An important issue to be addressed is the correct time resolution and grid size. The time resolution depends on the magnitude of the collision frequencies. We require that $\nu_{mm}^{kl}\,\Delta t \leq 1$ for all quasi-particle pairs and $|f/\partial_t f| \gg \Delta t$, where f is an arbitrary field in the simulation. Since the Boltzmann collision operator is local in space, the cell size of the grid has no direct meaning for the collisional interaction range between two physical particles in a plasma. The cell size has direct implications for plasma related scales, since $|f/\partial_x f| \gg \Delta x$, $|f/\partial_y f| \gg \Delta y$, and $|f/\partial_z f| \gg \Delta z$ must hold. However, the distance between two quasi-particles matters in the sense that the integral over the volume of an elementary cell in Eqn. (4.113) disappears almost always in case they are too far apart on average. This means that the distribution functions f_k are not adequately approximated by quasi-particles and many more quasi-elements may be required. The average distance between physical particles enters the collision frequencies directly via the Coulomb logarithm. The latter contains lower and upper cut-offs for the impact parameter for Coulomb scattering and determines the frequency at which binary collisions are carried out.

We obtain normalized units by introducing $\nu_{mm}^{kl} \to \nu_{mm}^{kl}/\omega$ for the normalized collision frequencies, $\vec{p} \to \vec{p}/m_k c$ for the normalized momenta, and $\Delta t \to \omega\,\Delta t$ for the normalized time increment. In the PSC binary collisions are calculated with **PIC_bin_coll.f**. The parameters required for the collision module to work properly are set in the initialization modules **INIT_param.f** and **INIT_idistr.f**. They are listed in section 5.1.

4.5 Currents

For rigorous charge conservation the current densities are obtained from the variation of the charge density with respect to the particle motion. For simple weight functions nu-

merical methods are described in [79, 80, 81]. Conventional methods for improving charge conservation are described in [82, 83].

4.5.1 Mass distribution of a quasi-particle

Since the distribution function is a linear superposition of all quasi-particles a single quasi-particle will be considered in the following. The total mass contribution of a single quasi-particle located at $\vec{x}_i$ to the spatial grid with nodes at $j\Delta x$, $k\Delta y$, $l\Delta z$ is obtained by the following expression

$$\begin{aligned}\sum_{jkl} \Delta x\Delta y\Delta z\, \zeta_{jkl}(\vec{x}_i) \qquad (4.136)\\ = \sum_{jkl} \int_{x_j-\frac{\Delta x}{2}}^{x_j+\frac{\Delta x}{2}} dw_1 \int_{y_k-\frac{\Delta y}{2}}^{y_k+\frac{\Delta y}{2}} dw_2 \int_{z_l-\frac{\Delta z}{2}}^{z_l+\frac{\Delta z}{2}} dw_3\ \phi(\vec{x}_i-\vec{w})\ ,\end{aligned}$$

where $\zeta_{jkl}(\vec{x}_i)$ is the mass distribution of a quasi-particle at $\vec{x}_i$ over the nodes at $j\,\Delta x$, $k\,\Delta y$, and $l\,\Delta z$ of the grid. For illustration the integration domain in the xy-plane in Eqn. (4.136) is depicted by the square in the upper part of Fig. 4.5. By comparison we require

$$\begin{aligned}\zeta_{jkl}(\vec{x}_i) = \zeta_{1j}(x_i)\,\zeta_{2k}(y_i)\,\zeta_{3l}(z_i) \qquad (4.137)\\ = \frac{1}{\Delta x\Delta y\Delta z} \int_{x_j-\frac{\Delta x}{2}}^{x_j+\frac{\Delta x}{2}} dw_1 \int_{y_k-\frac{\Delta y}{2}}^{y_k+\frac{\Delta y}{2}} dw_2 \int_{z_l-\frac{\Delta z}{2}}^{z_l+\frac{\Delta z}{2}} dw_3\ \phi(\vec{x}_i-\vec{w})\ .\end{aligned}$$

We calculate $\zeta_{1j}(x_i)$ for the triangular form factor ϕ centered at x_i. We find

$$\zeta_{1j}(x_i) = \frac{1}{\Delta x} \int_{x_j-\frac{\Delta x}{2}}^{x_j+\frac{\Delta x}{2}} dw\, S_1(x_i-w)\ , \qquad (4.138)$$

$$S_1(x_i-w) = \begin{cases} 1-\frac{|x_i-w|}{\Delta x}\ , & |x_i-w|\le\Delta x \\ 0\ , & else \end{cases}\ . \qquad (4.139)$$

The integral in Eqn. (4.138) is readily evaluated to yield

$$\zeta_{1j}(x_i) = \begin{cases} 0\ , & |x_i-x_j| > \frac{3\Delta x}{2} \\ \frac{1}{2}\left(\frac{3}{2}-\frac{|x_i-x_j|}{\Delta x}\right)^2\ , & \frac{\Delta x}{2} < |x_i-x_j| \le \frac{3\Delta x}{2} \\ \frac{3}{4}-\frac{|x_i-x_j|^2}{\Delta x^2}\ , & |x_i-x_j| \le \frac{\Delta x}{2} \end{cases}\ . \qquad (4.140)$$

Figure 4.5 is helpful to understand the integration boundaries. Equation (4.140) is the same as the form factor Eqn. (4.77) required for force interpolation. The 3D mass density is the product of the mass densities in 1D for each coordinate direction.

4.5.2 The current conserving scheme

A current conserving scheme is easily motivated for a particle moving in only one direction, which we pick to be the x-direction. Then, we obtain with the help of Eqn. (4.20)

$$j^{n+1}_{x,j+\frac{1}{2}kl} = j^{n+1}_{x,j-\frac{1}{2}kl} + \frac{\Delta x}{\Delta t}\left(\rho^{n+\frac{3}{2}}_{jkl} - \rho^{n+\frac{1}{2}}_{jkl}\right)\ . \qquad (4.141)$$

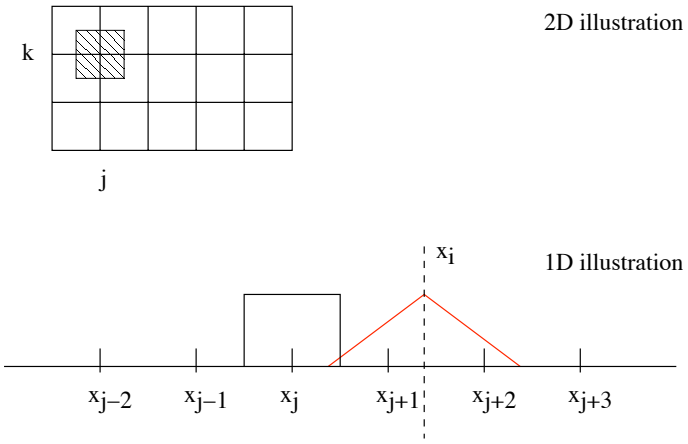

Figure 4.5: The square in the grid in upper part of the figure shows the integration domain in 2D. The overlap between a quasi-particle of triangular shape and the integration domain in 1D is shown in the lower part of the figure. The x_j's denote the grid points. The rectangle indicates the integration domain.

Dropping particle and sort labels $\vec{x}_i^{\,k} \to \vec{x}$ and $q^k \to q$ the charge distribution is given by

$$\rho_{jkl}^{n+\frac{1}{2}} = \frac{q}{Q}\,\frac{\alpha^2}{\eta}\,\frac{1}{N_c}\,\zeta_{jkl}\left(\vec{x}^{\,n+\frac{1}{2}}\right) . \tag{4.142}$$

Since the quasi-particle propagates along the x-direction we must have

$$\rho_{jkl}^{n+\frac{3}{2}} = \frac{q}{Q}\,\frac{\alpha^2}{\eta}\,\frac{1}{N_c}\,\zeta_{jkl}\left(\vec{x}^{\,n+\frac{3}{2}}\right) = \frac{q}{Q}\,\frac{\alpha^2}{\eta}\,\frac{1}{N_c}\,\zeta_{jkl}\left(\vec{x}^{\,n+\frac{1}{2}} + \delta x\,\vec{e}_x\right) , \tag{4.143}$$

resulting in

$$\begin{aligned} j_{x,j+\frac{1}{2}kl}^{n+1} &= j_{x,j-\frac{1}{2}kl}^{n+1} \\ &\quad + \frac{q\,\alpha^2}{Q\,\eta\,N_c}\,\frac{\Delta x}{\Delta t}\left[\zeta_{jkl}\left(\vec{x}^{\,n+\frac{1}{2}} + \delta x\,\vec{e}_x\right) - \zeta_{jkl}\left(\vec{x}^{\,n+\frac{1}{2}}\right)\right] , \end{aligned} \tag{4.144}$$

where

$$\begin{aligned} &\zeta_{jkl}\left(\vec{x}^{\,n+\frac{1}{2}} + \delta x\,\vec{e}_x\right) - \zeta_{jkl}\left(\vec{x}^{\,n+\frac{1}{2}}\right) \\ &\quad = \left[\zeta_{1j}\left(x^{\,n+\frac{1}{2}} + \delta x\right) - \zeta_{1j}\left(x^{\,n+\frac{1}{2}}\right)\right]\,\zeta_{2k}\left(y^{\,n+\frac{1}{2}}\right)\,\zeta_{3l}\left(z^{\,n+\frac{1}{2}}\right) . \end{aligned} \tag{4.145}$$

With the help of Eqn (4.140) the updated current can be calculated. The generalization to 3D is simple. We assume that the quasi-particle moves the distance $\delta\vec{x}$ during the time step Δt and introduce the definitions

$$j_{x,j+\frac{1}{2}kl}^{n+1} = j_{x,j-\frac{1}{2}kl}^{n+1} - \frac{\Delta x}{\Delta t}\,\frac{q}{Q}\,\frac{\alpha^2}{\eta}\,\frac{1}{N_c}\,\Delta\rho_{x,jkl}^{n+1} , \tag{4.146}$$

$$
\begin{aligned}
j^{n+1}_{y,jk+\frac{1}{2}l} &= j^{n+1}_{y,jk-\frac{1}{2}l} - \frac{\Delta y}{\Delta t}\,\frac{q}{Q}\,\frac{\alpha^2}{\eta}\,\frac{1}{N_c}\,\Delta\rho^{n+1}_{y,jkl}\;, \\
j^{n+1}_{z,jkl+\frac{1}{2}} &= j^{n+1}_{z,jkl-\frac{1}{2}} - \frac{\Delta z}{\Delta t}\,\frac{q}{Q}\,\frac{\alpha^2}{\eta}\,\frac{1}{N_c}\,\Delta\rho^{n+1}_{z,jkl}\;.
\end{aligned}
$$

This means that knowing the weights $\Delta\rho_x$, $\Delta\rho_y$, and $\Delta\rho_z$ the currents j_x, j_y, and j_z can be calculated. Equations (4.146) are recursion relations. However, since each quasi-particle can advance, at most, by one cell during the time step Δt they are easy to evaluate. To simplify the notation further grid and time labels are dropped

$$
\zeta_{jkl}\left(\vec{x}^{\,n+\frac{1}{2}}\right) \;\rightarrow\; \zeta(\vec{x})\;, \qquad \vec{\Delta\rho}^{\,n+1}_{jkl} \rightarrow \vec{\Delta\rho}\;, \qquad \vec{j}^{n+1}_{jkl} \rightarrow \vec{j}\;. \tag{4.147}
$$

Any shift of the quasi-particle can be represented by eight fractional shifts as is easily understood from the 1D example. Hence, we assume that each of the weights $\Delta\rho_x$, $\Delta\rho_y$, and $\Delta\rho_z$ can be represented by

$$
\begin{aligned}
\Delta\rho \;=\;& \alpha_1\,\zeta(x+\delta x, y+\delta y, z+\delta z) + \alpha_2\,\zeta(x+\delta x, y+\delta y, z) \\
&+\alpha_3\,\zeta(x+\delta x, y, z+\delta z) + \alpha_4\,\zeta(x, y+\delta y, z+\delta z) \\
&+\alpha_5\,\zeta(x+\delta x, y, z) + \alpha_6\,\zeta(x, y+\delta y, z) \\
&+\alpha_7\,\zeta(x, y, z+\delta z) + \alpha_8\,\zeta(x, y, z)\;,
\end{aligned} \tag{4.148}
$$

where $\Delta\rho$ is synonymous for $\Delta\rho_x$, $\Delta\rho_y$, and $\Delta\rho_z$. In order to calculate the weights $\Delta\rho_x$, $\Delta\rho_y$, and $\Delta\rho_z$ it is realized from (4.20) that

$$
\zeta\left(\vec{x}+\delta\vec{x}\right) - \zeta\left(\vec{x}\right) \;=\; \Delta\rho_x + \Delta\rho_y + \Delta\rho_z\;. \tag{4.149}
$$

Naturally it is required that $\Delta\rho_x = 0$ for $\delta x = 0$, $\Delta\rho_y = 0$ for $\delta y = 0$, and $\Delta\rho_z = 0$ for $\delta z = 0$. In addition, making use of the permutation symmetry $\zeta(x,y,z) = \zeta(y,x,z)$ it is found that for $\delta x = \delta y$ the equation $\Delta\rho_x = \Delta\rho_y$ holds. The same is true for permutations of the pairs (x,z) and (y,z). Finally, it needs to be remembered that

$$
\sum_{jkl}\zeta_{jkl}\left(\vec{x}\right) \;=\; 1\;. \tag{4.150}
$$

Due to the conservation of the quasi-particle mass we require

$$
\sum_{jkl}\Delta\rho_{xjkl} \;=\; 0\;, \qquad \sum_{jkl}\Delta\rho_{yjkl} = 0\;, \qquad \sum_{jkl}\Delta\rho_{zjkl} = 0\;. \tag{4.151}
$$

Taking all together 10 conditions for the representations of $\Delta\rho_x$, $\Delta\rho_y$, and $\Delta\rho_z$ are obtained. Each representation has 8 coefficients which can now be determined. Omitting details it is found

$$
\begin{aligned}
\Delta\rho_x \;=\;& \frac{1}{3}\,\zeta(x+\delta x, y+\delta y, z+\delta z) - \frac{1}{3}\,\zeta(x, y+\delta y, z+\delta z) \\
&+\frac{1}{6}\,\zeta(x+\delta x, y, z+\delta z) - \frac{1}{6}\,\zeta(x, y, z+\delta z) \\
&+\frac{1}{6}\,\zeta(x+\delta x, y+\delta y, z) - \frac{1}{6}\,\zeta(x, y+\delta y, z) \\
&+\frac{1}{3}\,\zeta(x+\delta x, y, z) - \frac{1}{3}\,\zeta(x, y, z)\;,
\end{aligned} \tag{4.152}
$$

$$\begin{aligned}
\Delta\rho_y &= \frac{1}{3}\,\zeta(x+\delta x, y+\delta y, z+\delta z) - \frac{1}{3}\,\zeta(x+\delta x, y, z+\delta z) \qquad (4.153)\\
&\quad +\frac{1}{6}\,\zeta(x, y+\delta y, z+\delta z) - \frac{1}{6}\,\zeta(x, y, z+\delta z)\\
&\quad +\frac{1}{6}\,\zeta(x+\delta x, y+\delta y, z) - \frac{1}{6}\,\zeta(x+\delta x, y, z)\\
&\quad +\frac{1}{3}\,\zeta(x, y+\delta y, z) - \frac{1}{3}\,\zeta(x, y, z)\ ,\\
\Delta\rho_z &= \frac{1}{3}\,\zeta(x+\delta x, y+\delta y, z+\delta z) - \frac{1}{3}\,\zeta(x+\delta x, y+\delta y, z) \qquad (4.154)\\
&\quad +\frac{1}{6}\,\zeta(x, y+\delta y, z+\delta z) - \frac{1}{6}\,\zeta(x, y+\delta y, z)\\
&\quad +\frac{1}{6}\,\zeta(x+\delta x, y, z+\delta z) - \frac{1}{6}\,\zeta(x+\delta x, y, z)\\
&\quad +\frac{1}{3}\,\zeta(x, y, z+\delta z) - \frac{1}{3}\,\zeta(x, y, z)\ .
\end{aligned}$$

Recalling that the form factors given by Eqn. (4.57) factorize the calculation of the density decomposition (4.152), (4.153), and (4.154) can be further simplified.

The currents $\vec{j}$ are computed in **PIC_move_part.f** by summing over the contribution of each individual quasi-particle. The module also computes the charge densities.

4.6 Energy conservation

The energy conservation law monitors the change of field and particle energies. Dropping species labels k we find for the change of energy with time of a particle at $\vec{x}_i$ with momentum $\vec{p}_i$

$$\begin{aligned}
\frac{d}{dt}\left(c\sqrt{mc^2+\vec{p}_i^{\,2}(t)} - mc^2\right) &= q\,\vec{v}_i(t)\cdot\vec{E}(\vec{x}_i(t),t)\ , \qquad (4.155)\\
\frac{d\vec{x}_i(t)}{dt} &= \vec{v}_i(t)\ .
\end{aligned}$$

It is assumed that collisions take place instantaniously. This means that the quasi-particles remain at rest during the binary collision processes. Hence, only kinetic energy between species k can be exchanged. The binary collision processes redistribute the quasi-particles in momentum space. After the collision processes the quasi-elements are allowed to move and to radiate. Since binary collisions are implemented in a way that conserves kinetic energy and there is no radiation during collisions we do not need to consider them here. A different way to look at the problem is to calculate the mean charge and energy densities from the Vlasov-Boltzmann equation. The calculation shows that binary collisions do not enter the balance equations as long as radiation processes are not considered during collisions.

We find the following relation for the energy density of quasi-particles k dropping the time arguments and summing over the quasi-particle index i

$$\begin{aligned}
&\frac{d}{dt}\left[\frac{n_0\,mc^2}{N_c}\,\sum_i \phi_{jkl}(\vec{x}_i)\,\left(\sqrt{1+\frac{\vec{p}_i^{\,2}}{mc^2}}-1\right)\right] \qquad (4.156)\\
&\qquad = \frac{q\,n_0}{N_c}\,\sum_i \phi_{jkl}(\vec{x}_i)\,\vec{v}_i\cdot\vec{E}(\vec{x}_i,t)\ .
\end{aligned}$$

where ϕ_{jkl} is the grid representation of the function ϕ given by Eqn. (4.57). Identifying the terms on the right hand side of Eqn. (4.156) finally yields

$$\frac{d\epsilon_{jkl}(t)}{dt} = \vec{j}_{jkl}(t) \cdot \vec{E}_{jkl}(t) \; , \tag{4.157}$$

where the energy density on the grid is given by

$$\epsilon_{jkl} \;=\; \frac{n_0\, mc^2}{N_c} \sum_i \phi_{jkl}(\vec{x}_i) \left(\sqrt{1 + \frac{\vec{p}_i^{\,2}}{mc^2}} - 1 \right) \; ,$$

or, in dimensionless units,

$$\epsilon_{jkl} \;=\; \frac{\alpha^2}{\eta^2} \frac{1}{N_c} \frac{m}{M} \sum_i \phi_{jkl}(\vec{x}_i) \left(\sqrt{1 + \vec{p}_i^{\,2}} - 1 \right) \; . \tag{4.158}$$

With the help of Maxwell's equations we find

$$\frac{\vec{E}_{jkl}^{n+1} \cdot \vec{E}_{jkl}^{n+\frac{1}{2}} - \vec{E}_{jkl}^{n+\frac{1}{2}} \cdot \vec{E}_{jkl}^{n}}{\Delta t} \;=\; \vec{E}_{jkl}^{n+\frac{1}{2}} \cdot \vec{\nabla}^{-} \times \vec{B}_{jkl}^{\,n+\frac{1}{2}} - \vec{j}_{jkl}^{\,n+\frac{1}{2}} \cdot \vec{E}_{jkl}^{n+\frac{1}{2}} \; , \tag{4.159}$$

$$\frac{\vec{B}_{jkl}^{n+1} \cdot \vec{B}_{jkl}^{n+\frac{1}{2}} - \vec{B}_{jkl}^{n+\frac{1}{2}} \cdot \vec{B}_{jkl}^{n}}{\Delta t} \;=\; -\vec{B}_{jkl}^{n+\frac{1}{2}} \cdot \vec{\nabla}^{+} \times \vec{E}_{jkl}^{\,n+\frac{1}{2}} \; , \tag{4.160}$$

$$\frac{\epsilon_{jkl}^{n+1} - \epsilon_{jkl}^{n}}{\Delta t} \;=\; \vec{j}_{jkl}^{\,n+\frac{1}{2}} \cdot \vec{E}_{jkl}^{n+\frac{1}{2}} \; . \tag{4.161}$$

Taking all terms together we obtain

$$\begin{aligned} &\frac{\vec{E}_{jkl}^{n+1} \cdot \vec{E}_{jkl}^{n+\frac{1}{2}} + \vec{B}_{jkl}^{n+1} \cdot \vec{B}_{jkl}^{n+\frac{1}{2}}}{\Delta t} - \frac{\vec{E}_{jkl}^{n+\frac{1}{2}} \cdot \vec{E}_{jkl}^{n} + \vec{B}_{jkl}^{n+\frac{1}{2}} \cdot \vec{B}_{jkl}^{n}}{\Delta t} \\ &= \vec{E}_{jkl}^{n+\frac{1}{2}} \cdot \vec{\nabla}^{-} \times \vec{B}_{jkl}^{\,n+\frac{1}{2}} - \vec{B}_{jkl}^{n+\frac{1}{2}} \cdot \vec{\nabla}^{+} \times \vec{E}_{jkl}^{\,n+\frac{1}{2}} \\ &\quad - \frac{\epsilon_{jkl}^{n+1} - \epsilon_{jkl}^{n}}{\Delta t} \; . \end{aligned} \tag{4.162}$$

The routine **OUT_poyc.f** checks Eqn. (4.162).

Chapter 5

The simulation code PSC

The PSC code is a three-dimensional (3D) Cartesian collisional kinetic code based on the Monte-Carlo-Particle-In-Cell (MCPIC) method. The code solves the relativistic Vlasov-Boltzmann equations coupled to the Maxwell equations for an arbitrary number of species. The code runs on distributed computing platforms. It features a 3D domain decomposition. The code structure is simple to understand so that modifications, corrections and extensions are easy to perform. The code is modular. Most of the modules in the code can be run stand alone. Hence, it is possible to solve the Vlasov equations only. This holds for the Maxwell solver and collision module too. The PSC code has a load distributer and is capable of checkpointing its core at any predefined time. The code can be restarted from the core dump. The code uses the Message Passing Interface MPI which is the message passing standard available on most workstation clusters and parallel supercomputers with distributed memory up to a few thousand compute nodes. The source code language is FORTRAN90. The graphics packages shipped with the PSC code use the IDL language from RSI.

5.1 Details of the code

The PSC consists of different modules that model physics, control the code, and allow graphical processing of the data output. In the following sections we explain what the different modules do and how they are related to each other.

5.1.1 Name conventions for important fields

The following name conventions for the fields in the PSC are made:

- ex, ey, ez: electric fields in x-, y-, and z-directions.
- bx, by, bz: magnetic fields in x-, y-, and z-directions.
- jxi, jyi, jzi: total current densities in x-, y-, and z-directions.
- nn, ne, ni: charge densities for atoms, electrons, and ions.
- p_niloc: quasi-particle array for all particles.

The fields reserved for writing data out are:

- ext, eyt, ezt: electric fields in x-, y-, and z-directions.

- ex2t, ey2t, ez2t: squared electric fields in x-, y-, and z-directions.
- bxt, byt, bzt: magnetic fields in x-, y-, and z-directions.
- bx2t, by2t, bz2t: squared magnetic fields in x-, y-, and z-directions.
- jxit, jyit, jzit: total current densities in x-, y-, and z-directions.
- jxexit, jyeyit, jzezit: total energy deposition in x-, y-, and z-directions.
- nnt, net, nit: charge densities for atoms, electrons, and ions.
- poyxt, poyyt, poyzt: poynting fluxes in x-, y-, and z-directions.

5.1.2 The modules of the PSC

The PSC consists of the main programs **VLI.f**, **VLA.f**, and **SELECT.f**. The initialization module is **VLI.f**. The program starts the simulation. After a predefined time it writes the simulation core to the disk, which can be read by the main program **VLA.f**. The module **SELECT.f** post-processes the simulation data generated by **VLI.f** and **VLA.f**. The programs **VLI.f**, **VLA.f**, and **SELECT.f** call several subroutines that are listed below. A makefile with the name **Makefile** is provided to compile the code.

VLI.f: This is the code that starts the simulations. It calls the following routines:

- **INIT_param.f**: Sets the parameters that control the operation of the PSC code and define part of the plasma properties that are modeled. The parameters to be set are:
  - cpum: wall clock time limit
  - lw: laser wavelength
  - i0: laser intensity
  - n0: background density
  - lengthx: simulation box length in x-direction
  - lengthy: simulation box length in y-direction
  - lengthz: simulation box length in z-direction
  - xnpe: number of computation domains in x-direction
  - ynpe: number of computation domains in y-direction
  - znpe: number of computation domains in z-direction
  - i1tot: total number of grid points along the x-axis
  - i2tot: total number of grid points along the y-axis
  - i3tot: total number of grid points along the z-axis
  - i1n,i1x: end points of the grid in x-direction,requirement $i1x - i1n < i1tot$
  - i2n,i2x: end points of the grid in y-direction,requirement $i2x - i2n < i2tot$
  - i3n,i3x: end points of the grid in z-direction,requirement $i3x - i3n < i3tot$
  - boundary_field_x: selects the boundary conditions for the fields in x
  - boundary_field_y: selects the boundary conditions for the fields in y
  - boundary_field_z: selects the boundary conditions for the fields in z

  - boundary_part_x: selects the boundary conditions for the particles in x
  - boundary_part_y: selects the boundary conditions for the particles in y
  - boundary_part_z: selects the boundary conditions for the particles in z
  - nmax: time step limit
  - nprf: first time step for the output of field data
  - dnprf: time step increment for the output of field data
  - nprc: first time step for the output of collision data
  - dnprc: time step increment for the output of collision data
  - nprparti: first time step for particle data output
  - dnprparti: time step increment for particle data output
  - nistep: particle number increment for particle data output
  - pario: number of simultaneous I/O operations
  - dataout: path for data files
  - datachk: path for check-pointing files
  - tmnvf: time step when the time averaging of fields starts
  - tmxvf: time step when the time averaging of fields ends
  - tmnvp: time step when the time averaging of energy flux starts
  - tmxvp: time step when the time averaging of energy flux ends

- **INIT_idistr.f**: Sets the initial positions and momenta of the particles and their properties. Calculates the best initial load distribution on parallel computing platforms. Set up can be complex. The subroutine **INIT_den.f** is used to set the particle positions. Details can be obtained in section 4.3.1. The following parameters need to be set:

  - Mlim: upper limit for the available memory per node
  - dvel: speed at which the local computing domain is adapted
  - deval: particle subset used for load calculation
  - nicell: number of particles per cell
  - qni: particle charge
  - mni: particle mass
  - cni: cell the particle is in
  - lni: particle number
  - wni: particle weight
  - tni: temperature

  - **INIT_den.f**: Initial density function. Can be re-programmed freely. The following parameters need to be set:
    * x0: location of density center in x-direction
    * y0: location of density center in y-direction
    * z0: location of density center in z-direction
    * Lx: density gradient length in x-direction

  - Ly: density gradient length in y-direction
  - Lz: density gradient length in z-direction
  - widthx: width of density profile in x-direction
  - widthy: width of density profile in y-direction
  - widthz: width of density profile in z-direction

- **INIT_field.f**: Sets the initial values of most fields used in the PSC code. Also used to set up a laser pulse inside the simulation box. The following routines are called:
  - **INIT_spulse_z1.f** and **INIT_ppulse_z1.f**: Define the boundaries for a s- or p-polarized laser pulse propagating in positive z-direction at any location. The routines can be re-programmed. The following parameters need to be set:
    - dxm: pulse length x-direction
    - dym: pulse length y-direction
    - dzm: pulse length z-direction
    - xm: pulse center x-direction
    - ym: pulse center y-direction
    - zm: pulse center z-direction
  - **PIC_fax.f**, **PIC_fay.f**, and **PIC_faz.f**: Required for observables calculated from distributed particle data. The routines makes use of the MPI library.

- **OUT_param.f**: Generates a protocol of simulation parameters for the run. The data are recorded in the file **VLA.data**.

- **PIC_sort.f**: Generates a random sequence of particles and sorts them into cells in consecutive order according to their randomized labels. The routine is required if binary collisions are carried out.

- **PIC_bin_coll.f**: Performs binary collisions following the MCPIC method as described in section 4.4. The routine has to be adapted for the particle distribution set up in **INIT_idistr.f**. The following parameters need to be set:
  - lnL: Coulomb logarithm
  - npmax: number of particles of a particular sort allowed in cell
  - spxnsp: number of all particle sorts allowed in a cell

- **PIC_msa.f**: Maxwell solver following the FDTD scheme as described in section 4.2. The routine propagates the fields by half a time step to integral values and sets the boundary conditions for the Maxwell fields. The following routines are called:
  - **INIT_spulse_x1.f**, **INIT_spulse_x2.f**, **INIT_spulse_y1.f**, **INIT_spulse_y2.f**, **INIT_spulse_z1.f**, and **INIT_spulse_z2.f**, **INIT_ppulse_x1.f**, **INIT_ppulse_x2.f**, **INIT_ppulse_y1.f**, **INIT_ppulse_y2.f**, **INIT_ppulse_z1.f**, and **INIT_ppulse_z2.f**: Define the boundaries for s- or p-polarized laser pulse propagation in x, y, and z-directions depending on the name of the routines at any location. The routines can be re-programmed. The parameters to be set are:
    - dxm: pulse length x-direction
    - dym: pulse length y-direction

    - dzm: pulse length z-direction
    - xm: pulse center x-direction
    - ym: pulse center y-direction
    - zm: pulse center z-direction
  - **PIC_fex.f**, **PIC_fey.f**, and **PIC_fez.f**: Exchange distributed field data and set boundary conditions for the fields.

- **OUT_field.f**: Writes the field data out. The post-processors are used to read the recorded data and to generate compressed data files for the IDL scripts.
- **PIC_msb.f**: Propagates the Maxwell fields by half a time step. The following routines are called:
  - **PIC_fex.f**, **PIC_fey.f**, and **PIC_fez.f**
- **OUT_part.f**: Writes the particle data out. The post-processor is used to read the recorded data and to generated compressed data files for the IDL scripts.
- **PIC_move_part.f**: Propagates particles and calculates the current densities required for the Maxwell solver as described in section 4.5. Also calculates charge densities from distributed particle data. The following routines are called:
  - **PIC_fax.f**, **PIC_fay.f**, and **PIC_faz.f**
  - **PIC_pex.f**, **PIC_pex.f**, and **PIC_pex.f**: Exchange distributed particle data and set boundary conditions for the particles.
- **OUT_poyc.f**: Calculates the field energy, energy currents, and energy deposition by the Maxwell fields and particles.
- **SERV_write.f**: Check-points the data core of the simulation. The data core is required to restart the simulation at a later time.

VLA.f: This is the production code. It calls the following routines:

- **INIT_param.f**
- **OUT_param.f**
- **SERV_read.f**: Reads check-pointed data to re-start the simulation.
- **PIC_sort.f**
- **PIC_bin_coll.f**
- **PIC_msa.f**
- **OUT_field.f**
- **PIC_msb.f**
- **OUT_part.f**
- **PIC_move_part.f**
- **OUT_poyc.f**

- **SERV_write.f**

SELECT.f: This is the program for data post-processing. It calls the following routines:

- **SELECT_pfield_evol.f**: Selects the time resolved field data.
- **SELECT_tfield_evol.f**: Selects the time averaged field data.
- **SELECT_cl_evol.f**: Monitors the degree of energy conservation.
- **SELECT_electron_evol.f**: Selects the electron data.
- **SELECT_ion_evol.f**: Selects the ion data.
- **SELECT_atom_evol.f**: Selects the atom data.

5.1.3 Time progression in the PSC

The routine **INIT_field.f** initializes the fields. The routine **PIC_msa.f** advances the fields $\vec{E}^{\,n}$ and $\vec{B}^{\,n}$ with the help of the current $\vec{j}^{\,n}$ by half a time step to $\vec{E}^{\,n+\frac{1}{2}}$ and $\vec{B}^{\,n+\frac{1}{2}}$. With the help of **PIC_move_part.f** and the fields $\vec{E}^{\,n+\frac{1}{2}}$ and $\vec{B}^{\,n+\frac{1}{2}}$ the particle positions and momenta $\vec{x}^{\,n}$ and $\vec{p}^{\,n}$ are advanced to $\vec{x}^{\,n+1}$ and $\vec{p}^{\,n+1}$. The current $\vec{j}^{\,n+1}$ is calculated. With the help of **PIC_msb.f** and $\vec{j}^{\,n+1}$ the fields $\vec{E}^{\,n+\frac{1}{2}}$ and $\vec{B}^{\,n+\frac{1}{2}}$ are advanced to $\vec{E}^{\,n+1}$ and $\vec{B}^{\,n+1}$. Figure 5.1 shows the flow diagram. The new fields are used in a new time cycle as is indicated by the arrows in the figure.

5.1.4 TCSH scripts for data processing

While **SELECT.x** can be used to select single data sets the TCSH scripts described here are helpful to generate large numbers of compressed data files for further processing with the supplied IDL scripts. The TCSH scripts call **SELECT.x**. They do not need further adaption. The supplied TCSH scripts are:

- **PROCESSOR_pfield**: Time-resolved field data post-processor.
- **PROCESSOR_tfield**: Time-averaged field data post-processor.
- **PROCESSOR_electron**: Electron data post-processor.
- **PROCESSOR_ion**: Ion data post-processor.
- **PROCESSOR_atom**: Atom data post-processor.

5.1.5 IDL scripts

There are a number of IDL scripts supplied with the code for automatic data post-processing. The IDL scripts need the compressed data files that are generated from the raw simulation data with the help of the TCSH scripts **PROCESSOR_pfield** to **PROCESSOR_atom** described earlier. The IDL scripts implement further diagnostics. They have adjustable parameters that define, which particular data sets are read from the disk and that control the layout of the plots they generate. The IDL scripts produce unique file names for the identification of the processed data sets. The names of the scripts themselves are useful to identify what they do. The letters **read** stand for scripts that read simulation data. The letters **fields** stand for field data. Adjustable parameters control the name of the data sets

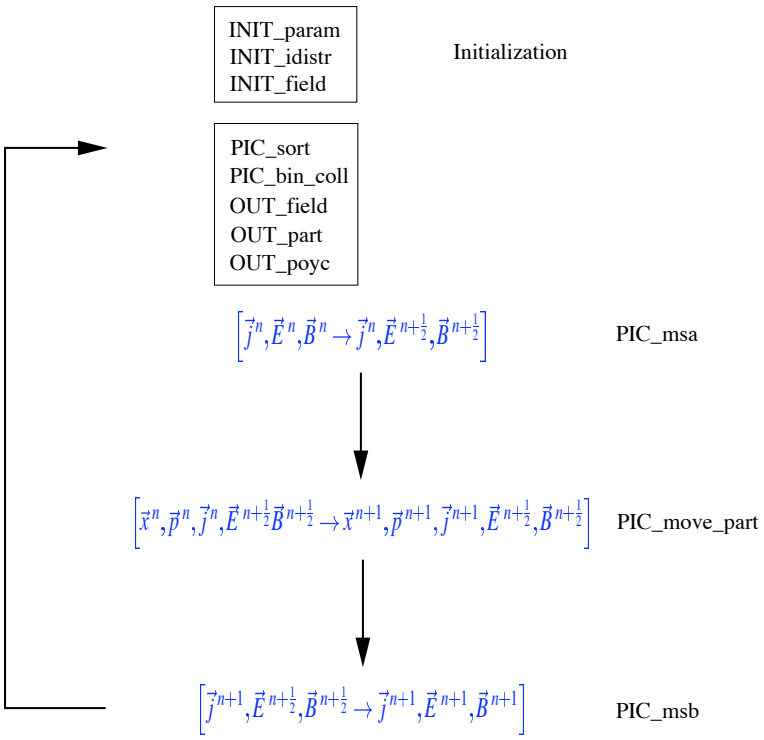

Figure 5.1: The figure lists the modules called by **VLI.f** and illustrates the time flow. The diagram for **VLA.f** is similar. The arrows indicate the direction of time progression. Further details are given in the text.

and the range of the field values that is plotted. The data range is controlled with the help of the parameters **mini** and **maxi**. The letters **parts** stand for particle data. Adjustable parameters control the names of the particle data sets that are evaluated, the volume of phase space that is plotted, the charge of the particles in units of the electron charge, and their mass in units of the electron mass. The phase space volume is controlled with the help of **x1** to **z2**, **pxmin** to **pzmax**, **enmin** to **enmax**. The letters **ps** in the file name of the plots mean that the output format is postscript. The letters **xy** indicate that the plots will show the xy-projection of phase space. The remaining 2D projections have synonymous abbreviations. The letters **mass** indicate that the particle mass is discriminated while the letters **charge** mean the same for the particle charge. The combination of **mass** and **charge** discriminates the particle data for both their mass and charge. The postscript plots, which the supplied IDL scripts produce, print further information at the top left corner of the plots that helps to uniquely identify the processed data sets. The postscript plots can be converted into a number of other data formats. The supplied scripts are:

- **read_FIELDS_1D.pro**: This is an IDL script that generates 1D plots of field data. The program calls the following routines:
  - **fields_ps.pro**

- **read_FIELDS_2D.pro**: This is an IDL script that generates 2D plots of field data. The program calls the following routines:
  - **fields_xy_ps.pro**
  - **fields_xz_ps.pro**
  - **fields_yz_ps.pro**
- **read_FIELDS_3D.pro**: This is an IDL script that generates 3D plots of field data. The program calls the following routine:
  - **fields_xyz_ps.pro**
- **read_ELECTRONS.pro**, **read_IONS.pro**, and **read_ATOMS.pro**: These are IDL scripts that generates 2D plots of particle data. The programs calls the following routines:
  - **parts_xy_ps.pro**
  - **parts_charge_xy_ps.pro**
  - **parts_mass_xy_ps.pro**
  - **parts_mass_charge_xy_ps.pro**
  - **parts_xz_ps.pro**
  - **parts_charge_xz_ps.pro**
  - **parts_mass_xz_ps.pro**
  - **parts_mass_charge_xz_ps.pro**
  - **parts_yz_ps.pro**
  - **parts_charge_yz_ps.pro**
  - **parts_mass_yz_ps.pro**
  - **parts_mass_charge_yz_ps.pro**
  - **parts_xpxpypz_ps.pro**
  - **parts_mass_charge_xpxpypz_ps.pro**
  - **parts_ypxpypz_ps.pro**
  - **parts_mass_charge_ypxpypz_ps.pro**
  - **parts_zpxpypz_ps.pro**
  - **parts_mass_charge_zpxpypz_ps.pro**
  - **parts_enz_ps.pro**
  - **parts_pxpypz_ps.pro**
  - **parts_charge_pxpypz_ps.pro**
  - **parts_mass_pxpypz_ps.pro**
  - **parts_mass_charge_pxpypz_ps.pro**

5.1.6 PBS batch scripts

The letters PBS stand for Portable Batch System. The PBS has a set of commands that can be used to control the execution of jobs. The following PBS batch scripts are provided to submit the simulation code, the TCSH scripts for data formatting and compression, and the IDL scripts to the batch queues of a computer system running OpenPBS:

- **vliexec**: Submits **VLI.x** to the batch queues. The scripts performs different functions. If parallel I/O is required it links distributed data sets to the home directory. The script generates backup files.
- **vlaexec**: Submits **VLA.x** to the batch queues. The scripts performs different functions. If parallel I/O is required it links distributed data sets to the home directory. The script generates backup files.
- **pexec**: Submits **PROCESSOR_pfield** to the batch queues.
- **texec**: Submits **PROCESSOR_tfield** to the batch queues.
- **eexec**: Submits **PROCESSOR_electron** to the batch queues.
- **iexec**: Submits **PROCESSOR_ion** to the batch queues.
- **aexec**: Submits **PROCESSOR_atom** to the batch queues.
- **IDLFIELD1D**: Submits **IDL**-scripts to the batch queues.
- **IDLFIELD2D**: Submits **IDL**-scripts to the batch queues.
- **IDLFIELD3D**: Submits **IDL**-scripts to the batch queues.
- **IDLELECTRON**: Submits **IDL**-scripts to the batch queues.
- **IDLION**: Submits **IDL**-scripts to the batch queues.
- **IDLATOM**: Submits **IDL**-scripts to the batch queues.

5.2 Required hardware and software

The PSC has been developed for computing platforms with many processors and distributed memory. However, it is also possible to run the code on servers with a single processor. Successful implementations of the PSC have also been established on servers with multiple processors and shared memory. The PSC requires the installation of a FORTRAN90 compiler and the MPI library. For graphical output use of the IDL language is made.

5.2.1 Server hardware

Several low cost server configurations have been built and tested with the code. A list of tested server configurations is given below. The fastest configurations are listed at the top:

	CPU	CLOCK	BOARD	RAM	OP	COMPILER
S1	Dual AMD 64bit	2.2 GHz	MSI 9131 PCI − X	4 GB	FEDORA CORE3	pgf90 64bit
S2	AMD 64bit	2.2 GHz	MSI 9131 PCI − X	2 GB	FEDORA CORE3	pgf90 64bit
S3	AMD 64bit	2.2 GHz	ASUS SK8V PCI	2 GB	FEDORA CORE3	pgf90 64bit
S4	INTEL 32bit P4	3.2 GHz	INTEL P4 Tyan PCI − X	2 GB	FEDORA CORE3	pgf90 32bit
S5	INTEL 32bit P4	3.2 GHz	ASUS P4C800 PCI	2 GB	FEDORA CORE3	pgf90 32bit

Each server can be interconnected with any number of servers to form a compute cluster with many compute nodes. Support for how to build and configure a computing cluster for

the PSC, the most recent server configurations and of how to implement the PSC on them, and information about low cost high performance interconnects can be obtained from the Open Source Project web-site *http://www.THE-PSC.com*.

5.2.2 Operating system

There are several choices for the operating system. One that has achieved great attention in recent years due to its low costs and high performance is the LINUX operating system. Linux is available free of charge from installation servers or as a supported distribution from various vendors like SUSE. The SUSE distribution can be obtained at *http://www.novell.com/linux/suse*. Depending on the server hardware 32-bit and 64-bit versions of the LINUX operating system are available. The tested server configurations have been supplied with LINUX Fedora Core 3. The ISO-images can be downloaded at *http://fedora.redhat.com/download*. Fedora Core 3 proved to be stable on all listed server configurations.

5.2.3 Fortran compilers

The Portland FORTRAN compilers are used. They generate fast and stable code. The compilers can be obtained at *http://www.pgroup.com*.

5.2.4 Message passing software

The PSC needs the MPI message passing software. The MPI package can be obtained at *http://www-unix.mcs.anl.gov/mpi/mpich*.

5.2.5 Graphics software

At present the IDL software is used for data evaluation. The IDL package can be obtained at *http://www.rsinc.com*.

5.2.6 The batch system

To operate the PSC in single processor or multi-processor mode the OpenPBS batch system is used. It can be obtained at *http://www.openpbs.org*. Further support to adapt it to operate on a cluster computer can be obtained at *http://www.THE-PSC.com*.

Chapter 6

Examples

In this section we review a few problems from the field of laser-plasma physics and show how the PSC can be used for modeling. For each example we perform simulations with the PSC and provide the source code for the runs. The target platform used for all simulations described here is a Beowulf cluster based on INTEL Pentium IV processors with 3.2GHz clock speed and 2GB RAM per node. The operating system is Redhat Linux with Kernel Version 2.4.18. The MPICH library version 1.2.4 has been installed on the servers. The FORTRAN compiler used is the Portland Group compiler pgf90. The graphics software used is IDL-5.6 from RSI.

The basic interest in intense laser pulse propagation through plasma is the wide range of potential applications. These include electron acceleration by wake-fields as is investigated in [15, 45, 46, 47, 102, 88], relativistic optical laser pulse guiding, x-ray lasing, and high-harmonic generation [90, 91, 92]. Recent experimental evidence of relativistic laser pulse channeling in under-dense plasma has been given by [93, 88, 94]. Measurable signals from the interaction of intense laser pulses with under-dense plasma have been discussed in [95, 96]. The onset of relativistic self-focusing in ionizing high density gas jets has been observed by [97]. Instabilities arising due to intense laser pulse propagation through under-dense plasma are analyzed in [37, 98, 99, 100, 101]. Numerical simulations of wake-field generation, beam filamentation, particle acceleration, and trapping are presented in [100, 36, 102, 103, 104, 105]. Detailed analytical accounts of nonlinear phenomena of intense laser pulses in under-dense plasma are found in [90, 106, 107, 108, 109, 110, 111]. In particular, self-generated magnetic fields in under-dense plasma are discussed in [48, 112, 113]. Aspects of laser pulse propagation in magnetized plasma are treated in [114, 115]. Recent reviews of nonlinear laser optics including instabilities and ionizational effects are given by [100, 101]. High-harmonic generation is reviewed by [92]. A review on magnetic field generation is found in [96]. Absorption of laser radiation in plasma and transport of mass and energy are important issues for potential applications like the Fast Ignition concept in Inertial Confinement Fusion (ICF) [26, 116]. As soon as the radiation pressure of the laser exceeds the thermal pressure of the plasma and the interaction time of the laser with the plasma is sufficiently long processes like shock formation [9], density profile steepening, hole boring [33, 50, 93, 94], and target surface corrugation [51] take place. At the same time fast electrons are generated [58, 88, 110, 117] with transport properties related to the target geometry.

It is the aim of this section to discuss theoretical aspects of intense laser pulse propagation through plasma with particular attention to nonlinear plasma optics, self-generated electric and magnetic fields, laser pulse absorption, and the acceleration of ions. The discussion of plasma and beam instabilities is omitted. Readers interested in the latter are referred

to the recent review articles [100, 101]. In section 6.1 the par-axial approximation of the relativistic wave equation for a laser beam is derived and analyzed. Envelope equations for the slowly varying amplitude are given. In section 6.2 special attention is devoted to self-generated electric and magnetic fields. In section 6.3 some analytical considerations of laser pulse absorption are given. They are not supported by simulations. Here we refer the interested reader to the literature [9].

6.1 Basics of nonlinear plasma optics

Most analytical treatments done for intense laser pulses in under-dense plasma assume that it can be described by a cold ideal-fluid model. Although this means a considerable simplification compared to a kinetic approach the corresponding set of coupled equations has still a high degree of complexity which is difficult to keep track of. A powerful approach to an understanding of the nonlinear phenomena involved is obtained by deriving envelope equations of low dimensionality for the laser beam and fluid motion. These equations are expected to describe the slow time scale evolution on large spatial scales of the laser-plasma interaction correctly. In the following a brief derivation of the par-axial approximation of the relativistic wave equation for the cold fluid will be given and then the latter will be used to derive envelope equations [100, 101, 108]. In particular the derivation follows [100, 108]. The starting point are Maxwell's equations in the Lorentz gauge

$$\partial_j\partial_j A_i - \frac{1}{c^2}\partial_t^2 A_i = -\frac{1}{\epsilon_0 c^2} j_i \,, \tag{6.1}$$

$$\partial_j\partial_j \Phi - \frac{1}{c^2}\partial_t^2 \Phi = -\frac{1}{\epsilon_0}\rho \,, \tag{6.2}$$

with the gauge condition

$$\partial_i A_i + \frac{1}{c^2}\partial_t \Phi = 0 \,,$$

and the relativistic cold fluid equations

$$\begin{aligned} \left(\partial_t + v_j\partial_j\right)\left(p_i - eA_i\right) &= e\left(\partial_i\Phi - v_j\partial_i A_j\right) \,, \\ \partial_t n + \partial_i\left(n v_i\right) &= 0 \,, \end{aligned} \tag{6.3}$$

with

$$\begin{aligned} \rho &= e\left(n_0 - n\right) \,, \qquad j_i = -env_i \,, \\ v_i &= \frac{p_i}{m\gamma} \,, \qquad \gamma = \sqrt{1 + \frac{p_j p_j}{m^2 c^2}} \,. \end{aligned} \tag{6.4}$$

The quantities A_i and Φ denote the components of the vector potential and the scalar potential, respectively. In the first equation of (6.3) the relation

$$\left[\mathbf{v}\times\nabla\times\mathbf{A}\right]_i = v_j\partial_i A_j - v_j\partial_j A_i \tag{6.5}$$

has been used. Summation over repeated indices is implied. All other quantities in Equations (6.1), (6.3) and (6.4) denote electron properties. They will now be solved for small densities ($n \ll n_c$) by a multiple scale expansion. The multiple scale expansion method makes the

assumption that the envelope of the high frequency laser pulse oscillations varies slowly transverse to the beam propagation direction and even slower along it provided that a frame of reference co-moving with the group velocity v_g of the laser pulse is adopted. To find an appropriate ordering parameter of spatial scales Equations (6.1), (6.3), and (6.4) are normalized to

$$\begin{aligned} &p_i \to \frac{p_i}{mc} \,, \qquad A_i \to \frac{eA_i}{mc} \,, \qquad \Phi \to \frac{e\Phi_i}{mc^2} \,, \\ &t \to \omega t \,, \qquad r_i \to \frac{\omega r_i}{c} \,, \qquad n \to \frac{n}{n_0} \,. \end{aligned} \tag{6.6}$$

The quantity n_0 denotes the background ion density which is assumed to be constant. The laser frequency is denoted by ω. The electron mass is given by m. It is found

$$\begin{aligned} \partial_j\partial_j A_i - \partial_t^2 A_i &= \epsilon^2 j_i \,, \\ \partial_j\partial_j \Phi - \partial_t^2 \Phi &= \epsilon^2 (n-1) \,, \\ \partial_i A_i + \partial_t \Phi &= 0 \quad , \end{aligned} \tag{6.7}$$

and

$$\begin{aligned} \left(\partial_t + v_j\partial_j\right)\left(p_i - A_i\right) &= \partial_i\Phi - v_j\partial_i A_j \,, \\ \partial_t n + \partial_i\left(n v_i\right) &= 0 \,, \end{aligned} \tag{6.8}$$

with

$$v_i = \frac{p_i}{\gamma} \,, \qquad \gamma = \sqrt{1 + p_j p_j} \,, \qquad \epsilon = \frac{\omega_p}{\omega} \,, \qquad \omega_p = \sqrt{\frac{e^2 n_0}{\epsilon_0 m}} \,. \tag{6.9}$$

Following [108], now the ansatz

$$\begin{aligned} f(\mathbf{r},t) &= f_0(\epsilon x, \epsilon y, \epsilon^2 z, \xi) + \epsilon f_1(\epsilon x, \epsilon y, \epsilon^2 z, \xi) \,, \\ \xi &= z - \alpha t \,, \qquad \alpha = \frac{v_g}{c} \end{aligned} \tag{6.10}$$

is made for all physical quantities in Equations (6.7) and (6.8). The subscript 0 will be omitted in the following. Ansatz (6.10) implies

$$\begin{aligned} &\partial_x \to \epsilon\partial_x \,, \\ &\partial_y \to \epsilon\partial_y \,, \\ &\partial_z \to \partial_\xi + \epsilon^2\partial_z \,, \\ &\partial_t \to -\alpha\partial_\xi \,, \\ &\partial_i\partial_i - \partial_t^2 \to \epsilon^2\left(\partial_x^2 + \partial_y^2\right) + (1-\alpha^2)\partial_\xi^2 + 2\epsilon^2\partial_z\partial_\xi + \epsilon^4\partial_z^2 \,. \end{aligned} \tag{6.11}$$

Applying Equations (6.11) to Equations (6.7) and (6.8) and retaining only the lowest order in ϵ yields

$$\begin{aligned} \left(\partial_x^2 + \partial_y^2 + 2\partial_\xi\partial_z - \frac{\alpha^2-1}{\epsilon^2}\partial_\xi^2\right) A_i &= n v_i \,, \\ \left(\partial_x^2 + \partial_y^2 + 2\partial_\xi\partial_z - \frac{\alpha^2-1}{\epsilon^2}\partial_\xi^2\right) \Phi &= n - 1 \,, \\ \partial_\xi(A_z - \alpha\,\Phi) &= 0 \,, \end{aligned} \tag{6.12}$$

for Maxwell equations, and

$$\begin{aligned}\partial_\xi(nv_z - n) &= 0\,, \\ \partial_\xi(p_x - A_x) &= 0\,, \\ \partial_\xi(p_y - A_y) &= 0\,, \\ (v_z - 1)\partial_\xi(p_z - A_z) &= \partial_\xi\Phi - v_j\partial_\xi A_j\end{aligned} \tag{6.13}$$

for the fluid equations. The quantity $\alpha^2 - 1$ is of the same order as ϵ^2 which will be justified a posteriori. Equations (6.13) have a simple solution for circularly polarized laser light. Due to the second and third equations of (6.13) it may be assumed that

$$A_x = p_x\,, \qquad A_y = p_y\,. \tag{6.14}$$

Next cylindrical geometry is adopted and the ansatz

$$\begin{aligned}\mathbf{A}_\perp &= \frac{1}{\sqrt{2}}\left[(\mathbf{e}_x + i\mathbf{e}_y)\; A(\rho,z)\; \exp\left(i\frac{\xi}{\alpha}\right) + c.c.\right]\,, \\ \mathbf{v}_\perp &= \frac{1}{\sqrt{2}}\left[(\mathbf{e}_x + i\mathbf{e}_y)\; v(\rho,z)\; \exp\left(i\frac{\xi}{\alpha}\right) + c.c.\right]\,.\end{aligned} \tag{6.15}$$

is made. In addition, it is assumed that $A_z = 0$ holds which means that plasma wave generation is neglected. The amplitude $A(\rho, z)$ describes the slowly varying envelope of the laser beam. From the last equation of (6.12) it is found that $\alpha\partial_\xi\Phi = \partial_\xi A_z = 0$. With the help of these relations and the ansatz according to (6.15) it is found that from the last equation of (6.13), $\partial_\xi p_z = 0$, and consequently, from the first equation of (6.13) $\partial_\xi n = 0$. Hence, $p_z = 0$ is assumed. In order to establish the missing relation between the density n and the field amplitudes A_x and A_y, Equations (6.3) are expanded up to first order in ϵ. This yields

$$\begin{aligned}&(v_x\partial_x + v_y\partial_y)\,(p_x - A_x) - \alpha\partial_\xi\,(p_{x1} - A_{x1}) \\ &\qquad = \partial_x\Phi - v_x\partial_x A_x - v_y\partial_x A_y\,, \\ &(v_x\partial_x + v_y\partial_y)\,(p_y - A_y) - \alpha\partial_\xi\,(p_{y1} - A_{y1}) \\ &\qquad = \partial_y\Phi - v_x\partial_x A_x - v_y\partial_x A_y\,, \\ &\partial_\xi\Phi = -v_x\partial_\xi A_{x1} - v_y\partial_\xi A_{y1} - v_{x1}\partial_\xi A_x - v_{y1}\partial_\xi A_y\,.\end{aligned} \tag{6.16}$$

Time averaging (integration over the time variable ξ) over a full cycle finally gives

$$\partial_x\Phi = \partial_x\sqrt{1 + AA^*}\,, \qquad \partial_y\Phi = \partial_y\sqrt{1 + AA^*}\,. \tag{6.17}$$

With the help of Equations (6.15) and noting that $\partial_\xi\Phi = 0$ holds, it is finally obtained from Equations (6.12)

$$\left(\Delta_\perp + 2\frac{i}{\alpha}\partial_z\right)A \;=\; \left(\frac{n}{\gamma} - \frac{\alpha^2 - 1}{\epsilon^2\alpha^2}\right)A\,, \qquad n = 1 + \Delta_\perp\gamma\,, \tag{6.18}$$

where $\gamma = \sqrt{1 + AA^*}$. The dispersion relation obtainable from (6.18) gives relativistic corrections to the relation $\omega^2 = \omega_p^2 + c^2k^2$. Neglecting the relativistic corrections, it is found that $\alpha^2 - 1 = \alpha^2\epsilon^2$ showing that $\alpha^2 - 1$ is indeed of the order ϵ^2. In dimensional form, under the assumption that $\omega_p \ll \omega$, the relations $k = \omega/c$ and $v_g = c$ are found which yields

$$(\Delta_\perp + 2ik\partial_z)\,A \;=\; k^2\,\left(1 - \eta^2\right)A\,, \tag{6.19}$$

where

$$\eta^2 = 1 - \frac{\omega_p^2}{\omega^2} \frac{1}{\sqrt{1+\left|\frac{eA}{mc}\right|^2}} \left[1 + \frac{c^2}{\omega_p^2}\Delta_\perp \sqrt{1+\left|\frac{eA}{mc}\right|^2}\right] \tag{6.20}$$

denotes the refractive index.

Equation (6.19) is a par-axial approximation for the relativistic wave equation. It describes the propagation of the envelope of a long, slowly varying laser pulse. Limiting assumptions on spatial scales and laser pulse polarization have been made. It has also been assumed that a cold fluid description of the plasma is adequate. Hence, the par-axial wave equation (6.19) is only valid for long, circularly polarized laser pulses in a very dilute cold plasma for which $L \gg 2\pi c/\omega_p$ holds, where the quantity L denotes the pulse length in space. In addition, Equation (6.19) neglects plasma wave generation. Nevertheless, it is a highly nonlinear wave equation with far reaching implications [101]. In deriving (6.19) a constant background density was assumed. However, it will be shown in section 6.2 that this restriction may be relaxed with the consequence that ω_p in (6.19) becomes space dependent. It is now proceeded by expanding the refractive index given in Equation (6.20) for small density variations and small intensities while laser frequency variations are neglected [101]. It is found for the refractive index η

$$\eta \approx 1 - \frac{\omega_p^2}{2\omega^2}\left[1 + \frac{\delta n}{n_0} - \frac{1}{2}\left(1 - \frac{c^2}{\omega_p^2}\,\Delta_\perp\right)\left|\frac{eA}{mc}\right|^2\right] . \tag{6.21}$$

Neglecting ponderomotive density perturbations ($\Delta_\perp = 0$) and assuming parabolic radial density variation it may be written

$$\eta = \eta_0 - \eta_1 \frac{\rho^2}{\rho_0^2} + \eta_2 I , \tag{6.22}$$

where

$$\eta_0 = 1 - \frac{\omega_p^2}{2\omega^2} , \tag{6.23}$$

$$\eta_1 = \frac{\omega_p^2}{4\omega^2}\,\frac{\rho_0^2}{n_0}\,\partial_\rho^2 n(0) , \tag{6.24}$$

$$\eta_2 = \frac{\omega_p^2}{4\omega^2}\,\frac{e^2}{\epsilon_0 m^2\omega^2 c^3} . \tag{6.25}$$

Here n_0 denotes the unperturbed plasma density, $I = \epsilon_0 c\omega^2 A_0^2/2$ the laser intensity and A_0 the field strength. In order to derive envelope equations for Equation (6.19) the ansatz

$$A(\rho, z) = \frac{A_0\rho_0}{\rho_s(z)}\,\exp\left(-\left[1 - i\alpha_s(z)\right]\frac{\rho^2}{\rho_s^2(z)} + i\theta_s(z)\right) \tag{6.26}$$

is made [100], where ρ_s denotes the laser beam diameter, α_s the curvature of the wave front and θ_s the inverse wavelength shift. The wave front curvature α_s accounts for the larger phase velocities at the radial edges of the laser beam as soon as self-focusing starts. In addition, self-focusing changes the wave number and diameter of the beam which is described by θ_s and ρ_s. The ansatz (6.26) conserves total laser power. Hence, the quantity ρ_0 may be determined from the total laser beam power P by $\rho_0 = \sqrt{P/\pi A_0^2}$. A detailed discussion

given in [100] shows that the ansatz (6.26) can be improved by the source dependent expansion technique (SDE). However, in the present context the latter improves accuracy but contributes no new qualitative features. In the following, the laser intensity dependent part of the refractive index in Equation (6.21) is treated to lowest order as a parameter. It is obtained in polar coordinates

$$\begin{aligned}\frac{1}{\rho}\partial_\rho\left[\rho\partial_\rho A(\rho,z)\right] &= A(\rho,z)\left[-\frac{4}{\rho_s^2(z)}\left[1-i\alpha_s(z)\right]\right. \\ &\quad \left.+\frac{4\rho^2}{\rho_s^4(z)}\left[1-i\alpha_s(z)\right]^2\right], \\ 2ik\partial_z A(\rho,z) &= A(\rho,z)\left[-\frac{2ik}{\rho_s(z)}\partial_z\rho_s(z)\right. \\ &\quad +4ik\left[1-i\alpha_s(z)\right]\frac{\rho^2}{\rho_s^3(z)}\partial_z\rho_s(z) \\ &\quad \left.-2k\frac{\rho^2}{\rho_s^2(z)}\partial_z\alpha_s(z)-2k\partial_z\theta_s(z)\right].\end{aligned} \tag{6.27}$$

Under the assumption

$$I(\rho,z) = I_0\exp\left(-\frac{2\rho^2}{\rho_s^2(z)}\right)\approx I_0\left(1-\frac{2\rho^2}{\rho_s^2(z)}\right) \tag{6.28}$$

it is found, up to first order in $\rho^2/\rho_s^2(z)$, for the right hand side of Equation (6.19)

$$\begin{aligned}k^2\left(1-\eta^2\right)A(\rho,z) = k^2A(\rho,z)\Bigg(&\cdot 1-(\eta_0+\eta_2I_0)^2 \\ &+\left[4\eta_2(\eta_0+\eta_2I_0)I_0+2\eta_1(\eta_0+\eta_2I_0)\frac{\rho_s^2(z)}{\rho_0^2}\right]\frac{\rho^2}{\rho_s^2(z)}\Bigg).\end{aligned} \tag{6.29}$$

Next equal orders of $\rho^2/\rho_s^2(z)$ from the left and right hand sides of Equation (6.19) are compared using Equations (6.27) and (6.29). The zeroth order in $\rho^2/\rho_s^2(z)$ yields

$$\begin{aligned}-\frac{4}{\rho_s^2(z)}\left[1-i\alpha_s(z)\right]-\frac{2ik}{\rho_s(z)}\partial_z\rho_s(z)-2k\,\partial_z\theta_s(z) \\ = k^2\left(1-(\eta_0+\eta_2I_0)^2\right).\end{aligned} \tag{6.30}$$

Comparison of real and imaginary parts of Equation (6.30) yields envelope equations for the wave front curvature $\alpha_s(z)$ and the wave number shift $\theta_s(z)$

$$\begin{aligned}\alpha_s(z) &= \frac{k\rho_s^2(z)}{2}\,\partial_z\rho_s(z), \\ \partial_z\theta_s(z) &= -\frac{2}{k\rho_s^2(z)}-\frac{k}{2}\left[1-(\eta_0+\eta_2I_0)^2\right].\end{aligned} \tag{6.31}$$

Finally, to obtain the envelope for the laser beam diameter, the first order of $\rho^2/\rho_s^2(z)$ from the left and right of Equation (6.19) is compared making use of Equations (6.27) and (6.29). With the help of the Equations (6.31) we find

$$\partial_z^2\rho_s(z) = \frac{4}{k^2\rho_s^3(z)}\left[1-\frac{1}{2}\eta_0\eta_1k^2\frac{\rho_s^4(z)}{\rho_0^2}-\eta_0\eta_2I_0k^2\rho_s^2(z)\right]. \tag{6.32}$$

Introducing the definitions [100]

$$P = \frac{1}{2}\pi\rho_0^2 I_0 \,, \qquad P_c = \frac{\pi}{2k^2\eta_0\eta_2} \,, \qquad \eta_c = \frac{2}{k^2\rho_0^2\eta_0} \,, \tag{6.33}$$
$$Z_r = \frac{k\rho_0^2}{2} \,, \qquad R(z) = \frac{\rho_s(z)}{\rho_0} \,,$$

yields

$$\partial_z^2 R(z) = \frac{1}{Z_r^2 R^3(z)} \left[1 - \frac{\eta_1}{\eta_c} R^4(z) - \frac{P}{P_c}\right] . \tag{6.34}$$

The quantity P_c is the critical laser power and Z_r the Rayleigh length. The first term on the right of Equation (6.34) describes diffraction. It tends to increase the laser beam diameter while the last term has a compensating effect. In case of $P = P_c$ it exactly balances the diffractive force of the laser beam. Neglecting density modulations in the refractive index ($\eta_1 = 0$), it is obtained from Equation (6.34)

$$R(z) = \sqrt{1 + \left(1 - \frac{P}{P_c}\right)\frac{z^2}{Z_r^2}} \,. \tag{6.35}$$

A similar self-focusing effect may be obtained if a density channel is produced with radially increasing density. In that case it is found $\partial_\rho^2 n(0) > 0$. Hence, the ratio η_1/η_c is positive. It is seen as well that ionization may lead to enhanced diffraction since then $\eta_1/\eta_c < 0$ may hold [111]. The critical laser power obtained from Equations (6.33) is $P_c = 4.057 \cdot 10^9$ W (ω^2/ω_p^2). A detailed analysis of Equations (6.19) and (6.20) including ponderomotive self-channeling yields $P_c \approx 16.2 \cdot 10^9$ W (ω^2/ω_p^2) [36, 100].

6.1.1 Simulations of laser propagation in vacuum

In this subsection we present simulations of laser beam propagation in vacuum with the PSC in 3D. The theoretical background of vacuum laser beam propagation has been explained in section 6.1. The theory shows that a laser beam diffracts over a length scale, which is the Rayleigh length. Since we consider the problem of laser beam propagation in vacuum, the collision module **PIC_bin_coll.f** and the particle mover **PIC_move_part.f** have been turned off in **VLI.f** and **VLA.f**.

We begin by describing the setup of the simulation. Figure 6.1 depicts the simulation box, which we have selected for the simulation. A Cartesian right-handed coordinate system has been attached to the box, the origin of which is denoted by $(0, 0, 0)$. The same coordinate system is used in the PSC. The size of the simulation box is set up in **INIT_param.f**. We select a 3D simulation box of $20\,\mu\text{m} \times 20\,\mu\text{m} \times 50\,\mu\text{m}$. This is done by setting $lengthx = 20\,\mu$m, $lengthy = 20\,\mu$m, and $lengthz = 50\,\mu$m. The number of grid points for the spatial grid is $200 \times 200 \times 500$. The grid size is established by setting $i1tot = 200$, $i2tot = 200$, and $i3tot = 500$. We assign $200 \times 200 \times 500$ cells to the grid by setting $i1n = 0$, $i1x = 199$, $i2n = 0$, $i2x = 199$, $i3n = 0$, and $i3x = 499$. The plasma density required for normalization in the PSC (see subsection 4.1) is determined by $n0$. We set $n0 = 10^{25}\,\text{m}^{-3}$. The electric field strength $e0$ (see subsection 4.1) is obtained with the help of the laser intensity $i0$. We choose $i0 = 2 \cdot 10^{22}\,\text{Wm}^{-2}$. The laser frequency wl is determined with the help of the laser wavelength lw. We take $lw = 10^{-6}\,$m. We select periodic boundaries for the Maxwell fields and the quasi-particles along the x- and y-directions. However, we choose radiating boundary conditions for the fields and reflecting boundaries for the particles at $z = 0$ and

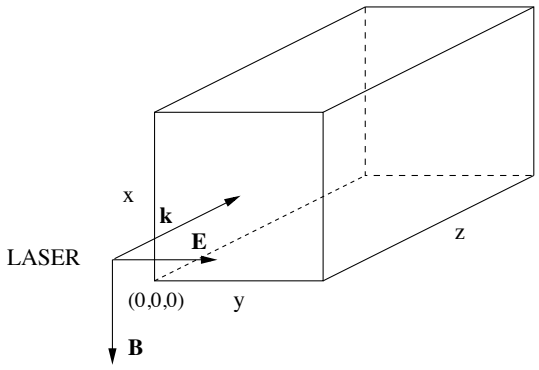

Figure 6.1: Laser beam propagation in vacuum in 3D. The figure shows the simulation box. The box defines a coordinate system, the origin of which is at $(0, 0, 0)$. The direction of the incident laser pulse is along the z-axis. It is indicated by $\vec{k}$ at the front side of the box. The laser field polarization is also depicted by arrows.

$z = 50\,\mu$m. We place no laser pulse at $z = 50\,\mu$m. Under these conditions radiation from inside the simulation box can freely escape at $z = 50\,\mu$m. The boundary conditions are set up by selecting $boundary\_field\_x = 1$, $boundary\_field\_y = 1$, $boundary\_field\_z = 0$, $boundary\_part\_x = 1$, $boundary\_part\_y = 1$, and $bounday\_part\_z = 0$. Since the simulation is very small we choose to carry it out on four nodes. We select $xnpe = 2$, $ynpe = 2$, and $znpe = 1$. The filesystems selected for the data output and check-pointing of the data are the ones from which the simulation is started. This means $data\_out =$ "./" and $data\_chk =$ "./". The maximum permissible CPU time for the simulation for a single run is set with the help of the parameter $cpum$. We choose $cpum = 6000$, which means 6000 sec. After 6000 sec the PSC check-points its data core and restarts the simulation from the latter. The maximum permissible number of time steps is given by $nmax$. We select $nmax = 1000$. The parameters for data output control have been adjusted such that output is generated every four full laser cycles, which means after $np = 4\,nnp$ time steps, where nnp is the number of time steps for a full laser cycle, for the time resolved fields. We do not need particles in the simulation. We remove particles from the simulation either by setting $INIT\_den = 0$ in **INIT_den.f** or by setting $nicell = 0$ in **INIT_idistr.f**. Time-averaging is repeatedly done over a full laser cycle. The required settings are $tmnvf = 1$, $tmxvf = nnp$, $tmnvp = 1$, and $tmxvp = nnp$. The initial location, direction, and polarization of the laser pulse is set with the help of twelve files. Details are listed in subsection 5.1. The laser pulse is assumed to propagate along the z-axis and to be p-polarized, which means that the electric field vector of the laser oscillates along the y-axis as depicted in Fig. 6.1. Hence, we turn off all antennas except **INIT_ppulse_z1.f**, which irradiates the plasma through the surface at $z = 0$ along z. The coordinate frame used to set up the laser pulse is the same as the one used for the simulation box. The origin is at $(0, 0, 0)$. We choose a flat top laser pulse, that rises over $1\,\mu$m at full-width-half-maximum (FWHM) in propagation direction. The widths in lateral directions are $2.5\,\mu$m. At startup time of the simulation the laser pulse is placed at $(10\,\mu\text{m}, 10\,\mu\text{m}, -2\,\mu\text{m})$, which is the center of the xy-plane $2\,\mu$m in front of the simulation box. The corresponding setup parameters are $xm = 10^{-5}$ m, $ym = 10^{-5}$ m, and $zm = -2 \cdot 10^{-6}$ m. The laser pulse widths are $dxm = 2.5 \cdot 10^{-6}$ m, $dym = 2.5 \cdot 10^{-6}$ m, and $dzm = 10^{-6}$ m. In case **OpenPBS** is available (see subsection 5.1.6) the scripts **vliexec** to

IDLATOM have to be adjusted to the local computing environment. It is further necessary to adjust the IDL files shipped with the PSC as described in subsection 5.1.5. The post processors **PROCESSOR_pfield** to **PROCESSOR_atom** require no adaption.

We continue by describing the simulation results. During runtime the PSC records diagnostic data in the file **VLA.data**, that can be used to trace possible runtime errors. The file reflects most setup parameters and the wall clock time needed for each time-step. The file shows that $2 \cdot 10^7$ cells have been allocated for the simulation. The required memory is about 1000 MByte per node. The run takes about 18 sec of wall clock time for the computations and about 8 sec for data communication between nodes per time step. Figure 6.2 shows a 3D plot of the transverse electric field E_y^2 at $t = 133$ fs. The units are given in the figure. As has been predicted by the theoretical considerations in section 6.1 we find that the laser beam diffracts. The diffraction length is the Rayleigh length $Z_r \approx 18\,\mu$m for the parameters of the simulation. Since it is difficult the illustrate laser beam diffraction in a 3D plot, we are showing an iso-contour plot of E_y^2 at $x = 10\,\mu$m in plot (a) of Fig. 6.3. Plot (b) of the same figure shows a 1D line-out of the field amplitude through the center of the diffracting beam. We note that the $FDTD$-scheme shows numerical dispersion, which starts to become a problem at the resolution taken for this simulation. Details are found in the literature.

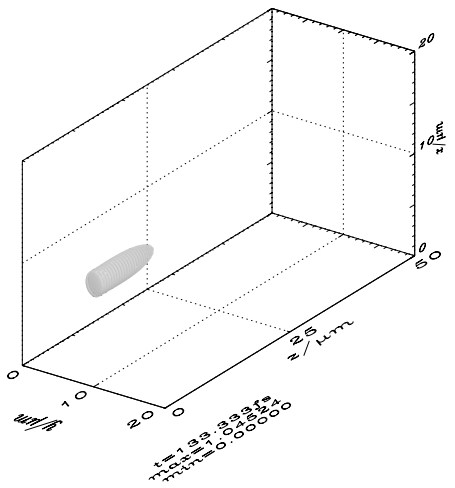

Figure 6.2: Laser beam propagation in vacuum in 3D. The figure shows the field E_y^2 after $t = 133$ fs. The units of the field are $E_0 = 8.67 \cdot 10^{12}$ V/m. The contour level plotted is $0.5 \cdot E_0^2$.

6.1.2 Simulations of relativistic self-focusing in 2D

In this subsection we present simulations of self-focusing with the PSC in 2D. The theoretical background of self-focusing has been laid out in section 6.1. The theory presented is valid for weakly relativistic intensities ($a = v_{os}/c > 1$) and does not contain kinetic effects, which we will briefly address here too. The plasma we consider here consists of electrons and protons. It is irradiated by a laser beam at relativistic intensity, which means ($a \gg 1$). The peak

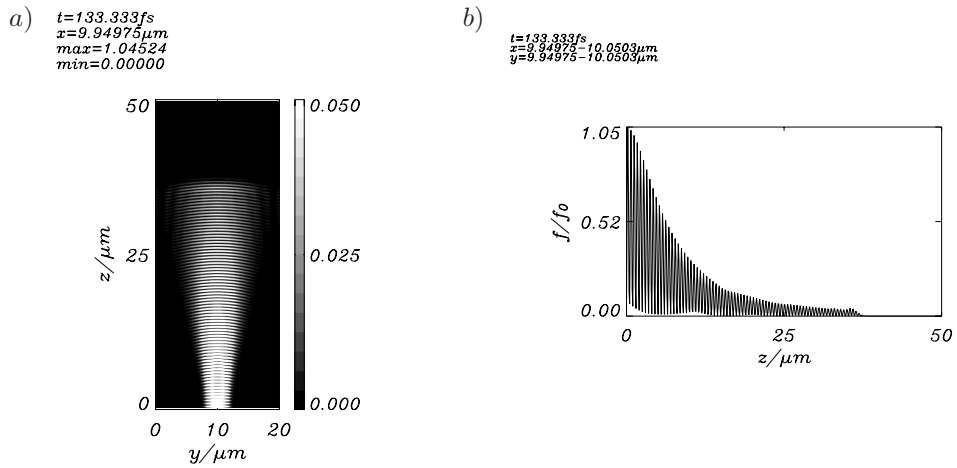

Figure 6.3: Laser beam diffraction in vacuum. The setup of the 3D simulation is depicted in Fig. 6.1, while the laser beam in 3D is shown in Fig. 6.2. The figure shows the 2D contour plot of the field E_y^2 at $t = 133\,\mathrm{fs}$ (a) and the field amplitude of the latter along the z-axis at $x = y = 10\,\mu\mathrm{m}$ (b). The color-bar in plot (a) gives the data range selected for the plot, while the maximum and minimum values of the field E_y^2 are printed at the top left corner of the plot. The units of the field are $E_0 = 8.67 \cdot 10^{12}\,\mathrm{V/m}$.

plasma density is sub-critical (see section 6.1). This means that $\omega > \omega_{pe}$ holds. Since the plasma density for a sub-critical plasma is low and the proton charge can only be $Z = 1$ we neglect collisions. Hence, the collision module **PIC_bin_coll.f** has been turned off in **VLI.f** and **VLA.f**.

We begin by describing the setup of the simulation. Figure 6.4 depicts the simulation box, which we have selected for the simulation. A Cartesian right-handed coordinate system has been attached to the box, the origin of which is denoted by $(0, 0, 0)$. The same coordinate system is used in the PSC. The simulation box is 3D. However, we only select the 2D simulation plane depicted by the shaded area in the figure, which is placed in the center of 3D simulation box. The sector shaded in dark represents the plasma. The size of the simulation box is set up in **INIT_param.f**. We select a 3D simulation box of $40\,\mu\mathrm{m} \times 40\,\mu\mathrm{m} \times 50\,\mu\mathrm{m}$. This is done by setting $lengthx = 40\,\mu\mathrm{m}$, $lengthy = 40\,\mu\mathrm{m}$, and $lengthz = 50\,\mu\mathrm{m}$. The number of grid points of the spatial grid is $400 \times 400 \times 1000$. The grid size is established by setting $i1tot = 400$, $i2tot = 400$, and $i3tot = 1000$. For the 2D plane in Fig. 6.4, however, only 400×1000 cells are considered by assigning $i1n = 199$, $i1x = 199$, $i2n = 0$, $i2x = 399$, $i3n = 0$, and $i3x = 999$. The plasma density required for normalization in the PSC (see subsection 4.1) is determined by $n0$. We set $n0 = 10^{26}\,\mathrm{m}^{-3}$. The electric field strength $e0$ (see subsection 4.1) is obtained with the help of the laser intensity $i0$. We choose $i0 = 10^{23}\,\mathrm{Wm}^{-2}$. The laser frequency wl is determined with the help of the laser wavelength lw. We take $lw = 10^{-6}\,\mathrm{m}$. We select periodic boundaries for the Maxwell fields and the quasi-particles along the x- and y-directions. However, we choose radiating boundary conditions for the fields and periodic boundary conditions for the particles at $z = 0$ and $z = 50\,\mu\mathrm{m}$. We place no laser pulse at $z = 50\,\mu\mathrm{m}$. Under these conditions radiation from inside the simulation box can freely escape $z = 50\,\mu\mathrm{m}$. The boundary conditions are set up by selecting $boundary\_field\_x = 1$, $boundary\_field\_y = 1$, $boundary\_field\_z = 0$,

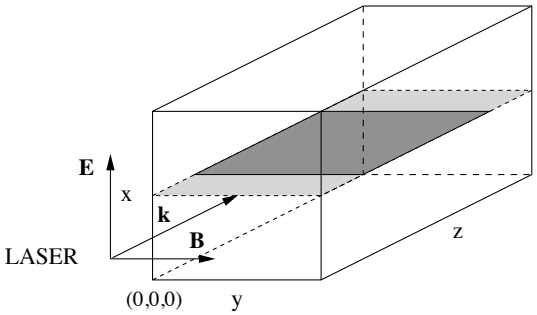

Figure 6.4: Relativistic self-focusing. The figure shows the simulation box that harbors the 2D simulation plane used in the PSC for the run. The plasma is indicated by the darker area inside the simulation plane. The box defines a coordinate system, the origin of which is at $(0, 0, 0)$. The direction of the incident laser pulse is along the z-axis. It is indicated by $\vec{k}$ at the front side of the box. The laser field polarization is depicted by $\vec{E}$. Since the electric field is perpendicular to the simulation plane the laser pulse is called s-polarized.

boundary_part_x $= 1$, *boundary_part_y* $= 1$, and *bounday_part_z* $= 1$. Since the simulation is very small we choose to carry it out on a single node. This implies $xnpe = 1$, $ynpe = 1$, and $znpe = 1$. The filesystems selected for the data output and check-pointing of data core are the ones from which the simulation is started. This means *data_out* = "./" and *data_chk* = "./". The maximum permissible CPU time for the simulation for a single run is set with the help of the parameter *cpum*. We choose $cpum = 6000$, which means 6000 sec. After 6000 sec the PSC check-points its data core and restarts the simulation from the latter. The maximum permissible number of time steps is given by $nmax$. We select $nmax = 2000$. The parameters for data output control have been adjusted such that output is generated every four full laser cycles, which means after $np = 4\,nnp$ time steps, where nnp is the number of time steps for a full laser cycle, for the time resolved fields and particles. Every particle is recorded after np time steps. The relevant settings are $nprf = 0$, $dnprf = np$, $nprc = 0$, $dnprc = np$, $nprparti = 0$, $dnprparti = np$, $nistep = 1$. Time-averaging is repeatedly done over a full laser cycle. The required settings are $tmnvf = 1$, $tmxvf = nnp$, $tmnvp = 1$, and $tmxvp = nnp$. While $n0$ sets the density for the normalization in the PSC, the file **INIT_den.f** is required to determine the shape and location of the plasma in the simulation box. The coordinate system used for setting up the density is the same as the one that defines the simulation box. The origin of the coordinate system is again $(0, 0, 0)$. The default density function provided with the PSC makes use of nine parameters. They are explained in subsection 5.1. For the simulation of relativistic self-focusing we choose $x0 = 2 \cdot 10^{-5}$ m, $y0 = 2 \cdot 10^{-5}$ m, and $z0 = 2.5 \cdot 10^{-5}$ m. For the gradient lengths at the plasma boundaries we use $Lx = 10^{-8}$ m, $Ly = 10^{-8}$ m, and $Lz = 5 \cdot 10^{-8}$ m. The width of the plasma is given by $widthx = 10^{-4}$ m, $widthy = 10^{-4}$ m, and $widthz = 2 \cdot 10^{-5}$ m. The initial location, direction, and polarization of the laser beam is set with the help of twelve files. Details are listed in section 5.1. The laser beam is assumed to propagate along the z-axis and to be s-polarized, which means that the electric field vector of the laser oscillates out of the simulation plane depicted in Fig. 6.4. Hence, we turn off all antennas except **INIT_spulse_z1.f**, which irradiates the plasma through the surface at $z = 0$ along

z. The coordinate frame used to set up the laser beam is the same as the one used for the simulation box. The origin is at $(0, 0, 0)$. We choose a flat top laser beam, that rises over $1\,\mu$m at full-width-half-maximum (FWHM) in propagation direction. The widths in lateral directions are $5\,\mu$m. At startup time of the simulation the laser beam is placed at $(20\,\mu\text{m}, 20\,\mu\text{m}, -2\,\mu\text{m})$, which is the center of the xy-plane $2\,\mu$m in front of the simulation box. This means $xm = 2 \cdot 10^{-5}\,\text{m}$, $ym = 2 \cdot 10^{-5}\,\text{m}$, and $zm = -2 \cdot 10^{-6}\,\text{m}$. The laser beam widths are $dxm = 5 \cdot 10^{-6}\,\text{m}$, $dym = 5 \cdot 10^{-6}\,\text{m}$, and $dzm = 10^{-6}\,\text{m}$, where dzm characterizes the steepness of the front side of the laser beam. Next we need to set up the distribution functions. This is done with the help of the file **INIT_idistr.f**. We choose to perform the simulation for electrons and protons. We take two particles per cell for each particle sort. This means that we set $nicell = 2$. Since we deal with electrons and protons we have two entries for particle properties, one for electrons and one for protons. For the electron charge we choose $q_e = -1.6 \cdot 10^{-19}\,\text{As}$, for the electrons mass $m_e = 9.1 \cdot 10^{-31}\,\text{kg}$, and for the electron temperature $T_e = 0\,\text{keV}$. This means $qni = -1.0$, $mni = 1.0$, and $tni = 0.0$. For the protons we set $qni = 1.0$, $mni = 1836$, and $tni = 0.0$. We place the quasi-particles on mesh points in the xy-plane, while we put them at equidistant locations along the z-direction. In case **OpenPBS** is available (see subsection 5.1.6) the scripts **vliexec** to **IDLATOM** have to be adjusted to the local computing environment. It is further necessary to adjust the IDL files shipped with the PSC as described in subsection 5.1.5. The post processors **PROCESSOR_pfield** to **PROCESSOR_atom** require no adaption.

We continue by describing the simulation results. During runtime the PSC records diagnostic data in the file **VLA.data**, which can be used to trace possible runtime errors. The file reflects most setup parameters and the wall clock time needed for each time-step. The file shows that 400000 cells and $1.28 \cdot 10^6$ quasi-particles have been allocated for the simulation. The required memory is about 520 MByte. The run takes about 16 sec of wall clock time per time step on a single node. Figures 6.5 and 6.6 show plots of the transverse electric field E_x^2 at various times. The units are given in the figure. The critical laser power for the parameters of the simulation is $\approx 10^{11}$ W, while the irradiated laser power is about 10^{13} W. Consequently relativistic self-focusing of the laser beam sets in as has been predicted in section 6.1. This means that the normalized value of the transverse field E_x^2 grows with time as Fig. 6.5 shows. As the laser field grows electrons are captured in the electric potential, which the laser beam generates at its tip as it propagates through the plasma. This phenomenon is illustrated in Figs. 6.7 and 6.8. The captured electrons gain considerable energy. Plots (a) and (b) of Figs. 6.9 and 6.10 show the phase space properties of the captured electrons. As plot (b) of the figure depicts a broad electron spectrum is generated with electrons energies of up to 25 MeV. We note that the physics of electrons capture is a highly nonlinear process that has not been covered in section 6.1.

6.2 Wakefields in plasma

Self-generated electric and magnetic fields are due to nonlinear processes appearing in high orders of a typical expansion parameter. Keeping the restriction to a cold electron fluid with immobile ions, it is possible to reformulate the basic equations as a single equation in the normalized fluid momentum [48, 113], thus allowing a refined expansion technique up to high orders [48, 112, 113]. The starting point are Maxwell equations coupled with ideal cold fluid equations

$$\nabla \times \mathbf{E} = -\partial_t \mathbf{B}\,, \tag{6.36}$$

$$c^2\,\nabla \times \mathbf{B} = \partial_t \mathbf{E} + \frac{1}{\epsilon_0}\mathbf{j}\,, \tag{6.37}$$

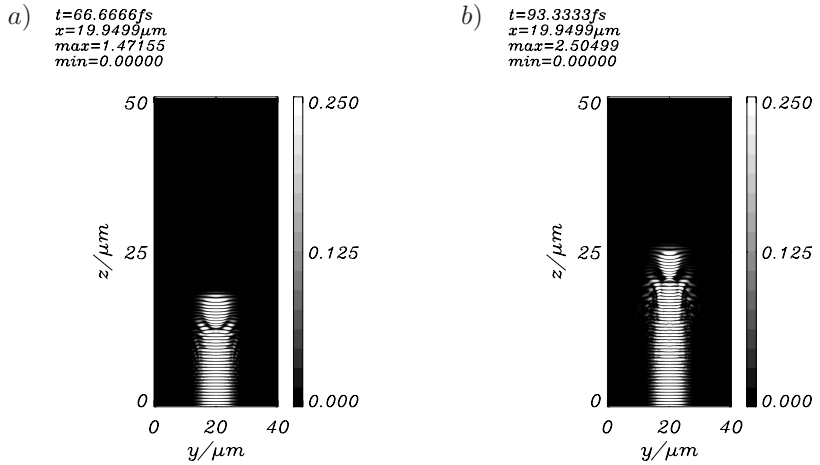

Figure 6.5: Self-focusing simulation in 2D. The laser intensity rises as the laser beam focuses. The simulation plane is the one depicted in Fig. 6.4. The laser is s-polarized and propagates along the z-axis. The figure shows the field E_x^2 at $t = 66\,\mathrm{fs}$ (a) and $t = 93\,\mathrm{fs}$ (b). The color-bars to the right show the selected data range for the plots, while the maximum and minimum values encountered by the field are printed at the top of each plot. The units of the field are $E_0 = 8.67 \cdot 10^{12}\,\mathrm{V/m}$.

$$\nabla \cdot \mathbf{E} = \frac{1}{\epsilon_0}\rho \,, \tag{6.38}$$

$$\nabla \cdot \mathbf{B} = 0 \,, \tag{6.39}$$

$$\partial_t \mathbf{p} + \mathbf{v} \cdot \nabla \mathbf{p} = -e\left(\mathbf{E} + \mathbf{v} \times \mathbf{B}\right) \,, \tag{6.40}$$

$$\partial_t n + \nabla\left(n\mathbf{v}\right) = 0 \,, \tag{6.41}$$

$$\mathbf{v} = \frac{c\mathbf{p}}{\sqrt{m^2c^2 + p^2}} \,. \tag{6.42}$$

The ions are taken to be immobile. Taking the curl of both sides of Equation (6.40) and using the relation (6.5) it is found

$$\partial_t \mathbf{\Omega} \;=\; \nabla \times \left(\mathbf{v} \times \mathbf{\Omega}\right) \,, \qquad \mathbf{\Omega} = \nabla \times \mathbf{q} - \frac{e}{mc}\mathbf{B} \,, \qquad \mathbf{q} = \frac{\mathbf{p}}{mc} \,, \tag{6.43}$$

where $\mathbf{\Omega}$ is the generalized vorticity. The implication of Equation (6.43) is that the flux of $\mathbf{\Omega}$ through an arbitrary surface moving with the fluid velocity is constant in time. This means $\partial_t \mathbf{\Omega} = 0$ (see [85, 86]). As a consequence it is obtained

$$\mathbf{B} \;=\; \frac{mc}{e}\,\nabla \times \mathbf{q} \,. \tag{6.44}$$

Equation (6.44) may now be inserted into Equation (6.40). Making use of relation (6.5) again yields

$$\mathbf{E} \;=\; -\frac{mc}{e}\,\left(\partial_t \mathbf{q} + c\nabla\sqrt{1+q^2}\right) \,. \tag{6.45}$$

The second term on the right of Equation (6.45) is the electric field induced by the ponderomotive force. Equations (6.44) and (6.45) imply $\mathbf{q} = e\mathbf{A}/mc$ and $e\Phi/mc^2 = \sqrt{1+q^2}$. With

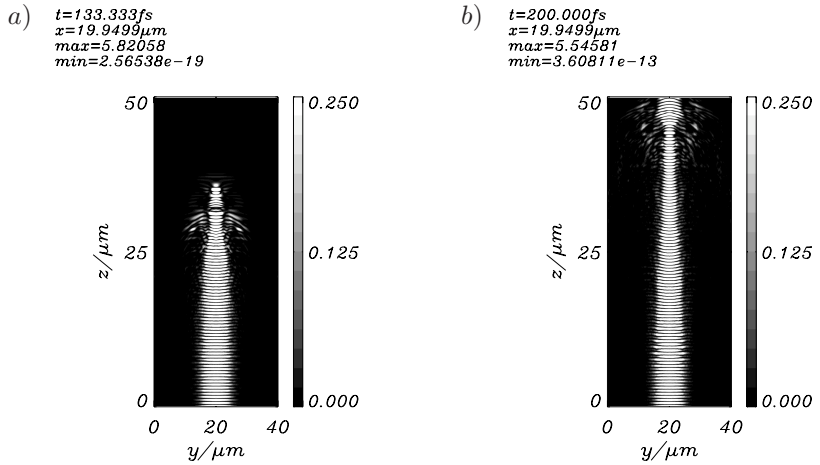

Figure 6.6: Self-focusing simulation in 2D. The laser intensity rises as the laser beam focuses. The simulation plane is the one depicted in Fig. 6.4. The laser is s-polarized and propagates along the z-axis. The figure shows the field E_x^2 at $t = 133\,\mathrm{fs}$ (a) and $t = 200\,\mathrm{fs}$ (b). The color-bars to the right show the selected data range for the plots, while the maximum and minimum values encountered by the field are printed at the top of each plot. The units of the field are $E_0 = 8.67 \cdot 10^{12}\,\mathrm{V/m}$.

the help of Equations (6.38) and (6.45) an expression for the electron density is obtained

$$\frac{n}{n_0} \;=\; 1 + \frac{c}{\omega_p^2}\,\nabla\cdot\left[\partial_t \mathbf{q} + c\nabla\sqrt{1+q^2}\right]\,, \tag{6.46}$$

where n_0 denotes the background ion density and $\omega_p = \sqrt{e^2 n_0/\epsilon_0 m}$ is the plasma frequency. Using Equations (6.37), (6.44), (6.45) and (6.46) it is found

$$\begin{aligned}\partial_t^2\mathbf{q} + c^2\nabla\times\nabla\times\mathbf{q} + \frac{\omega_p^2\mathbf{q}}{\sqrt{1+q^2}} \\ = -c\,\partial_t\nabla\sqrt{1+q^2} - c\,\frac{\mathbf{q}}{\sqrt{1+q^2}}\nabla\cdot\left[\partial_t\mathbf{q} + c\,\nabla\sqrt{1+q^2}\right]\,,\end{aligned} \tag{6.47}$$

where ω_p may depend on space. For the investigation of weak nonlinearities, Equation (6.47) is expanded up to fourth order in the normalized quiver velocity $v_{os}/c = eA/mc$. Hence, it is written for the normalized fluid momentum $\mathbf{q} = \mathbf{q}_1 + \mathbf{q}_2 + \mathbf{q}_3 + \mathbf{q}_4$, where indices denote expansion order. Making use of the approximations $\left(1+q^2\right)^{1/2} \approx 1 + q^2/2 - q^4/4$ and $\left(1+q^2\right)^{-1/2} \approx 1 - q^2/2 + 3q^4/4$ it is found

$$\begin{aligned}\partial_t^2\mathbf{q} + c^2\nabla\times\nabla\times\mathbf{q} + \omega_p^2\mathbf{q} \;=\; & -\frac{c}{2}\partial_t\nabla\left(q^2 - \frac{q^4}{2}\right) \\ & -c\,\mathbf{q}\left(1 - \frac{q^2}{2}\right)\nabla\cdot\partial_t\mathbf{q} \\ & +\frac{1}{2}\mathbf{q}\left(\omega_p^2 - c^2\Delta\right)q^2\,.\end{aligned} \tag{6.48}$$

To first order in v_{os}/c it is obtained

$$\partial_t^2\mathbf{q}_1 + c^2\nabla\times\nabla\times\mathbf{q}_1 + \omega_p^2\mathbf{q}_1 \;=\; 0\,. \tag{6.49}$$

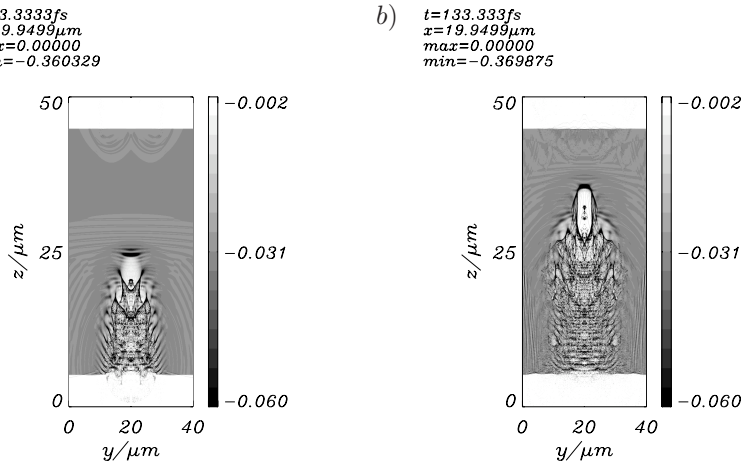

Figure 6.7: Electron capture in a self-focusing laser beam in 2D. The simulation plane is the one depicted in Fig. 6.4. The laser is s-polarized and propagates along the z-axis. The figure shows the field ρ_e at $t = 93\,\mathrm{fs}$ (a) and $t = 133\,\mathrm{fs}$ (b) The color-bars to the right show the selected data range for the plots, while the maximum and minimum values of the field are printed at the top of each plot. The units of the fields are $\rho_0 = 4.82 \cdot 10^8\,\mathrm{As/m^3}$.

Equation (6.49) has two solutions one of which is curl free and one of which is divergence free. Both decouple. The curl free part describes linear plasma oscillations in a cold fluid while the rotational part describes transverse electro-magnetic waves in the plasma. Hence, the first order plasma motion induced by a transverse laser pulse has the property $\nabla \cdot \mathbf{q}_1 = 0$. To second order it is found keeping in mind that a solution with $\nabla \cdot \mathbf{q}_1 = 0$ is required

$$\partial_t^2 \mathbf{q}_2 + c^2 \nabla \times \nabla \times \mathbf{q}_2 + \omega_p^2 \mathbf{q}_2 \quad = \quad -\frac{c}{2} \nabla\, \partial_t\, q_1^2\,. \tag{6.50}$$

The solution of (6.50) is

$$\mathbf{q}_2 = -\frac{c}{2\omega_p^2} \nabla \partial_t \Phi\,, \tag{6.51}$$

$$\Phi = \omega_p \int_{-\infty}^{t} d\tau\ \sin\omega_p(t-\tau)\ q_1^2(\mathbf{r},\tau)\,, \tag{6.52}$$

$$\omega_p^2 q_1^2 = \partial_t^2 \Phi + \omega_p^2 \Phi\,. \tag{6.53}$$

A formal approach to solve the linear differential equation (6.50) is the Fourier technique. The right of Equation (6.50) implies that the solution is irrotational. In addition, it is required that the solution vanishes for $t \to -\infty$ and that there is no plasma perturbation in front of the pulse. The first requirement implies

$$\mathbf{q}_2(\mathbf{r},t) \quad = \quad \int_{-\infty}^{\infty} \frac{d\omega}{2\pi} \int_{-\infty}^{\infty} \frac{d\mathbf{k}}{(2\pi)^3}\, e^{-i(\omega+i\epsilon)t}\, e^{i\mathbf{k}\cdot\mathbf{r}}\, \tilde{\mathbf{q}}_2(\mathbf{k},\omega)\,, \tag{6.54}$$

where

$$\tilde{\mathbf{q}}_2(\mathbf{k},\omega) \quad = \quad \frac{c}{2}\, \frac{\omega}{(\omega+i\epsilon)^2 - \omega_p^2}\, \mathbf{k}\, q_1^2(\mathbf{k},\omega)\,. \tag{6.55}$$

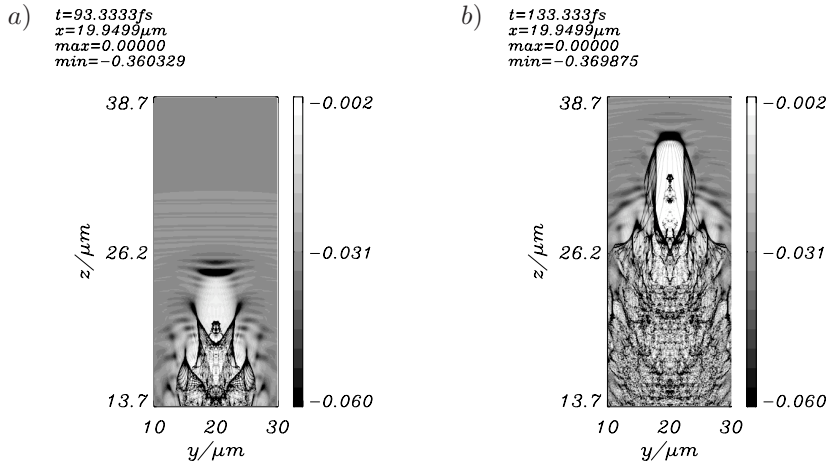

Figure 6.8: Electron capture in a self-focusing laser beam in 2D. The simulation plane is the one depicted in Fig. 6.4. The laser is s-polarized and propagates along the z-axis. The figure shows the field ρ_e at $t = 93\,\mathrm{fs}$ (a) and $t = 133\,\mathrm{fs}$ (b). The color-bars to the right show the selected data range for the plots, while the maximum and minimum values of the field are printed at the top of each plot. The units of the fields are $\rho_0 = 4.82 \cdot 10^8\,\mathrm{As/m^3}$.

Performing the contour integrations in Equation (6.54) it is obtained

$$\mathbf{q}_2(\mathbf{r},t) \;=\; -\frac{c}{4}\,\nabla\left(e^{-i\omega_p t}q_1^2(\mathbf{r},\omega_p) + e^{i\omega_p t}q_1^2(\mathbf{r},-\omega_p)\right)\;. \tag{6.56}$$

The requirement that there is no plasma perturbation in front of the pulse gives

$$q_1^2(\mathbf{r},\omega_p) \;=\; \frac{i}{\omega_p}\int_{-\infty}^{t} d\tau\; e^{i\omega_p\tau}\;\partial_\tau q_1^2(\mathbf{r},\tau)\;. \tag{6.57}$$

Inserting Equation (6.57) into (6.56) Equations (6.51) and (6.52) are obtained. Since $\mathbf{q}_2$ is irrotational there is no second order contribution to the magnetic field.

However, electric wake-field generation is already described by Equations (6.45), (6.50), (6.51) and (6.52). It is found to second order

$$\mathbf{E}_2 \;=\; -\frac{mc^2}{2e}\,\nabla\Phi\;, \tag{6.58}$$

$$n_2 \;=\; n_0\left(1+\frac{c^2}{2\omega_p^2}\Delta\Phi\right)\;, \tag{6.59}$$

$$\mathbf{v}_2 \;=\; -\frac{c^2}{2\omega_p^2}\partial_t\nabla\Phi\;. \tag{6.60}$$

To proceed we transform from the lab system into the speed of light frame coordinates for which we take assuming rotational symmetry around the axis ρ, z and $\xi = ct - z$ as independent variables. We obtain

$$\mathbf{E}_{2\perp} \;=\; -\frac{mc^2}{2e}\,\partial_\rho\Phi\;\mathbf{e}_\rho\;, \tag{6.61}$$

$$\mathbf{E}_{2z} \;=\; \frac{mc^2}{2e}\,\partial_\xi\Phi\;\mathbf{e}_z\;, \tag{6.62}$$

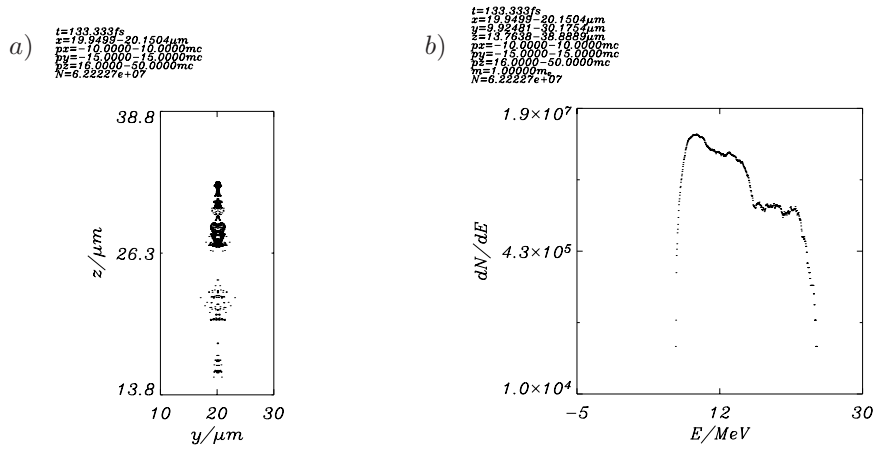

Figure 6.9: Phase space of trapped electrons generated by a self-focusing laser beam in 2D. The simulation plane is the one depicted in Fig. 6.4. The laser is s-polarized and propagates along the z-axis. The figure shows (a) the yz-projection of electron phase space and (b) the electron energy spectrum.after $t = 133\,\mathrm{fs}$. The normalization of the momenta is $m_e c$. In the top left corner of each plot the sampling range in phase space for the electrons has been printed.

$$\Phi = k_p \int_{-\infty}^{\xi} d\tau \ \sin k_p(\xi - \tau)\ q_1^2(\rho, \tau)\ , \tag{6.63}$$

where $k_p = \omega_p/c$. The speed of light frame coordinates are chosen such that the laser pulse propagates from the right to the left. If L denotes the rear end of the laser pulse then we obtain behind it ($\xi > L$)

$$\Phi = \psi_1(\rho)\ \sin(k_p\xi) - \psi_2(\rho)\cos(k_p\xi)\ , \tag{6.64}$$

$$\psi_1(\rho) = k_p \int_{-\infty}^{L} d\tau \cos k_p\tau\ q_1^2(\rho, \tau)\ , \tag{6.65}$$

$$\psi_2(\rho) = k_p \int_{-\infty}^{L} d\tau \sin k_p\tau\ q_1^2(\rho, \tau)\ , \tag{6.66}$$

where the relation $\sin(x - y) = \sin x \cos y - \sin y \cos x$ has been used. We may draw some immediate conclusions from Equations (6.61), (6.62) and (6.64). The first conclusion is that the transverse and longitudinal wake-fields are phase shifted by $\pi/2$. A second observation is that the wavelength of the electric plasma wake is $2\pi/k_p$. This is reproduced by the simulation in two spatial dimensions as we will see later. All the simulations are performed for Gaussian time and beam envelopes and for density profiles which are constant with the exception of the front and rear edges which have finite transition gradients. Finally, we can conclude that the relative magnitude of the longitudinal and transverse electric wake-fields is determined by k_p and the transverse gradient. Assuming that the shape of the radial beam envelope taken in the simulations is $I = I_0\ \exp\left(-\rho^2/\rho_s^2\right)$ we obtain with the help of (6.61) and (6.62) $|E_z(\rho_m)|/|\mathbf{E}_\perp(\rho_m)| \approx k_p\rho_m$, where $\rho_m = \rho_s/\sqrt{2}$ is the location of the extremum of the radial derivative of the beam envelope. Simulations have been reported in [36].

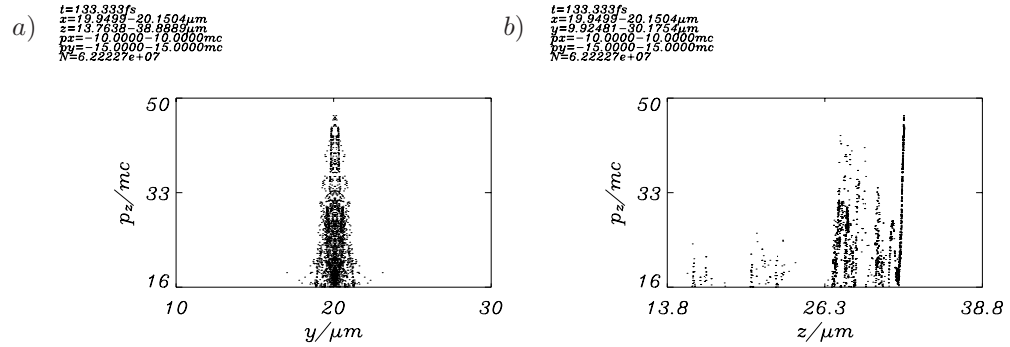

Figure 6.10: Phase space of trapped electrons generated by a self-focusing laser beam in 2D. The simulation plane is the one depicted in Fig. 6.4. The laser is s-polarized and propagates along the z-axis. The figure shows (a) yp_z- and (b) the zp_z-projections of the electron phase space after $t = 133\,\mathrm{fs}$. The normalization of the momenta is $m_e c$. In the top left corner of each plot the sampling range in phase space for the electrons has been printed.

If we look for a solution of Equation (6.47) in the Coulomb gauge ($\nabla \cdot \mathbf{q} = 0$) we obtain

$$\begin{aligned}\left(\Delta - \frac{1}{c^2}\partial_t^2\right)\mathbf{q} &= \frac{\omega_p^2}{c^2}\frac{\mathbf{q}}{\sqrt{1+q^2}}\left[1 + \frac{c^2}{\omega_p^2}\Delta\sqrt{1+q^2}\right] \\ &\quad + \frac{1}{c}\,\partial_t \nabla\sqrt{1+q^2}\,.\end{aligned} \tag{6.67}$$

We may next make assumptions on spatial and temporal scales. We assume that the transverse spatial variations (perpendicular to the pulse propagation direction) of the beam envelope are much more rapid than the longitudinal ones. Introducing the variables ρ, z and $\xi = z - ct$ as independent variables and making the ansatz

$$\begin{aligned}\mathbf{q}_\perp(\rho, z, \xi) &= \frac{1}{2}\left[(\mathbf{e}_x + i\mathbf{e}_y)\; q(\epsilon\rho, \epsilon^2 z, \epsilon^2\xi)\; \exp(ik\xi) + c.c\right]\,, \\ q_z &= 0\,,\end{aligned} \tag{6.68}$$

which neglects plasma wave generation with the additional requirement $\epsilon = \omega_p/\omega \ll 1$ we find

$$(\Delta_\perp + 2ik\partial_z)\,\mathbf{q} = \frac{\omega_p^2}{c^2}\,\frac{\mathbf{q}}{\sqrt{1+q^2}}\,\left[1 + \frac{c^2}{\omega_p^2}\,\Delta_\perp\sqrt{1+|q|^2}\right]\,. \tag{6.69}$$

In Equation (6.69) only terms up to order ϵ^2 have been kept. This equation is equivalent to Equations (6.19) and (6.20). The inclusion of plasma waves may be obtained up to second order in v_{os}/c by making use of the second order solution given in (6.51), (6.52) and (6.53). Neglecting higher order contributions of $\partial_t\nabla\sqrt{1+q^2}$ we find

$$\begin{aligned}&\left(\Delta - \frac{1}{c^2}\partial_t^2\right)\mathbf{q} \\ &= \frac{\omega_p^2}{c^2}\frac{\mathbf{q}}{\sqrt{1+q^2}}\,\left[1 + \frac{c^2}{2\omega_p}\,\Delta\int_{-\infty}^{t} d\tau\;\sin\omega_p(t-\tau)\;\mathbf{q}^2\right]\,.\end{aligned} \tag{6.70}$$

Equation (6.70) describes the interaction between density modulations by wake-field generation in the body of the laser pulse, self-focusing and enhanced diffraction. Envelope equations for (6.70) may be found in [43]. Instabilities arising from Equation (6.70) are know as self-modulation instabilities. The physical mechanism is understood straight forwardly. The finite rise time of the front edge of the laser pulse generates density oscillations. In regions of high density enhanced diffraction is obtained while in low density regions enhanced focusing occurs. Thus, the pulse energy is transversely and longitudinally redistributed and the pulse splits into beam-lets whose length is $2\pi/k_p$.

To find the magnetic field, we next proceed to the third order in the systematic momentum expansion. We obtain

$$\begin{aligned} & \partial_t^2 \mathbf{q}_3 + c^2 \nabla \times \nabla \times \mathbf{q}_3 + \omega_p^2 \mathbf{q}_3 \qquad (6.71) \\ = \quad & \mathbf{q}_1 \left(\frac{1}{2} \left[\omega_p^2 - c^2 \Delta \right] q_1^2 - c \nabla \cdot \partial_t \mathbf{q}_2 \right) - c \partial_t \nabla \ (\mathbf{q}_1 \cdot \mathbf{q}_2) \ . \end{aligned}$$

Finally, to fourth order we find

$$\begin{aligned} & \partial_t^2 \mathbf{q}_4 + c^2 \nabla \times \nabla \times \mathbf{q}_4 + \omega_p^2 \mathbf{q}_4 \qquad (6.72) \\ = \quad & -\frac{c}{2} \partial_t \nabla \left[q_2^2 + 2 \mathbf{q}_1 \cdot \mathbf{q}_3 - \frac{1}{2} \left(q_1^4 + 4 \mathbf{q}_1 \cdot \mathbf{q_3} \right) \right] \\ & + \mathbf{q}_1 \left(\frac{1}{2} \left[\omega_p^2 - c^2 \Delta \right] \mathbf{q}_1 \cdot \mathbf{q}_2 - c \partial_t \nabla \cdot \mathbf{q}_3 \right) \\ & + \mathbf{q}_2 \left(\frac{1}{2} \left[\omega_p^2 - c^2 \Delta \right] q_1^2 - c \partial_t \nabla \cdot \mathbf{q}_2 \right) \ . \end{aligned}$$

Taking the curl of both sides of Equation (6.72) we ultimately obtain

$$\left(\partial_t^2 - c^2 \Delta + \omega_p^2 \right) \mathbf{B}_4 \quad = \quad \frac{1}{\epsilon_0} \nabla \times \left(\mathbf{j}_1 + \mathbf{j}_2 \right) \ , \qquad (6.73)$$

where

$$\mathbf{j}_1 \quad = \quad \frac{\epsilon_0 mc}{e} \, \mathbf{q}_2 \left(\frac{1}{2} \left[\omega_p^2 - c^2 \Delta \right] q_1^2 - c \partial_t \nabla \cdot \mathbf{q}_2 \right) \ , \qquad (6.74)$$

$$\mathbf{j}_2 \quad = \quad \frac{\epsilon_0 mc}{e} \, \mathbf{q}_1 \left(\frac{1}{2} \left[\omega_p^2 - c^2 \Delta \right] \mathbf{q}_1 \cdot \mathbf{q}_2 - c \partial_t \nabla \cdot \mathbf{q}_3 \right) \ . \qquad (6.75)$$

According to Equation (6.75) an explicit expression for $\nabla \cdot \mathbf{q}_3$ is required. Therefore, from Equation (6.71)

$$\begin{aligned} \left(\partial_t^2 + \omega_p^2 \right) \nabla \cdot \mathbf{q}_3 \quad = \quad & \mathbf{q}_1 \cdot \nabla \left(\frac{1}{2} \left[\omega_p^2 - c^2 \Delta \right] q_1^2 - c \nabla \cdot \partial_t \mathbf{q}_2 \right) \qquad (6.76) \\ & - c \, \partial_t \Delta \ (\mathbf{q}_1 \cdot \mathbf{q}_2) \ , \end{aligned}$$

the solution of which is

$$\begin{aligned} \nabla \cdot \mathbf{q}_3 \quad = \quad & \frac{1}{\omega_p} \int_{-\infty}^{t} d\tau \ \sin \omega_p (t - \tau) \qquad (6.77) \\ & \times \left\{ \mathbf{q}_1 \cdot \nabla \left(\frac{1}{2} \left[\omega_p^2 - c^2 \Delta \right] q_1^2 - c \partial_\tau \nabla \cdot \mathbf{q}_2 \right) - c \ \partial_\tau \Delta \ (\mathbf{q}_1 \cdot \mathbf{q}_2) \right\} \ . \end{aligned}$$

With the help of relation (6.53) and Equation (6.77) we bring the currents Equations (6.74) and (6.75) into the form

$$\mathbf{j}_1 = \frac{n_0 e c^2}{4\omega_p^2}\,(\nabla\partial_t\Phi)\,\left[q_1^2 - \frac{c^2}{\omega_p^2}\Delta\Phi\right]\,, \tag{6.78}$$

$$\mathbf{j}_2 = e n_0 c\,\mathbf{q}_1\left\{\mathbf{q}_1\cdot\mathbf{q}_2 - \frac{c^2}{\omega_p}\Delta\int_{-\infty}^{t} d\tau\,\sin\omega_p(t-\tau)\;\mathbf{q}_1\cdot\mathbf{q_2}\right. \tag{6.79}$$
$$\left. -\frac{c}{2}\int_{-\infty}^{t} d\tau\,\cos\omega_p(t-\tau)\;\mathbf{q}_1\cdot\nabla\left[q_1^2 - \frac{c^2}{\omega_p^2}\Delta\Phi\right]\right\}\,.$$

To proceed further a solution for $\mathbf{q}_1$ is required. Taking the speed of light frame coordinates z, ρ and $\xi = ct - z$ and making the ansatz

$$\mathbf{q}_1(\rho,z,\xi) = \frac{1}{2}\left[\mathbf{a}(\rho,z,\xi)\;\exp\left(-ik\xi\right) + c.c\;\right]\,, \tag{6.80}$$

with an amplitude $\mathbf{a}(\rho,z,\xi)$ that varies slowly in space and time, we find for Equation (6.49)

$$(\Delta_\perp - 2ik\partial_z)\,\mathbf{a} = \frac{\omega^2}{c^2}\;\left(1-\eta_1^2\right)\mathbf{a}\,, \tag{6.81}$$

$$\mathbf{a}(\rho,z,\xi) = \mathbf{a}_0(\xi)\;\frac{\rho_0}{\rho_s(z)}\;\exp\left(-\left[1-i\alpha_s(z)\right]\frac{\rho^2}{\rho_s^2(z)} + i\theta_s(z)\right)\,, \tag{6.82}$$

where $\eta_1^2 = 1-\omega_p^2/\omega^2$. For the envelope equations we get from (6.31) and (6.32)

$$\alpha_s(z) = -\frac{k\rho_s^2(z)}{2}\;\partial_z\rho_s(z)\,, \tag{6.83}$$

$$\partial_z\theta_s(z) = \frac{2}{k\rho_s^2(z)} + \frac{k}{2}\;\frac{\omega_p^2}{\omega^2}\,, \tag{6.84}$$

$$\partial_z^2\rho_s(z) = \frac{4}{k^2\rho_s^3(z)}\,. \tag{6.85}$$

If the laser pulse is sufficiently broad ($\rho_s\to\infty$) we may easily solve the envelope equations (6.83) to obtain $\alpha_s \approx 0$ and $\theta_s \approx -kz\omega_p^2/2\omega^2$. From Equation (6.81) follows $k = \omega/c$. Hence, we obtain with the help of Equations (6.49) and (6.80) the relation $\omega^2 \approx \omega_p^2 + c^2k^2$. The function $\mathbf{a}$ becomes a function of ρ and ξ. The self-generated magnetic field will in general have a quasi-steady component as well as high-harmonic contributions. Here, the interest is in the quasi-steady part which to leading order is given by the current [48, 113]

$$\mathbf{j} = \frac{n_0 e c^2}{4\omega_p^2}\,(\nabla\partial_t\Phi_0)\,\left[\frac{|\mathbf{a}|^2}{2} - \frac{c^2}{\omega_p^2}\Delta\Phi_0\right]\,, \tag{6.86}$$

$$\Phi_0 = \frac{\omega_p}{2}\;\int_{-\infty}^{t} d\tau\;\sin\omega_p(t-\tau)\;|\mathbf{a}(\rho,\tau)|^2\,, \tag{6.87}$$

where Equation (6.80) has been used. In the speed of light frame coordinates we have

$$\partial_\xi^2\Phi_0 = \frac{\omega_p^2}{2c^2}\;|\mathbf{a}|^2 - \frac{\omega_p^2}{c^2}\;\Phi_0\,, \tag{6.88}$$

$$\Phi_0 = \frac{k_p}{2}\int_{-\infty}^{\xi} d\tau\;\sin k_p(\xi-\tau)\;\left|a(\rho,\tau)\right|^2\,. \tag{6.89}$$

With the help of Equation (6.88) and the speed of light frame coordinates for Equations (6.86) and (6.87) follows

$$j_z = \frac{ecn_0}{4k_p^4}\left(\partial_\xi^2\Phi_0\right)\ \left[\left(k_p^2-\Delta_\perp\right)\Phi_0\right]\ , \tag{6.90}$$

$$j_\rho = -\frac{ecn_0}{4k_p^4}\left(\partial_\rho\partial_\xi\Phi_0\right)\ \left[\left(k_p^2-\Delta_\perp\right)\Phi_0\right]\ . \tag{6.91}$$

Performing the curl of the current given by (6.90) and (6.91) we find that there is only an $\mathbf{e}_\phi$ component of $\mathbf{B}$ implying $\mathbf{B} = B\ (-\sin\phi, \cos\phi, 0)$. Using (6.73) we get

$$\left(\frac{1}{\rho}\partial_\rho\rho\partial_\rho - \frac{1}{\rho^2} - 1\right)B_\phi = -F(\rho,\xi)\ , \tag{6.92}$$

$$F(\rho,\xi) = \left(\partial_\rho\partial_\xi\Phi_0\right)\partial_\xi\left(1-\Delta_\perp\right)\Phi_0 - \left(\partial_\xi^2\Phi_0\right)\partial_\rho\left(1-\Delta_\perp\right)\Phi_0\ , \tag{6.93}$$

where $\rho \to k_p\rho$ and $B_\phi \to \epsilon_0 c k_p B_\phi/en_0$. Since Φ_0 is a function of the laser intensity and F contains terms proportional to Φ_0^2 the magnetic field $\mathbf{B}$ scales like the second power of the laser intensity. We next look for a solution for B_ϕ that disappears at $\rho = 0$ and $\rho \to \infty$. We find

$$\begin{aligned} B_\phi = \Bigg[& -I_1(\rho)\ \int_\infty^\rho drrK_1(r)F(r,\xi) \\ & +K_1(r)\ \int_0^\rho drrI_1(r)F(r,\xi)\Bigg]\ . \end{aligned} \tag{6.94}$$

The functions $I_1(\rho)$ and $K_1(\rho)$ are modified Bessel functions obeying the relations [87]

$$\frac{1}{\rho}\partial_\rho\rho\partial_\rho I_1 - \left(\frac{1}{\rho^2}+1\right)I_1 = 0\ , \tag{6.95}$$

$$\frac{1}{\rho}\partial_\rho\rho\partial_\rho K_1 - \left(\frac{1}{\rho^2}+1\right)K_1 = 0\ , \tag{6.96}$$

$$\rho\partial_\rho K_1 + K_1 = -\rho K_0\ , \tag{6.97}$$

$$\rho\partial_\rho I_1 + I_1 = \rho I_0\ , \tag{6.98}$$

$$I_0K_1 + I_1K_0 = \frac{1}{\rho}\ . \tag{6.99}$$

With the help of the relations (6.95), (6.96), (6.97), (6.98), and (6.99) it is straight forward to verify that Equation (6.94) is a solution of Equation (6.92). The shape of the magnetic field is essentially determined by the function F given in Equation (6.93). The function F in turn depends on the pulse shape via Φ_0 given in Equation (6.87). However, behind the pulse the quasi-steady magnetic field adopts a universal form similar to the situation for the electric wake-field. This is seen by recalling that behind the laser pulse we have $\xi > L$. Hence, we obtain

$$\Phi_0 = A\ \sin(k_p\xi - \theta)\ , \tag{6.100}$$

$$A = \sqrt{A_1^2 + A_2^2}\ , \tag{6.101}$$

$$\tan\theta = \frac{A_1}{A_2}\ , \tag{6.102}$$

$$A_1 = \frac{k_p}{2}\int_{-\infty}^L d\tau\cos k_p\tau\ |a(\rho,\tau)|^2\ , \tag{6.103}$$

$$A_2 \;=\; \frac{k_p}{2}\int_{-\infty}^{L} d\tau \sin k_p\tau \;\; |a(\rho,\tau)|^2 \; .$$

Next we assume the the laser pulse is adequately represented by

$$|a(\rho,\xi)|^2 \;=\; a_0^2 \; f_1(\xi) \; f_2(\rho) \; , \tag{6.104}$$

where f_1 gives the beam envelope in propagation direction and f_2 the transverse pulse shape. The value a_0^2 determines the peak normalized intensity of the laser pulse. With the help of Equations (6.100), (6.101), (6.102), (6.103), (6.104), and (6.104), it is easy to show that the form of F given by Equation (6.93) is

$$\begin{aligned} F(\rho,\xi) \;=\; & \frac{k_p^2}{2} \; \left[\partial_\rho \left(A^2 - A\Delta_\perp A\right)\right. \\ & \left. + \left[A\partial_\rho\Delta_\perp A - (\partial_\rho A)\Delta_\perp A\right] \; \cos 2(k_p\xi - \theta)\right] \; , \end{aligned} \tag{6.105}$$

where

$$A \;=\; a_0^2 \; f_2(\rho) \; \sqrt{Z_1^2 + Z_2^2} \; , \qquad \tan\theta = \frac{Z_1}{Z_2} \; , \tag{6.106}$$

and

$$\begin{aligned} Z_1 \;&=\; \frac{k_p}{2}\int_{-\infty}^{L} d\tau \cos k_p\tau \; f_1(\tau) \; , \\ Z_2 \;&=\; \frac{k_p}{2}\int_{-\infty}^{L} d\tau \sin k_p\tau \; f_1(\tau) \; . \end{aligned} \tag{6.107}$$

Thus, the magnetic wake-field has a component that is constant along ξ and a component that oscillates with $2k_p$ in longitudinal direction, where k_p is the wavelength of the electric wake-field. An intuitive way to understand the $2k_p$ oscillation in fourth order is obtained writing the quasi steady current Equation (6.86) in the form $\mathbf{j} = -en_0\delta n_2\mathbf{v}_2$, where δn_2 and $\mathbf{v}_2$ are obtained from Equation (6.58). Both, δn_2 and $\mathbf{v}_2$ oscillate with k_p giving constant as well as $2k_p$ contributions. Simulation results are reported in [49].

6.2.1 Wake field simulations in 2D

In this subsection we present wakefield simulations with the PSC in 2D. The theoretical background has been laid out in section 6.2. While the theory is only valid for sub-relativistic intensities ($a = v_{os}/c \ll 1$), the numerical model can be extended to much larger values of a. The plasma we consider consists of electrons and protons. The peak electron plasma density must be sub-critical for laser-wakefield generation (see section 6.2). This means that $\omega > \omega_{pe}$ must hold. Since the plasma density for a sub-critical plasma is low and the proton charge can only be $Z = 1$ we neglect collisions. Hence, the collision module **PIC_bin_coll.f** has been commented out in **VLI.f** and **VLA.f**.

We begin by describing the setup of the simulation. Figure 6.11 depicts the simulation box, which we have selected for the simulation. A Cartesian right-handed coordinate system has been attached to the box, the origin of which is denoted by $(0, 0, 0)$. The same coordinate system is used in the PSC. The simulation box is 3D. However, we only select a 2D simulation plane depicted by the shaded area in the figure. The sector shaded in dark represents the plasma. The size of the simulation box is set up in **INIT_param.f**. We select a 3D simulation box of $40\,\mu$m$\times 40\,\mu$m$\times 50\,\mu$m. This is done by setting $lengthx = 40\,\mu$m, $lengthy =$

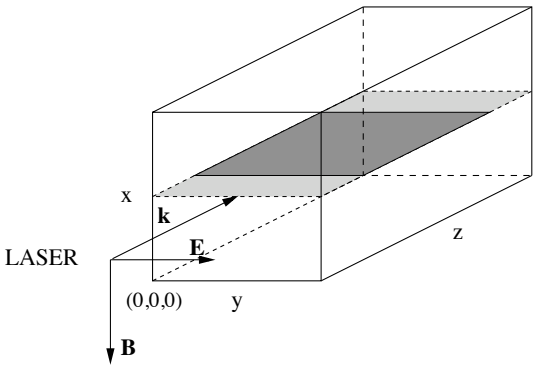

Figure 6.11: Wake field simulation in 2D. The figure shows the simulation box that harbors the simulation plane in 2D. The box defines a coordinate system, the origin of which is at $(0,0,0)$. The direction of the incident laser pulse is along the z-axis. It is indicated by $\vec{k}$ at the front side of the box. The laser field polarization is also depicted by $\vec{E}$. Since the electric field is parallel to the simulation plane the laser pulse is called p-polarized.

$40\,\mu$m, and $lengthz = 50\,\mu$m. The number of grid points of the spatial grid is $400\times400\times1000$. This grid size is established by setting $i1tot = 400$, $i2tot = 400$, and $i3tot = 1000$. For the 2D plane in Fig. 6.11, however, only 400×1000 cells are used by assigning $i1n = 199$, $i1x = 199$, $i2n = 0$, $i2x = 399$, $i3n = 0$, and $i3x = 999$. The plasma density required for normalization in the PSC (see subsection 4.1) is determined by $n0$. We set $n0 = 10^{25}\,\mathrm{m}^{-3}$. The electric field strength $e0$ (see subsection 4.1) is obtained with the help of the laser intensity $i0$. We choose $i0 = 2.0 \cdot 10^{22}\,\mathrm{Wm}^{-2}$. The laser frequency wl is determined with the help of the laser wavelength lw. We take $lw = 10^{-6}\,\mathrm{m}$. We select periodic boundaries for the Maxwell fields and the quasi-particles along the x- and y-directions. However, we choose the radiating boundary condition at $z = 0$ for the fields and reflecting boundary conditions for the particles. At $z = 50\,\mu$m we select the radiating boundary for the fields too. But, we place no laser pulse. Under this condition radiation from inside the simulation box can freely escape. The particles are again reflected at $z = 50\,\mu$m. The boundary conditions are set up by selecting $boundary\_field\_x = 1$, $boundary\_field\_y = 1$, $boundary\_field\_z = 0$, $boundary\_part\_x = 1$, $boundary\_part\_y = 1$, and $bounday\_part\_z = 0$. Since the simulation is very small we choose to carry it out on a single node. This implies $xnpe = 1$, $ynpe = 1$, and $znpe = 1$. The filesystems selected for the data output and check-pointing data are the ones from which the simulation is started. This means $data\_out =$ "./" and $data\_chk =$ "./". The maximum permissible CPU time for a single run is set with the help of the parameter $cpum$. We choose $cpum = 6000$, which means 6000 sec. After 6000 sec the PSC check-points its data core and restarts the simulation from the latter. The maximum permissible number of time steps is given by $nmax$. We select $nmax = 2000$. The parameters for data output control have been adjusted such that output for the time resolved fields and particles is generated every four full laser cycles, which means after $np = 4\,nnp$ time steps, where nnp is the number of time steps for a full laser cycle. Every particle is recorded after np time steps. The relevant settings are $nprf = 0$, $dnprf = np$, $nprc = 0$, $dnprc = np$, $nprparti = 0$, $dnprparti = np$, $nistep = 1$. Time-averaging is repeatedly done over a full laser cycle. The required settings are $tmnvf = 1$, $tmxvf = nnp$, $tmnvp = 1$, and $tmxvp = nnp$. While $n0$ sets the density for the normalization in the PSC, the file **INIT_den.f** is required to

determine the shape and location of the plasma in the simulation box. The coordinate system used for setting up the density is the same as the one that defines the simulation box. The origin of the coordinate system is $(0, 0, 0)$. The default density function provided with the PSC makes use of nine parameters. They are explained in subsection 5.1. For the wakefield simulation we choose $x0 = 2 \cdot 10^{-5}\,\mathrm{m}$, $y0 = 2 \cdot 10^{-5}\,\mathrm{m}$, and $z0 = 2.5 \cdot 10^{-5}\,\mathrm{m}$. For the gradient lengths at the plasma boundaries we use $Lx = 10^{-8}\,\mathrm{m}$, $Ly = 10^{-8}\,\mathrm{m}$, and $Lz = 5 \cdot 10^{-8}\,\mathrm{m}$. The width of the plasma is given by $widthx = 10^{-4}\,\mathrm{m}$, $widthy = 10^{-4}\,\mathrm{m}$, and $widthz = 2 \cdot 10^{-5}\,\mathrm{m}$. The initial location, direction, and polarization of the laser pulse is set with the help of twelve files. Details are listed in subsection 5.1. The laser pulse is assumed to propagate along the z-axis and to be p-polarized, which means that the electric field vector of the laser oscillates in the simulation plane depicted in Fig. 6.11. Hence, we turn off all antennas except **INIT_ppulse_z1.f**, which irradiates the plasma through the surface at $z = 0$ along z. The coordinate frame for the laser pulse is the same as the one for the simulation box. The default initial shape of the laser pulse in space shipped with the PSC is a Gaussian. We choose $1\,\mu$m at full-width-half-maximum (FWHM) in propagation direction. The widths in lateral directions are $5\,\mu$m. At startup time of the simulation the laser pulse is placed at $(20\,\mu\mathrm{m}, 20\,\mu\mathrm{m}, -2\,\mu\mathrm{m})$, which is the center of the xy-plane $2\,\mu$m in front of the simulation box. This means $xm = 2 \cdot 10^{-5}\,\mathrm{m}$, $ym = 2 \cdot 10^{-5}\,\mathrm{m}$, and $zm = -2 \cdot 10^{-6}\,\mathrm{m}$. The laser pulse widths are $dxm = 5 \cdot 10^{-6}\,\mathrm{m}$, $dym = 5 \cdot 10^{-6}\,\mathrm{m}$, and $dzm = 10^{-6}\,\mathrm{m}$. The distribution functions are set up with the help of the file **INIT_idistr.f**. We choose to perform the simulation for electrons and protons and take only one particle per cell for each particle sort. This means that we set $nicell = 1$. Since we deal with electrons and protons we have two entries for particle properties, one for electrons and one for protons. For the electron charge we choose $q_e = -1.6 \cdot 10^{-19}\,\mathrm{As}$, for the electrons mass $m_e = 9.1 \cdot 10^{-31}\,\mathrm{kg}$, and for the electron temperature $T_e = 0\,\mathrm{keV}$. This means $qni = -1.0$, $mni = 1.0$, and $tni = 0.0$. For the protons we set $qni = 1.0$, $mni = 1836$, and $tni = 0.0$. In case **OpenPBS** is available (see subsection 5.1.6) the scripts **vliexec** to **IDLATOM** have to be adapted to the local computing environment (see subsection 5.1). It is further necessary to adapt the IDL files shipped with the PSC in case the intent is to use them (see subsection 5.1.5). The post-processors **PROCESSOR_pfield** to **PROCESSOR_atom** require no adaptions.

We continue by describing the simulation results. During runtime the PSC records diagnostic data in the file **VLA.data**, that can be used to trace possible irregularities. The file contains most setup parameters and the wall clock time for each time-step. The file shows that 400000 cells and 640000 quasi-particles have been allocated for the simulation. The required memory is about 370 MByte. The run takes about 9 sec of wall clock time per time step. Figures 6.12 and 6.13 show plots of the transverse electric field E_y, the electron density ρ_e, the longitudinal electric field E_z, and the magnetic field B_x. The units are given in the figure. As has been predicted by the theoretical considerations in section 6.2, we find transverse (E_y), longitudinal (E_z), and magnetic wakefields (B_x). The longitudinal wakefield acquires field strength of more than $10\,\mathrm{GeV/m}$ and oscillates with k_p (see section 6.2 for a definition). The transverse wakefield E_y has the spatial structure predicted by the theory. The same holds for the magnetic wakefield B_x, which oscillates along the z-axis with approximately $2k_p$ as comparison with E_z shows. Since $a > 1$ holds for the simulation, the theory given in section 6.2 cannot be expected to apply strictly to the simulation. It is interesting to look into the electron phase space generated by the short laser pulse considered here. Figure 6.14 shows projections of the electron phase space at $t = 146\,\mathrm{fs}$. The electrons oscillate in the wakefield of the laser. However, the simulation shows that it is not possible to trap electrons in the electric potential of the wake. We do not observe laser-wakefield

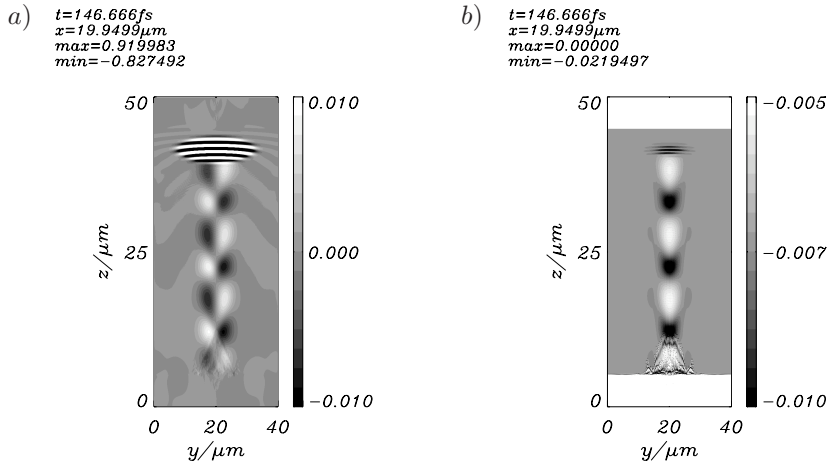

Figure 6.12: Wake field simulation in 2D. The simulation plane is the one depicted in Fig. 6.11. The laser is p-polarized and propagates along the z-axis. The figure shows the fields E_y (a) and ρ_e (b). The time is $t = 146\,\mathrm{fs}$. The color-bars to the right of the plots show the selected data range for the plots, while the maximum and minimum values encountered are printed in the top left corner of the plots, respectively. The units are $E_0 = 3.38 \cdot 10^{12}\,\mathrm{V/m}$ and $\rho_0 = 2.16 \cdot 10^8\,\mathrm{As/m^3}$.

acceleration of electrons for the simulation parameters selected. Electron acceleration occurs at the plasma boundary due to resonance effects (see plot (a) of the figure).

6.2.2 Simulation of self-modulation of laser pulses in 2D

In this subsection we present a simulation of the self-modulation instability of a laser beam with the PSC in 2D. Laser beam self-modulation occurs for laser pulses, that are much longer than the plasma length $2\pi/k_p$ and the power of which is not high enough the surpass the limit of relativistic self-focusing ($P < P_c$). The theoretical background has been laid out in section 6.2. While the theory is strictly valid only for sub-relativistic intensities ($a = v_{os}/c \ll 1$), the numerical model can be extended with confidence to much larger values of a. The plasma we consider consists of electrons and protons. The peak electron plasma density must be sub-critical for laser self-modulation (see section 6.2). This means that $\omega > \omega_{pe}$ must hold. Since the plasma density for a sub-critical plasma is low and the proton charge can only be $Z = 1$ we neglect collisions. Hence, the collision module **PIC_bin_coll.f** has been commented out in **VLI.f** and **VLA.f**.

We begin by describing the setup of the simulation. Figure 6.15 depicts the simulation box, which we have selected for the simulation. A Cartesian right-handed coordinate system has been attached to the box, the origin of which is denoted by $(0, 0, 0)$. The same coordinate system is used in the PSC. The simulation box is 3D. However, we only select a 2D simulation plane depicted by the shaded area in the figure. The sector shaded in dark represents the plasma. The size of the simulation box is set up in **INIT_param.f**. We select a 3D simulation box of $40\,\mu\mathrm{m} \times 40\,\mu\mathrm{m} \times 50\,\mu\mathrm{m}$. This is done by setting $lengthx = 40\,\mu\mathrm{m}$, $lengthy = 40\,\mu\mathrm{m}$, and $lengthz = 50\,\mu\mathrm{m}$. The number of grid points of the spatial grid is $400 \times 400 \times 1000$. This grid size is established by setting $i1tot = 400$, $i2tot = 400$, and $i3tot = 1000$. For the 2D plane in Fig. 6.11, however, only 400×1000 cells are used by assigning $i1n = 199$, $i1x = 199$, $i2n = 0$, $i2x = 399$, $i3n = 0$, and $i3x = 999$. The

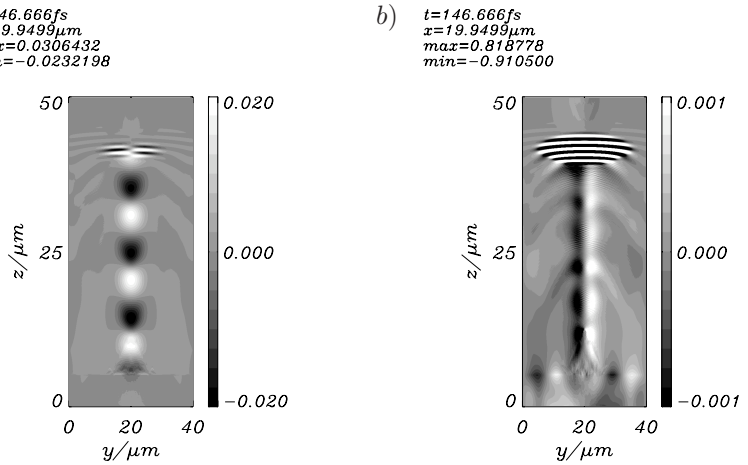

Figure 6.13: Wake field simulation in 2D. The simulation plane is the one depicted in Fig. 6.11. The laser is p-polarized and propagates along the z-axis. The figure shows the fields E_z (a) and B_x (b). The time is $t = 146\,\mathrm{fs}$. The color-bars to the right of the plots show the selected data range for the plots, while the maximum and minimum values encountered are printed in the top left corner of the plots, respectively. The units are $E_0 = 3.38 \cdot 10^{12}\,\mathrm{V/m}$ and $B_0 = 1.29 \cdot 10^4\,\mathrm{Vs/m^2}$.

plasma density required for normalization in the PSC (see subsection 4.1) is determined by $n0$. We set $n0 = 2 \cdot 10^{25}\,\mathrm{m^{-3}}$. The electric field strength $e0$ (see subsection 4.1) is obtained with the help of the laser intensity $i0$. We choose $i0 = 5.0 \cdot 10^{22}\,\mathrm{Wm^{-2}}$. The laser frequency wl is determined with the help of the laser wavelength lw. We take $lw = 10^{-6}\,\mathrm{m}$. We select periodic boundaries for the Maxwell fields and the quasi-particles along the x- and y-directions. However, we choose the radiating boundary condition at $z = 0$ for the fields and reflecting boundary conditions for the particles. At $z = 50\,\mu\mathrm{m}$ we select the radiating boundary for the fields too. But, we place no laser pulse. Under this condition radiation from inside the simulation box can freely escape. The particles are again reflected at $z = 50\,\mu\mathrm{m}$. The boundery conditions are set up by selecting $boundary\_field\_x = 1$, $boundary\_field\_y = 1$, $boundary\_field\_z = 0$, $boundary\_part\_x = 1$, $boundary\_part\_y = 1$, and $bounday\_part\_z = 0$. Since the simulation is very small we choose to carry it out on a single node. This implies $xnpe = 1$, $ynpe = 1$, and $znpe = 1$. The filesystems selected for the data output and check-pointing data are the ones from which the simulation is started. This means $data\_out =$ "./" and $data\_chk =$ "./". The maximum permissible CPU time for a single run is set with the help of the parameter $cpum$. We choose $cpum = 6000$, which means 6000 sec. After 6000 sec the PSC check-points its data core and restarts the simulation from the latter. The maximum permissible number of time steps is given by $nmax$. We select $nmax = 2000$. The parameters for data output control have been adjusted such that output for the time resolved fields and particles is generated every four full laser cycles, which means after $np = 4\,nnp$ time steps, where nnp is the number of time steps for a full laser cycle. Every particle is recorded after np time steps. The relevant settings are $nprf = 0$, $dnprf = np$, $nprc = 0$, $dnprc = np$, $nprparti = 0$, $dnprparti = np$, $nistep = 1$. Time-averaging is repeatedly done over a full laser cycle. The required settings are $tmnvf = 1$, $tmxvf = nnp$, $tmnvp = 1$, and $tmxvp = nnp$. While $n0$ sets the density for the normalization in the PSC, the file **INIT_den.f** is required to determine the shape and

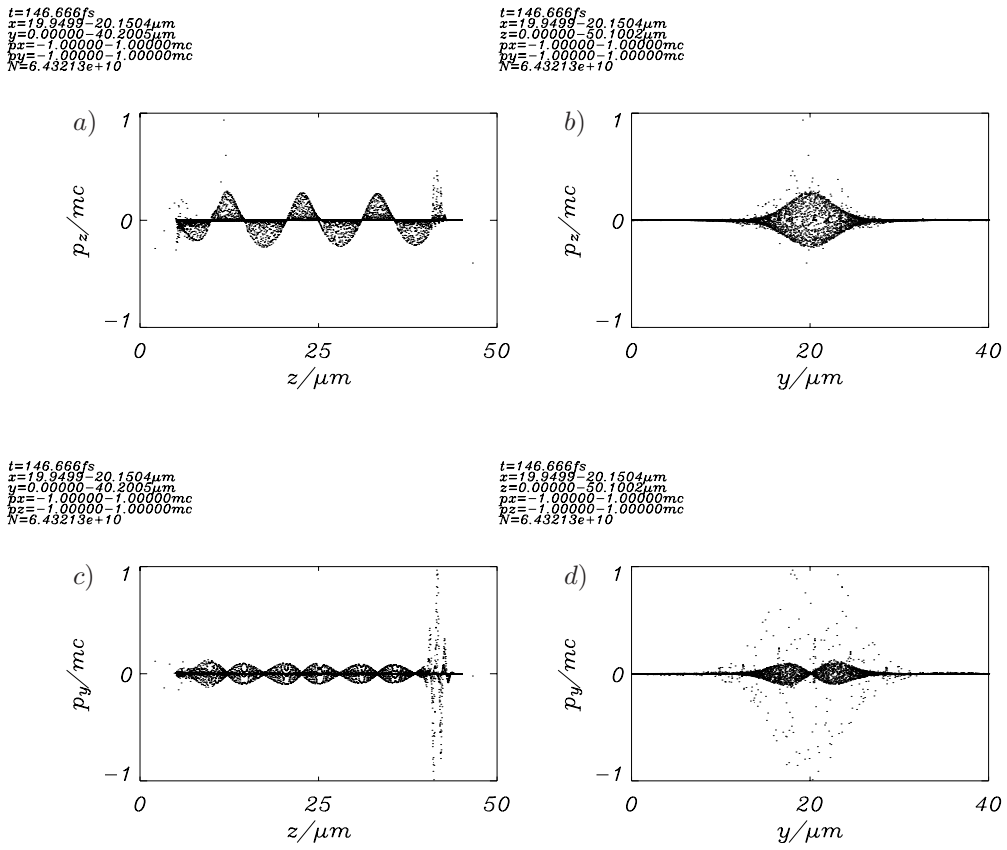

Figure 6.14: Electron phase space for the wake field simulation in 2D. The simulation plane is the one depicted in Fig. 6.11. The laser is p-polarized and propagates along the z-axis. The figure shows (a) the zp_z-, (b) the zp_y-, (c) the yp_z-, and (d) the yp_y-projections of the electron phase space after $t = 146\,\mathrm{fs}$. The momenta are given in units of $m_e c$. In the top left corner of each plot the sampling range in phase space for the electrons has been printed.

location of the plasma in the simulation box. The coordinate system used for setting up the density is the same as the one that defines the simulation box. The origin of the coordinate system is $(0, 0, 0)$. The default density function provided with the PSC makes use of nine parameters. They are explained in subsection 5.1. For the wakefield simulation we choose $x0 = 2 \cdot 10^{-5}\,\mathrm{m}$, $y0 = 2 \cdot 10^{-5}\,\mathrm{m}$, and $z0 = 2.5 \cdot 10^{-5}\,\mathrm{m}$. For the gradient lengths at the plasma boundaries we use $Lx = 10^{-8}\,\mathrm{m}$, $Ly = 10^{-8}\,\mathrm{m}$, and $Lz = 5 \cdot 10^{-8}\,\mathrm{m}$. The width of the plasma is given by $widthx = 10^{-4}\,\mathrm{m}$, $widthy = 10^{-4}\,\mathrm{m}$, and $widthz = 2 \cdot 10^{-5}\,\mathrm{m}$. The initial location, direction, and polarization of the laser pulse is set with the help of twelve files. Details are listed in subsection 5.1. The laser pulse is assumed to propagate along the z-axis and to be p-polarized, which means that the electric field vector of the laser oscillates in the simulation plane depicted in Fig. 6.15. Hence, we turn off all antennas except **INIT_ppulse_z1.f**, which irradiates the plasma through the surface at $z = 0$ along z. The coordinate frame for the laser pulse is the same as the one for the simulation box.

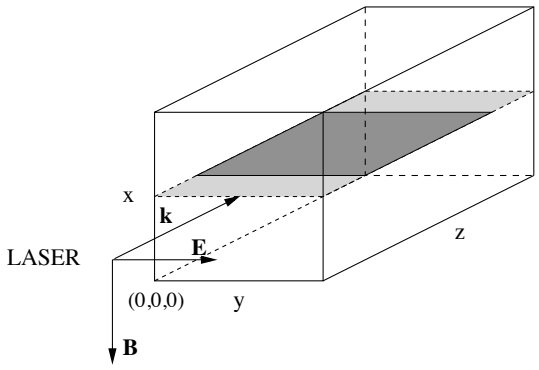

Figure 6.15: Laser beam self-modulation in 2D. The figure shows the simulation box that harbors the simulation plane in 2D. The box defines a coordinate system, the origin of which is at $(0,0,0)$. The direction of the incident laser pulse is along the z-axis. It is indicated by $\vec{k}$ at the front side of the box. The laser field polarization is depicted by $\vec{E}$. Since the electric field is parallel to the simulation plane the laser pulse is called p-polarized.

The default initial shape of the laser pulse in space shipped with the PSC is a Gaussian. We choose a rise length of $1\,\mu$m at full-width-half-maximum (FWHM), after which the intensity remains constant, in propagation direction. The widths in lateral directions are $5\,\mu$m. At startup time the laser pulse is placed at $(20\,\mu\text{m}, 20\,\mu\text{m}, -2\,\mu\text{m})$, which is the center of the xy-plane $2\,\mu$m in front of the simulation box. This means $xm = 2 \cdot 10^{-5}$ m, $ym = 2 \cdot 10^{-5}$ m, and $zm = -2 \cdot 10^{-6}$ m. The laser pulse widths are $dxm = 5 \cdot 10^{-6}$ m, $dym = 5 \cdot 10^{-6}$ m, and $dzm = 10^{-6}$ m. The distribution functions are set up with the help of the file **INIT_idistr.f**. We choose to perform the simulation for electrons and protons and take two particles per cell for each particle sort. This means that we set $nicell = 2$. Since we deal with electrons and protons we have two entries for particle properties, one for electrons and one for protons. For the electron charge we choose $q_e = -1.6 \cdot 10^{-19}$ As, for the electrons mass $m_e = 9.1 \cdot 10^{-31}$ kg, and for the electron temperature $T_e = 0$ keV. This means $qni = -1.0$, $mni = 1.0$, and $tni = 0.0$. For the protons we set $qni = 1.0$, $mni = 1836$, and $tni = 0.0$. In case **OpenPBS** is available (see subsection 5.1.6) the scripts **vliexec** to **IDLATOM** have to be adapted to the local computing environment (see subsection 5.1). It is further necessary to adapt the IDL files shipped with the PSC in case the intent is to use them (see subsection 5.1.5). The post-processors **PROCESSOR_pfield** to **PROCESSOR_atom** require no adaptions.

We continue by describing the simulation results. During runtime the PSC records diagnostic data in the file **VLA.data**, that can be used to trace possible irregularities. The file contains most setup parameters and the wall clock time for each timestep. The file shows that 400000 cells and $1.28 \cdot 10^6$ quasi-particles have been allocated for the simulation. The required memory is about 540 MByte. The run takes about 14 sec of wall clock time per time step. Figures 6.16 and 6.17 show plots of the transverse electric field E_y^2 and the electron density ρ_e. The units are given in the figure. Since the laser pulse is much longer than $2\pi/k_p$ and the irradiated peak power is about $5 \cdot 10^{12}$ W, while the critical power is about 10^{13} W, laser beam self-modulation occurs as has been predicted in section 6.2. However, since $a > 1$ holds for the simulation, the theory given in section 6.2 cannot be expected to apply strictly to the simulation. It is interesting to look into the electron phase space generated by the laser beam considered here. Figures 6.18 and 6.19 show projections of the electron phase

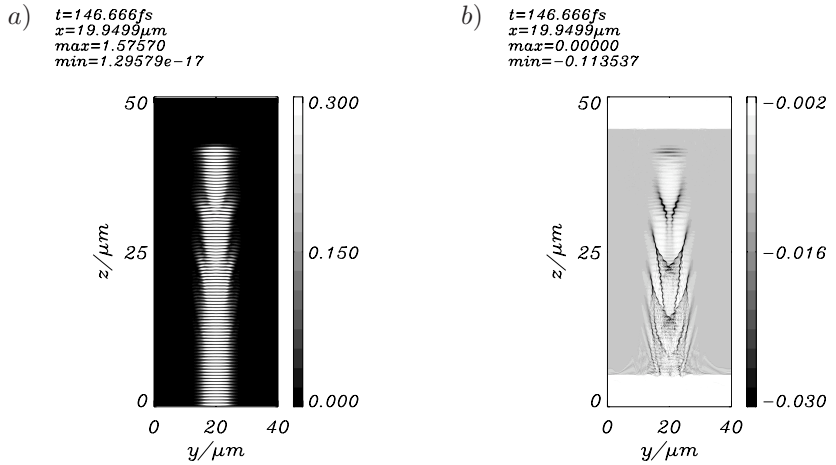

Figure 6.16: Self-modulated laser beam. The simulation plane is the one depicted in Fig. 6.11. The laser is p-polarized and propagates along the z-axis. The fields E_y^2 (a) and ρ_e (b) are shown. The time is $t = 146\,\mathrm{fs}$. The color-bars show the selected data range for each plot, while the maximum and minimum values of the fields are printed in the top left corner of the plots. The units are $E_0 = 6.13 \cdot 10^{12}\,\mathrm{V/m}$ and $\rho_0 = 3.41 \cdot 10^8\,\mathrm{As/m^3}$.

space at $t = 146\,\mathrm{fs}$. The electrons oscillate in the laser field and are accelerated considerably. However, the simulation shows that it is not possible to trap electrons.

6.3 Aspects of plasma absorption

In recent years efforts have been undertaken to understand collective absorption of ultrashort intense laser radiation in plasma. Absorption processes like the anomalous skin effect [53, 58, 118], Brunel heating [58, 59, 61, 119], and $\vec{j} \times \vec{B}$-heating [63] have been investigated intensively. However, big discrepancies between experimental observations [54] and results obtained from theoretical investigations in 1D remained. The correlation between critical surface deformation and high laser absorption was first observed by Wilks *et al.* [51]. They tried to explain their observation pointing out that laser radiation interacting with a deformed critical plasma layer can be considered being obliquely incident. Hence, Wilks *et al.* assumed that the main absorption mechanism was Brunel heating. However, more detailed numerical investigations of Brunel heating carried out by Gibbon *et al.* [61, 119] and Ruhl *et al.* [58] revealed that the effect is suppressed for intense laser irradiation while absorption in deformed targets remains high with growing intensity. Recently, the question of how absorption is related to the evolution of quasi-steady electric fields has been addressed [120]. It was found that they can enhance fractional absorption. However, at present a satisfactory understanding of the numerical and experimental results is still missing. The robustness of absorption in deformed plasma layers suggests that it cannot be solely explained with the help of 1D mechanisms.

In the following we identify various mechanisms that contribute to laser absorption in plasma. We show that plasma surface oscillations couple with the radiation field. This effect is likely to enhance fractional absorption. However, at high laser intensities the ponderomotive pressure is capable of suppressing surface oscillations which may lead to a reduction of absorption with growing intensity.

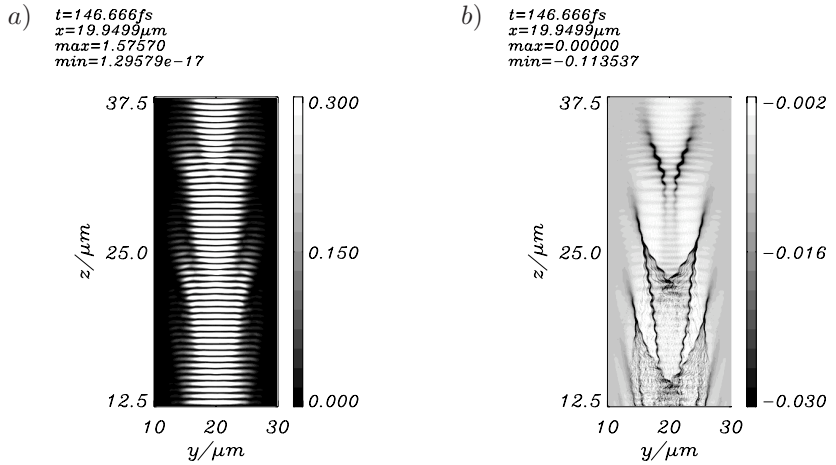

Figure 6.17: Self-modulated laser beam. The simulation plane is the one depicted in Fig. 6.11. The laser is p-polarized and propagates along the z-axis. Enlarged views of the fields E_y^2 (a) and ρ_e (b) are shown. The time is $t = 146\,\mathrm{fs}$. The color-bars show the selected data range for each plot, while the maximum and minimum values of the fields are printed in the top left corner of the plots. The units are $E_0 = 6.13 \cdot 10^{12}\,\mathrm{V/m}$ and $\rho_0 = 3.41 \cdot 10^8\,\mathrm{As/m^3}$.

While the nonlinear 1D laser-plasma interaction can be described by a simple model that yields all the relevant absorption mechanisms the same does not hold for intense laser-plasma interaction in 2D due to the violation of lateral momentum conservation.

6.3.1 A kinetic model for sharp edged plasma

We derive nonlinear equations for laser-plasma interaction which are able to describe absorption in a self-consistent way. Use is made of the well-known boosting technique [121] which yields a constant of motion. The boosted frame will be used here. For the initial electron distribution a Maxwellian is taken. We assume that the ionic plasma vacuum interface can be approximated by a step-like density profile with $n_i(z) = n_0$ for $z > 0$. This assumption simplifies the following analysis but is rather irrelevant for the discussion that follows. The ions are taken to be immobile. The electrons are allowed to penetrate into the vacuum. We obtain for the electron distribution

$$\begin{aligned} f(t) &= \frac{n_0}{\sqrt{2\pi}^3 m^3 v_{th}^3} \exp\left(-\frac{p_x^2(0)+p_z^2(0)}{2m^2v_{th}^2}\right) \\ &\quad \exp\left(-\frac{(p_y(0)+\bar\beta\bar\gamma mc)^2}{2\bar\gamma^2 m^2 v_{th}^2}\right) , \end{aligned} \tag{6.108}$$

where

$$z(\tau) = z - \int_\tau^t d\eta\; v_z(\eta) \;, \tag{6.109}$$

$$p_x(\tau) = p_x \;, \tag{6.110}$$

$$p_y(\tau) = p_y + e\left[A_y(z(\tau),\tau) - A_y(z,t)\right] \;, \tag{6.111}$$

$$p_z(\tau) = p_z + e\int_\tau^t d\eta\; \left[E_z(z(\eta),\eta) + v_y(\eta)\;\partial_z A_y(z(\eta),\eta)\right] \tag{6.112}$$

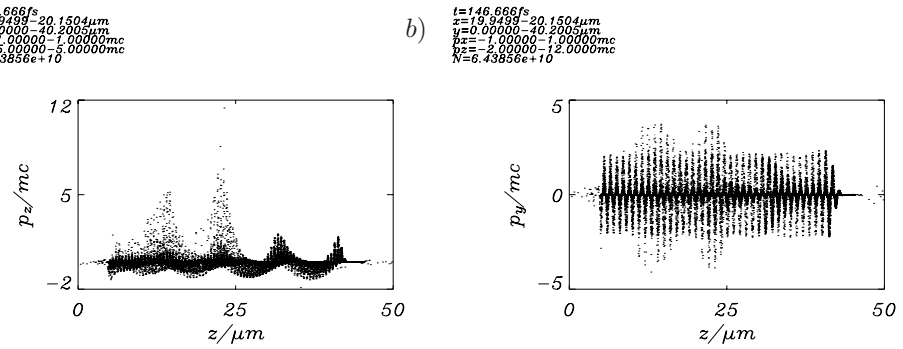

Figure 6.18: Electron phase space for the self-modulated laser beam simulation. The simulation plane is the one depicted in Fig. 6.15. The laser is p-polarized and propagates along the z-axis. The figure shows (a) the zp_z- and (b) the zp_y-projections of the electron phase space after $t = 146\,\mathrm{fs}$. The momenta are normalized in units $m_e c$. In the top left corner of each plot the sampling range in phase space for the electrons has been printed.

and

$$v_z(\tau) \approx \frac{p_z(\tau)}{m\bar{\gamma}}\,, \qquad v_y(\tau) \approx -c\bar{\beta} + \frac{p_y(\tau) + \bar{\beta}\bar{\gamma}mc}{m\bar{\gamma}^3}\,, \tag{6.113}$$

where $E_y = -\partial_t A_y$ and $B_x = -\partial_z A_y$. The longitudinal and transverse electromagnetic fields E_y, E_z, and B_x are obtained from Maxwell equations

$$\partial_z E_z = \frac{1}{\epsilon_0}\rho\,, \tag{6.114}$$

$$\partial_t E_z = -\frac{1}{\epsilon_0} j_z\,, \tag{6.115}$$

$$\partial_z E_y = \partial_t B_x\,, \tag{6.116}$$

$$\partial_t E_y = c^2 \partial_z B_x - \frac{1}{\epsilon_0} j_y\,. \tag{6.117}$$

The quantities $\bar{\beta}$ and $\bar{\gamma}$ are given by $\bar{\beta} = \sin\theta$ and $\bar{\gamma} = 1/\sqrt{1-\bar{\beta}^2}$ where θ denotes the angle of incidence. We next insert Equations (6.109), (6.110), (6.111), (6.112) and (6.113) into Equation (6.108). Assuming that $A_y(z,0)$ disappears for $z > 0$ we obtain for the electron charge density ρ_e and the electron current densities j_{ye} and j_{ze}

$$\rho_e = -\frac{en_0}{2\pi m^2 v_{th}^2} \int_{-\infty}^{\infty} dp_y dp_z \, \exp\left[-\frac{p_y^2}{2\bar{\gamma}^2 m^2 v_{th}^2}\right] \times \exp\left[-\frac{1}{2m^2 v_{th}^2}\left(p_z + e\int_0^t d\tau\,\left\{E_z^L + \frac{(p_y + eA_y)}{m\bar{\gamma}^3}\,\partial_z A_y\right\}\right)^2\right]\,, \tag{6.118}$$

$$j_{ye} = -\frac{en_0}{2\pi m^2 v_{th}^2} \int_{-\infty}^{\infty} dp_y dp_z \left(-\bar{\beta}c + \frac{p_y + eA_y(t)}{m\bar{\gamma}^3}\right) \exp\left[-\frac{p_y^2}{2\bar{\gamma}^2 m^2 v_{th}^2}\right] \tag{6.119}$$

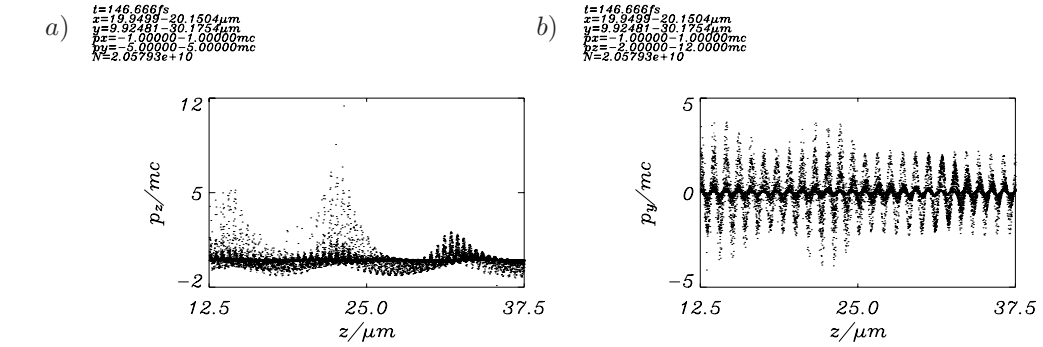

Figure 6.19: Electron phase space for the self-modulated laser beam simulation. The simulation plane is the one depicted in Fig. 6.15. The laser is p-polarized and propagates along the z-axis. The figure shows enlarged views of (a) the zp_z- and (b) the zp_y-projections of the electron phase space after $t = 146\,\mathrm{fs}$. The momenta are normalized in units $m_e c$. In the top left corner of each plot the sampling range in phase space for the electrons has been printed.

$$\times \exp\left[-\frac{1}{2m^2v_{th}^2}\,\left(p_z + e\int_0^t d\tau\,\left\{E_z^L + \frac{(p_y+eA_y)}{m\bar{\gamma}^3}\,\partial_z A_y\right\}\right)^2\right]\,,$$

$$\begin{aligned} j_{ze} &= -\frac{en_0}{2\pi m^2 v_{th}^2}\,\int_{-\infty}^{\infty} dp_y dp_z\,\frac{p_z}{m\bar{\gamma}}\,\exp\left[-\frac{p_y^2}{2\bar{\gamma}^2 m^2 v_{th}^2}\right] \qquad (6.120)\\ &\quad\times\exp\left[-\frac{1}{2m^2v_{th}^2}\,\left(p_z + e\int_0^t d\tau\,\left\{E_z^L + \frac{(p_y+eA_y)}{m\bar{\gamma}^3}\,\partial_z A_y\right\}\right)^2\right]\,, \end{aligned}$$

where $E_z^L = E_z + \bar{\beta}c\partial_z A_y$ and $A_y(t) = A_y(z,t)$. From Equations (6.118), (6.119), and (6.120) we find after calculating the total charge and current densities $\rho = \rho_e + \rho_i$, $j_y = j_{ye} + j_{yi}$, and $j_z = j_{ze} + j_{zi}$ and using Maxwell equations

$$\partial_z E_z = \frac{1}{\epsilon_0}\,\rho\,, \qquad (6.121)$$

$$\left(\partial_z^2 - \frac{1}{c^2}\partial_t^2\right) A_y = \frac{\omega_p^2}{c^2\bar{\gamma}^2}\mathcal{A}_y + \frac{1}{\epsilon_0 c^2}\,\rho\,\left(\bar{\beta}c - \frac{e}{m\bar{\gamma}^3}A_y\right)\,, \qquad (6.122)$$

where

$$\begin{aligned} \mathcal{A} &= A_y + \frac{1}{2\pi e\bar{\gamma}m^2v_{th}^2}\,\int_{-\infty}^{\infty} dp_y dp_z\,p_y\,\exp\left[-\frac{p_y^2}{2\bar{\gamma}^2m^2v_{th}^2}\right] \qquad (6.123)\\ &\quad\times\exp\left[-\frac{1}{2m^2v_{th}^2}\,\left(p_z + e\int_0^t d\tau\,\left\{E_z^L + \frac{(p_y+eA_y)}{m\bar{\gamma}^3}\,\partial_z A_y\right\}\right)^2\right]\,,\\ \rho &= e\bar{\gamma}n_0 - \frac{en_0}{2\pi m^2v_{th}^2}\,\int_{-\infty}^{\infty} dp_y dp_z\,\exp\left[-\frac{p_y^2}{2\bar{\gamma}^2m^2v_{th}^2}\right] \qquad (6.124) \end{aligned}$$

$$\times \exp\left[-\frac{1}{2m^2v_{th}^2}\ \left(p_z + e\int_0^t d\tau\ \left\{E_z^L + \frac{(p_y+eA_y)}{m\bar{\gamma}^3}\ \partial_z A_y\right\}\right)^2\right]\ ,$$

and $\omega_p^2 = e^2 n_0/\epsilon_0 m$. The second term on the right of Equation (6.123) disappears for small lateral temperatures. We now proceed by rewriting (6.123) and (6.124)

$$\begin{aligned}
\mathcal{A} &= A_y + \frac{1}{2\pi e\bar{\gamma}m^2v_{th}^2}\ \int_{-\infty}^{\infty} dp_y dp_z\ p_y\ \exp\left[-\frac{p_y^2}{2\bar{\gamma}^2m^2v_{th}^2}\right] \qquad (6.125)\\
&\quad \times \exp\left[-\frac{(p_z+G+p_yF)^2}{2m^2v_{th}^2}\right]\ ,\\
\rho &= e\bar{\gamma}n_0 - \frac{en_0}{2\pi m^2v_{th}^2}\ \int_{-\infty}^{\infty} dp_y dp_z\ \exp\left[-\frac{p_y^2}{2\bar{\gamma}^2m^2v_{th}^2}\right] \qquad (6.126)\\
&\quad \times \exp\left[-\frac{(p_z+G+p_yF)^2}{2m^2v_{th}^2}\right]\ ,
\end{aligned}$$

where

$$\begin{aligned}
G &= e\int_0^t d\tau\ \left\{E_z^L + \frac{eA_y\partial_z A_y}{m\bar{\gamma}^3}\right\}\ , \qquad (6.127)\\
F &= e\int_0^t d\tau\ \frac{\partial_z A_y}{m\bar{\gamma}^3}\ . \qquad (6.128)
\end{aligned}$$

At this point Equations (6.127) and (6.128) depend on p_z through the velocity v_z in Equation (6.109). But they do not depend on p_y. Performing the p_y-integration yields

$$\begin{aligned}
\mathcal{A} &= A_y - \frac{\bar{\gamma}^2}{\sqrt{2\pi}emv_{th}}\ \int_{-\infty}^{\infty} dp_z\ \frac{(p_z+G)\,F}{\sqrt{1+\bar{\gamma}^2F^2}^3} \qquad (6.129)\\
&\quad \times \exp\left[-\frac{(p_z+G)^2}{2m^2v_{th}^2(1+\bar{\gamma}^2F^2)}\right]\ ,\\
\rho &= e\bar{\gamma}n_0 - \frac{e\bar{\gamma}n_0}{\sqrt{2\pi}mv_{th}}\ \int_{-\infty}^{\infty} dp_z\ \frac{1}{\sqrt{1+\bar{\gamma}^2F^2}} \qquad (6.130)\\
&\quad \times \exp\left[-\frac{(p_z+G)^2}{2m^2v_{th}^2(1+\bar{\gamma}^2F^2)}\right]\ .
\end{aligned}$$

We may now investigate the case for which the kinetic fluid is hot ($v_{th} \to \infty$). This means that we may expand the exponential functions in (6.129) and (6.130). We obtain

$$\begin{aligned}
\mathcal{A}_y &\approx A_y - \frac{\bar{\gamma}^2}{\sqrt{2\pi}emv_{th}}\int_{-\infty}^{\infty} dp_z\ p_z\ e^{-\frac{p_z^2}{2m^2v_{th}^2}}\ F\ , \qquad (6.131)\\
\rho &\approx \frac{\epsilon_0\omega_p^2\bar{\gamma}}{\sqrt{2\pi}em^2v_{th}^3}\ \int_{-\infty}^{\infty} dp_z\ p_z\ e^{-\frac{p_z^2}{2m^2v_{th}^2}}\ G\ . \qquad (6.132)
\end{aligned}$$

With the help of (6.121) and (6.122) we find for the field equations

$$\partial_z E_z = \frac{\omega_p^2\bar{\gamma}}{\sqrt{2\pi}em^2v_{th}^3}\ \int_{-\infty}^{\infty} dp_z\ p_z\ e^{-\frac{p_z^2}{2m^2v_{th}^2}}\ G\ , \qquad (6.133)$$

$$\left(\partial_z^2 - \frac{1}{c^2}\partial_t^2\right) A_y = \frac{\omega_p^2}{c^2\bar{\gamma}^2}\left(1 - \frac{1}{\sqrt{2\pi}m^3 v_{th}^3}\int_{-\infty}^{\infty} dp_z\, p_z\, e^{-\frac{p_z^2}{2m^2 v_{th}^2}}\, G\right) A_y \quad (6.134)$$
$$+\frac{\omega_p^2}{c^2\bar{\gamma}^2}\,\frac{c\bar{\beta}\bar{\gamma}^3}{\sqrt{2\pi}em^2 v_{th}^3}\int_{-\infty}^{\infty} dp_z\, p_z\, e^{-\frac{p_z^2}{2m^2 v_{th}^2}}\, G$$
$$+\frac{\omega_p^2}{c^2\bar{\gamma}^2}\,\frac{\bar{\gamma}^2}{\sqrt{2\pi}emv_{th}}\int_{-\infty}^{\infty} dp_z\, p_z\, e^{-\frac{p_z^2}{2m^2 v_{th}^2}}\, F\,.$$

Neglecting the nonlinear source terms on the right side of (6.134) Fresnel-like angular scaling of absorption is obtained [118]. In this case the second line of (6.134) represents the contribution to linear Brunel heating while the last line and A_y from the first line give the contribution of the anomalous skin effect to absorption. Linearizing of particle trajectories, assuming small electron displacements and stationary conditions, and neglecting the light pressure allows us to approximate (6.127) as

$$G \approx \frac{ev_z}{\omega^2}\, e^{i\omega t}\, \partial_z E_z^L\,. \quad (6.135)$$

Expression (6.135) is substituted for G in the first line of (6.134). With the help of G the charge density (6.132) can be calculated

$$\rho \approx \frac{\epsilon_0\omega_p^2}{\omega^2}\, e^{i\omega t}\, \partial_z E_z^L\,. \quad (6.136)$$

The same expression can be obtained from a fluid model as is shown in the next section.

6.3.2 A fluid model for sharp edged plasma

Equations (6.133) and (6.134) indicate that fluid-like behavior and kinetic effects determine laser absorption in the plasma for oblique incidence. To see this we may first derive an equation similar to Equation (6.122) from a fluid model. We keep ions fixed and write for electron mass and momentum balance neglecting thermal pressure

$$\partial_t n_e + \partial_z\left(u_{ze}\, n_e\right) = 0\,, \quad (6.137)$$
$$\partial_t p_{ze} + u_{ze}\,\partial_z p_{ze} = -e\,\left(E_z + u_{ye}\,\partial_z A_y\right)\,, \quad (6.138)$$
$$\frac{d}{dt}\left(p_{ye} - eA_y\right) = 0\,, \quad (6.139)$$

where

$$u_{ze} \approx \frac{p_{ze}}{m\bar{\gamma}}\,, \quad (6.140)$$
$$u_{ye} \approx -c\bar{\beta} + \frac{p_{ye} + \bar{\beta}\bar{\gamma}mc}{m\bar{\gamma}^3} \quad (6.141)$$

and

$$\rho = -e\bar{\gamma}n_e + e\bar{\gamma}n_0\,, \quad (6.142)$$
$$j_y = -e\bar{\gamma}n_e\, u_{ye} - e\bar{\gamma}n_0\,\bar{\beta}c\,. \quad (6.143)$$

It is easy to integrate Equation (6.139). The charge density is obtained from (6.137) and (6.138). We find with the help of perturbation analysis from (6.137), (6.138), and (6.139)

in the stationary limit

$$n_e \approx -\frac{n_0}{i\omega}\, e^{i\omega t}\, \partial_z u_{ze} \,, \tag{6.144}$$

$$p_{ze} \approx -\frac{e}{i\omega}\, e^{i\omega t}\, E_z^L \,. \tag{6.145}$$

For the linearized charge density the fluid model yields the same expression as the kinetic approach

$$\rho \approx \frac{\epsilon_0 \omega_p^2}{\omega^2}\, e^{i\omega t}\, \partial_z E_z^L \,. \tag{6.146}$$

Both, the fluid model and the kinetic approach show that oscillations of the critical interface are present. Finally, the Maxwell equations for the fluid model read

$$\partial_z E_z = \frac{1}{\epsilon_0}\, \rho \,, \tag{6.147}$$

$$\left(\partial_z^2 - \frac{1}{c^2}\partial_t^2\right) A_y = \frac{\omega_p^2}{c^2 \bar{\gamma}^2} A_y + \frac{1}{\epsilon_0 c^2}\, \rho\, \left(\bar{\beta} c - \frac{e}{m\bar{\gamma}^3} A_y\right) \,. \tag{6.148}$$

6.3.3 Simulation of laser-matter interaction under oblique incidence

In this subsection we present a simulation of laser beam absorption in a sharp-edged plasma with the PSC in 2D under oblique incidence. The laser beam is reflected specularly at the critical plasma density as is predicted by the theory outlined in subsection 6.3.1. The plasma we consider consists of electrons and ions. The peak electron plasma density is highly overcritical. This means that $\omega \ll \omega_{pe}$ holds. For the ion background we take particles that have the mass of aluminum and an average charge of $Z = 10$. Since now the plasma density is high and the average ion charge is $Z = 10$, we cannot neglect collisions. Hence, the collision module **PIC_bin_coll.f** has been turned on in **VLI.f** and **VLA.f**.

We begin by describing the setup of the simulation. Figure 6.20 depicts the simulation box, which we have selected for the simulation. A Cartesian right-handed coordinate system has been attached to the box, the origin of which is denoted by $(0, 0, 0)$. The same coordinate system is used in the PSC. The simulation box is 3D. However, we only select a 2D simulation plane depicted by the shaded area in the figure. The sector shaded in dark represents the plasma. The size of the simulation box is set up in **INIT_param.f**. We select a 3D simulation box of $100\,\mu\text{m} \times 100\,\mu\text{m} \times 100\,\mu\text{m}$. This is done by setting $lengthx = 100\,\mu$m, $lengthy = 100\,\mu$m, and $lengthz = 100\,\mu$m. The number of grid points of the spatial grid is $2000 \times 2000 \times 2000$. This grid size is established by setting $i1tot = 2000$, $i2tot = 2000$, and $i3tot = 2000$. For the 2D plane in Fig. 6.11, however, only 2000×2000 cells are used by assigning $i1n = 999$, $i1x = 999$, $i2n = 0$, $i2x = 1999$, $i3n = 0$, and $i3x = 1999$. The plasma density required for normalization in the PSC (see subsection 4.1) is determined by $n0$. We set $n0 = 5 \cdot 10^{27}\,\text{m}^{-3}$. The electric field strength $e0$ (see subsection 4.1) is obtained with the help of the laser intensity $i0$. We choose $i0 = 5.0 \cdot 10^{22}\,\text{Wm}^{-2}$. The laser frequency wl is determined with the help of the laser wavelength lw. We take $lw = 10^{-6}\,$m. We select periodic boundaries for the Maxwell fields and the quasi-particles along the x-direction. At $y = 0$, $y = 100\,\mu$m, $z = 0$, and $z = 100\,\mu$m we choose radiating boundaries for the fields and periodic ones for the particles. We place no laser beam at $y = 0$, $y = 100\,\mu$m, and $z = 100\,\mu$m. We select reflecting boundaries for the particles at $z = 0$ and $z = 100\,\mu$m. Under this condition radiation from inside the simulation box can escape for the given setup. The boundary conditions are set up by selecting $boundary\_field\_x = 1$,

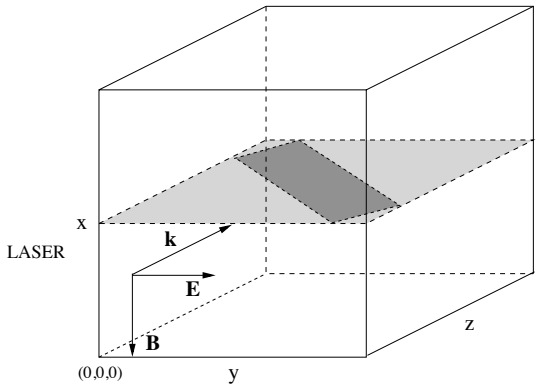

Figure 6.20: Laser beam interacting with plasma in 2D. The figure shows the simulation box that harbors the simulation plane in 2D. The box defines a coordinate system, the origin of which is at $(0,0,0)$. The direction of the incident laser pulse is along the z-axis. The reflected laser beam propagates along the y-axis. The incident beams is indicated by $\vec{k}$. The laser field polarization is depicted by $\vec{E}$. Since the electric field is parallel to the simulation plane the laser pulse is called p-polarized.

$boundary\_field\_y = 0$, $boundary\_field\_z = 0$, $boundary\_part\_x = 1$, $boundary\_part\_y = 1$, and $bounday\_part\_z = 0$. We choose to decompose the simulation domain along the y-axis and to carry the simulation out on 8 nodes. This implies $xnpe = 1$, $ynpe = 8$, and $znpe = 1$. The filesystems selected for the data output and check-pointing data are the ones from which the simulation is started. This means $data\_out =$ "./" and $data\_chk =$ "./". The maximum permissible CPU time for a single run is set with the help of the parameter $cpum$. We choose $cpum = 6000$, which means 6000 sec. After 6000 sec the PSC check-points its data core and restarts the simulation from the latter. The maximum permissible number of time steps is given by $nmax$. We select $nmax = 5000$. The parameters for data output control have been adjusted such that output for the time resolved fields and particles is generated every four full laser cycles, which means after $np = 4\,nnp$ time steps, where nnp is the number of time steps for a full laser cycle. Every particle is recorded after np time steps. The relevant settings are $nprf = 0$, $dnprf = np$, $nprc = 0$, $dnprc = np$, $nprparti = 0$, $dnprparti = np$, $nistep = 1$. Time-averaging is repeatedly done over a full laser cycle. The required settings are $tmnvf = 1$, $tmxvf = nnp$, $tmnvp = 1$, and $tmxvp = nnp$. While $n0$ sets the density for the normalization in the PSC, the file **INIT_den.f** is required to determine the shape and location of the plasma in the simulation box. The coordinate system used for setting up the density is the same as the one that defines the simulation box. The origin of the coordinate system is $(0,0,0)$. The default density function provided with the PSC makes use of nine parameters. They are explained in subsection 5.1. For the absorption simulation we choose $x0 = 5 \cdot 10^{-5}$ m, $y0 = 5.335 \cdot 10^{-5}$ m, and $z0 = 5.335 \cdot 10^{-5}$ m. In addition, we rotate the density function by 45° by setting the parameter $rot = 45$. For the gradient lengths at the plasma boundaries we use $Lx = 5 \cdot 10^{-8}$ m, $Ly = 5 \cdot 10^{-8}$ m, and $Lz = 5 \cdot 10^{-8}$ m. The width of the plasma is given by $widthx = 10^{-4}$ m, $widthy = 4.5 \cdot 10^{-5}$ m, and $widthz = 5 \cdot 10^{-6}$ m. The initial location, direction, and polarization of the laser pulse is set with the help of twelve files. Details are listed in subsection 5.1. The laser pulse is assumed to propagate along the z-axis and to be p-polarized, which means that the electric field vector of the laser oscillates in the simulation plane depicted in Fig. 6.20. Hence, we turn off all antennas

except **INIT_ppulse_z1.f**, which irradiates the plasma through the surface at $z = 0$ along z. The coordinate frame for the laser pulse is the same as the one for the simulation box. The default initial shape of the laser pulse in space shipped with the PSC is a Gaussian. We choose a rise length of $1\,\mu$m at full-width-half-maximum (FWHM), after which the intensity remains constant, in propagation direction. The widths in lateral directions are $5\,\mu$m. At startup time the laser pulse is placed at $(50\,\mu\text{m}, 50\,\mu\text{m}, -2\,\mu\text{m})$, which is the center of the xy-plane $2\,\mu$m in front of the simulation box. This means $xm = 5 \cdot 10^{-5}\,$m, $ym = 5 \cdot 10^{-5}\,$m, and $zm = -2 \cdot 10^{-6}\,$m. The laser pulse widths are $dxm = 5 \cdot 10^{-6}\,$m, $dym = 5 \cdot 10^{-6}\,$m, and $dzm = 10^{-6}\,$m. The distribution functions are set up with the help of the file **INIT_idistr.f**. We choose to perform the simulation for electrons and ions with $m_i = 27\,m_p$ and $Z = 10$. We take 10 particles per cell for the electrons and 1 particle per cell for the ions. This means that we set $nicell = 10$. Further setup details are found in the file **INIT_idistr.f**. Since we deal with electrons and ions we have two entries for particle properties, one for electrons and one for ions. For the electron charge we choose $q_e = -1.6 \cdot 10^{-19}\,$As, for the electrons mass $m_e = 9.1 \cdot 10^{-31}\,$kg, and for the electron temperature $T_e = 0.1\,$keV. This means $qni = -1.0$, $mni = 1.0$, and $tni = 0.1$. For the ions we set $qni = 10.0$, $mni = 27 \cdot 1836$, and $tni = 0.1$. In case **OpenPBS** is available (see subsection 5.1.6) the scripts **vliexec** to **IDLATOM** have to be adapted to the local computing environment (see subsection 5.1). It is further necessary to adapt the IDL files shipped with the PSC in case the intent is to use them (see subsection 5.1.5). The post-processors **PROCESSOR_pfield** to **PROCESSOR_atom** require no adaptions.

We continue by describing the simulation results. During runtime the PSC records diagnostic data in the file **VLA.data**, that can be used to trace possible irregularities. The file contains most setup parameters and the wall clock time for each timestep. The file shows that 4000000 cells and $3.96 \cdot 10^6$ quasi-particles have been allocated for the simulation. The required memory is about 640 MByte per node. The run takes about 14 sec of wall clock time per time step. Plot (a) of Fig. 6.21 shows the time-averaged incident and reflected transverse electric fields and the time-averaged magnetic field. The electron density has been inserted into plot (a) for clarity. From comparison of the intensities of the incident and reflected laser beams it can be inferred that significant laser absorption in the target takes place. The same conclusion can be drawn from the degree of electron heating that is observed in Fig. 6.24. Plot (b) of Fig. 6.22 shows that the laser radiation is capable of driving electrons across the plasma vacuum boundary as has been predicted in subsection 6.3.1. The latter electrons resonate in the electric potential present at the vacuum-plasma interface, gain energy and escape. In the plasma they undergo collisional interaction with the plasma background. It is interesting to observe that holes in the electron density can form, which contain electric field energy. Plots (a) and (b) of Fig. 6.23 show this phenomenon.

Looking into the electron phase space generated by the laser beam we find that strong electron heating takes place. Plots (a) and (b) of Fig. 6.24 show the electron energy distribution at $t = 239\,$fs and $t = 426\,$fs. It is evident that the electrons heat up rapidly adopting a Maxwellian, that is distorted in forward direction. The distortion is due to the acceleration of electrons in the laser field.

6.3.4 Absorption at high laser intensities

We are now able to understand some intensity dependent trends of absorption. First we find from Equation (6.114) the general property

$$\partial_t E_z = -\frac{1}{\epsilon_0}\, j_z \qquad \rightarrow \qquad \frac{1}{2}\,\partial_t E_z^2 = -\frac{1}{\epsilon_0}\, j_z E_z\ . \tag{6.149}$$

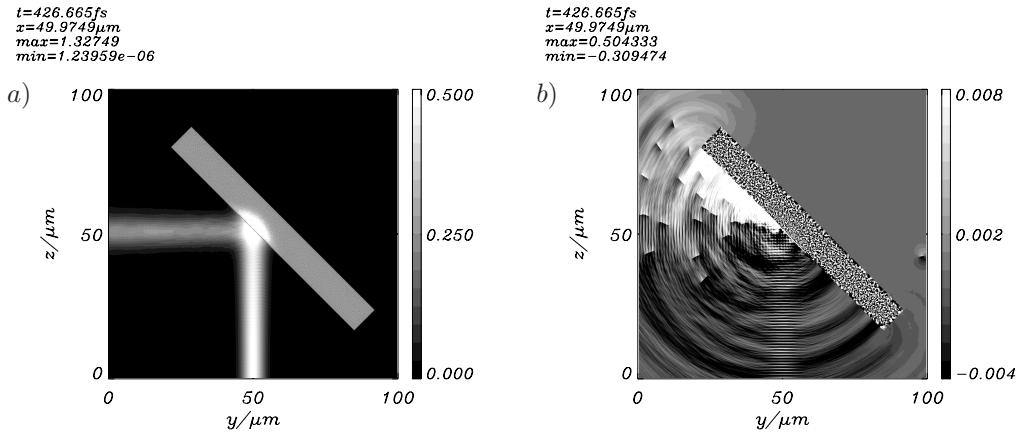

Figure 6.21: Time-averaged incident and reflected laser beam and magnetic field for the absorption simulation. The simulation plane is the one depicted in Fig. 6.20. The laser beam is p-polarized and propagates along the z-axis. The figure shows (a) the time-averaged radiation field $E_y^2 + E_z^2$ and (b) the time-averaged magnetic field B_x after $t = 426\,\mathrm{fs}$. The units are $E_0 = 6.13 \cdot 10^{12}\,\mathrm{V/m}$ and $B_0 = 2.0 \cdot 10^4\,\mathrm{Vs/m^2}$. In the top left corner of each plot further information is given. It is interesting to observe that the laser radiation is capable of scattering electrons into the vacuum as plot (b) shows.

In the stationary limit this yields after time-averaging $\langle j_z E_z \rangle = 0$. Hence, absorption can only be due to $\langle j_y E_y \rangle$ and the degree of de-phasing between lateral current j_y and lateral field A_y determines energy deposition in the plasma. Taking nonlinearities into account Equation (6.134) shows that the rising amplitude of E_z^L enhances the electron density in the skin layer where the laser field A_y is present for finite angles of incidence. The fields E_z^L and A_y are coupled. Hence, it is likely that enhanced de-phasing between current j_y and field A_y is obtained. This situation is present during the first half-cycle and disappears during the next. However, the plasma interface oscillations just described may contribute to the cycle-averaged energy deposition in the plasma and enhances the latter beyond values obtained from linear theory. However, with increasing laser intensity the radiation pressure contribution to G in (6.127) dominates. Unlike the field E_z^L the radiation pressure suppresses electron penetration into the vacuum by plasma density gradient steepening. Hence, fractional absorption may drop as observed in [58]. The boosted model described in this section shows that in 1D the radiation pressure can compensate the electric field that drives plasma surface oscillations. Due to the curvature of the deformed targets considered in this chapter the same conclusions do not hold in 2D.

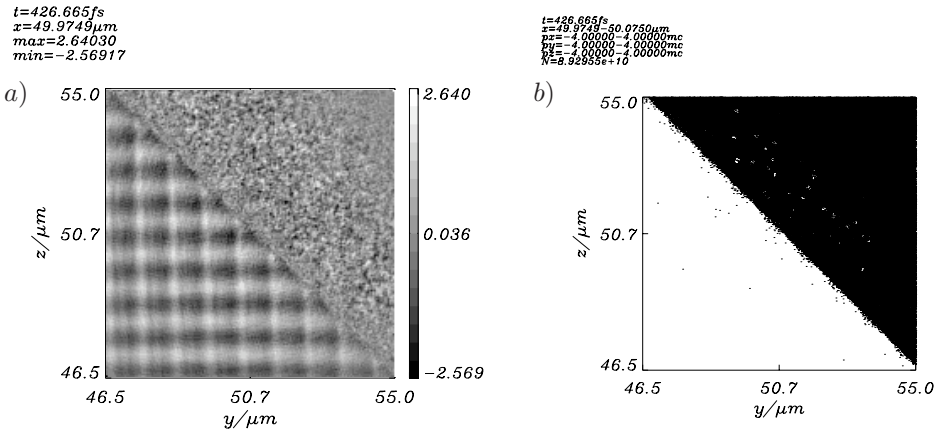

Figure 6.22: Electric field and the yz-projection of the electron phase space for the absorption simulation. The simulation plane is the one depicted in Fig. 6.20. The laser beam is p-polarized and propagates along the z-axis. Plot (a) shows the electric field $E_y + E_z$ and plot (b) the yz-projection of the electron phase space after $t = 426\,\mathrm{fs}$. The electric field is given in units of $E_0 = 6.13 \cdot 10^{12}\,\mathrm{V/m}$. In the top left corner of each plot further information is given. Plot (b) shows that electrons oscillate into the vacuum region in front of the target where the driving electric field is strong.

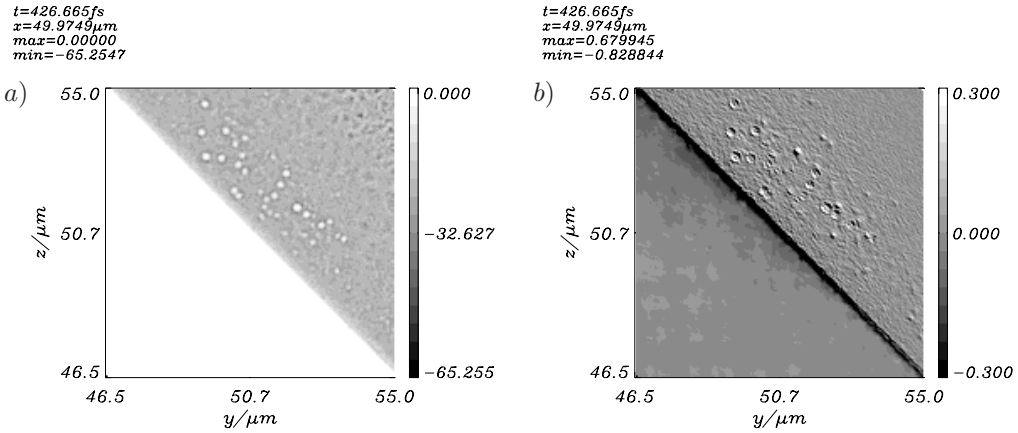

Figure 6.23: Time-averaged electron density and electric field for the absorption simulation. The simulation plane is the one depicted in Fig. 6.20. The laser beam is p-polarized and propagates along the z-axis. The figure shows (a) the time-averaged electron density and (b) the time-averaged electric field $E_y + E_z$ after $t = 426\,\mathrm{fs}$. The units are $n_0 = 2.13 \cdot 10^{27}\,\mathrm{m}^{-3}$ and $E_0 = 6.13 \cdot 10^{12}\,\mathrm{V/m}$. In the top left corner of each plot further information is given. Plots (a) and (b) show that there are holes in the electron density filled with radiation.

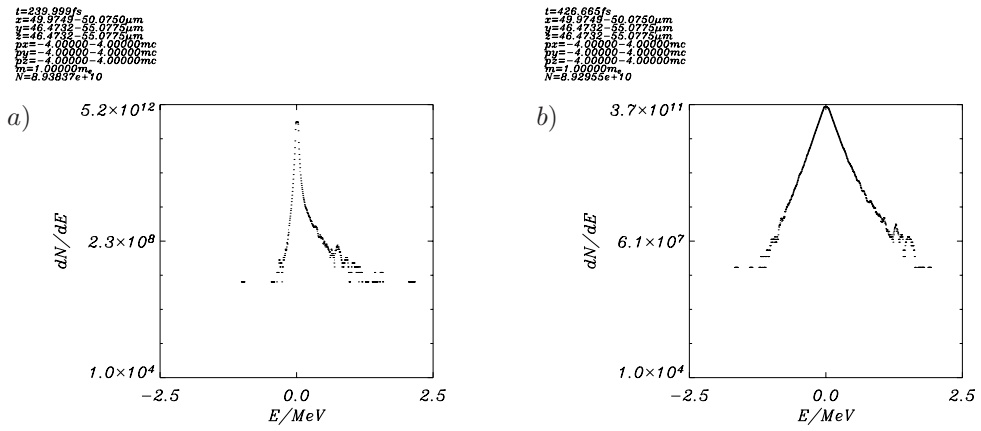

Figure 6.24: Electron energy distribution for the absorption simulation. The simulation plane is the one depicted in Fig. 6.20. The laser beam is p-polarized and propagates along the z-axis. Plot (a) shows the electron energy distribution at $t = 239\,\mathrm{fs}$ and plot (b) shows the same at $t = 426\,\mathrm{fs}$. In the top left corner of each plot further information is given. Plots (a) and (b) show that the laser radiation strongly heats the electrons.

Chapter 7

Summary

In section 3 the basic equations required to describe the physics of intense laser-plasma interaction have been introduced. They are Maxwell's equations and the relativistic Vlasov-Boltzmann equations.

In section 4 the numerical methods applied to solve the equations outlined in section 3 have been described. They comprise the FDTD scheme for solving Maxwell's equations, the Particle-In-Cell (PIC) method, which is a quasi-particle method, for solving the Vlasov-Boltzmann equations, and finally a Monte Carlo method first introduced by Takizuka [74], that reduces the solution of the equations of motion with collisions for the quasi-particles to a problem that scales like N, where N is the number of quasi-elements in the simulation. The methods described are the ones employed in the PSC code, which is available as open source software at http://www.THE-PSC.com.

In section 5 the structure and modules of the PSC code have been described. It has been explained which modules are required for solving Maxwell's equations, the Vlasov equations, and the Vlasov-Boltzmann equation. The boundary conditions implemented in the PSC have been explained. Various scripts shipped with the PSC have been described. Furthermore, the section gives a brief introduction into the usage of the graphics back-end of the PSC.

In section 6 a brief discussion of nonlinear aspects of intense laser pulse propagation through plasma has been given. Envelope equations based on the par-axial approximation for the wave equation in under-dense, cold plasma have been derived. With the help of the latter basic insight into important nonlinear phenomena like pulse diffraction, relativistic pulse self-focusing, and channeling of the laser beam has been obtained. Simulation performed with the PSC code have been presented in the text. The setup files for the simulations can be downloaded at http://www.THE-PSC.com. A simple expansion of the fluid flow up to the fourth order in the normalized quiver velocity has allowed an analytical description of electric and magnetic wake-fields. Wake field simulations have been presented. A set of integro-differential equations for laser absorption in sharp edged plasma has been given. The model explains the kinetic as well as the collective mechanisms that contribute to laser light absorption. Simulations with the PSC have been performed to illustrate the sharp-edged laser-plasma interaction phenomena.

Chapter 8

The open source project PSC

The Plasma Simulation Code (PSC) is developed as an open source software. It is the intent of the project to provide a state of the art simulation code for education and research in the field of intense laser-matter interaction. The code is developed by scientists in the field. It is updated on a regular basis to take account of recent developments in the field.

The current release of the PSC is available at http://www.THE-PSC.com. Details of the project, the setup of the PSC for the examples discussed in this chapter, new physics modules, terms and conditions of usage, and a complete list of publications achieved with the help of the code are explained and presented on the project web-site.

Chapter 9

License agreement

The PSC is released under the general terms and conditions of the GNU public license with the following restrictions:

- Proliferation of the PSC is inhibited without the prior consent of the authors of the code.
- Usage of the PSC has to be acknowledged in publications whenever use of the code has been made.

Bibliography

[1] G. A. Mourou, C. P. J. Barty, M. D. Perry, *Ultrahigh-intensity lasers: physics of the extreme on a tabletop*, Physics Today, 22 (Jan. 1998).

[2] D. Strickland and G. A. Mourou, *Compression of amplified chirped optical pulses*, Optics Comm. **56**, 216 (1985).

[3] M. D. Perry and G. A. Mourou, *Terawatt to Petawatt Subpicosecond lasers*, Science **264**, 917 (1994).

[4] C. J. Joshi and P. B. Corkum, *Interactions of ultra-intense laser light with matter*, Physics Today, 36 (Jan. 1995).

[5] S. Augst, D. Strickland, D. D. Meyerhofer, S. L. Chin, and J. H. Eberly, *Tunneling ionization of noble gases in a high-intensity laser field*, Phys. Rev. Lett. **63**, 2212 (1989).

[6] W. Lotz, *Electron-Impact Ionization Cross-Sections and Ionization Rate Coefficients for Atoms and Ions from Hydrogen to Calcium*, Z. Physik **216**, 241 (1968).

[7] L. Spitzer, *Physics of fully ionized gases*, Wiley, New York (1962).

[8] S. I. Braginskii, *Transport processes in a plasma*, Review of Plasma Physics **1**, 205 (1965).

[9] H. Ruhl, A. Macchi, P. Mulser, F. Cornolti, and S. Hain, *Collective dynamics and enhancement of absorption in deformed targets*, Phys. Rev. Lett. **82**, 2095 (1999).

[10] H. Ruhl, Y. Sentoku, K. Mima, K.A. Tanaka, and R. Kodama, *Collimated electron jets by intense laser beam-plasma surface interaction under oblique incidence*, Phys. Rev. Lett. **82**, 743 (1999).

[11] S. Bastiani, A. Rousse, J.P. Geindre, P. Audebert, C. Quoix, G. Hamoniaux, A. Antonetti, and J. -C. Gauthier, *Eperimental study of the interaction of subpicosecond laser pulses with solid targets of varying initial scale lengths*, Phys. Rev. **E 56**, 7179 (1997).

[12] Barbara F. Lasinski, A. Bruce Langdon, Stephen P. Hatchett, Michael H. Key, and Max Tabak, *Particle-in-cell simulations of ultra intense laser pulses propagating through overdense plasma for fast-ignitor and radiography applications*, Phys. Plasmas **6**, 2041 (1999).

[13] J. R. Davis, A. R. Bell, and M. Tatarakis, *Magnetic focusing and trapping of high-intensity laser-generated fast electrons at the rear of solid targets*, Phys. Rev. E **59**, 6032 (1999).

[14] A. R. Bell, J. R. Davis, S. Guerin, and H. Ruhl, *Fast electron transport in high intensity short pulse laser-solid experiments*, Plasma Phys. Control. Fusion **39**, 653 (1997).

[15] T. Tajima and J. M. Dawson, *Laser Electron Accelerator*, Phys. Rev. Lett. **43**, 267 (1979).

[16] T. Ditmire, J. W. G. Tisch, E. Springate, M. B. Mason, N. Hay, R. A. Smith, J. Marangos, and M. H. R. Hutchinson, *High-energy ions produced in explosions of superheated atomic clusters*, Nature **386**, 54 (1997).

[17] A. Maksimchuk, S. Gu, K. Flippo, D. Umstadter, and V. Yu. Bychenkov, *Forward Ion Acceleration in Thin Films Driven by a High-Intensity Laser*, Phys. Rev. Lett. **84**, 4108 (2000).

[18] T. Ditmire *et al.*, *Nuclear Fusion from Explosions of Femtosecond Laser-Heated Deuterium Clusters* Nature **398**, 489 (1999).

[19] V. Yu. Bychenkov, V. T. Tichonchuk, and S. V. Tolokonnikov, *Nuclear reactions triggered by laser-accelerated high-energy ions*, JETP **88**, 1137 (1999).

[20] P. A. Norreys *et al.*, *Neutron production from picosecond laser irradiation of deuterated targets at intensities of* 10^{19} $W\ cm^{-2}$, Plasma Phys. Control. Fusion **40**, 175 (1998).

[21] G. Pretzler, A. Saemann, A. Pukhov, D. Rudolph, T. Schtz, U. Schramm, P. Thirolf, D. Habs, K. Eidmann, G. D. Tsakiris, J. Meyer-ter-Vehn, and K. J. Witte, *Neutron production by 200 mJ ultrashort laser pulses*, Phys. Rev. E **58**, 1165 (1998).

[22] A. McPherson *et al.*,*Multiphoton-Induced X-ray Emission at 4-5 keV from Xe Atoms with Multiple Core Vacancies*, Nature **370**, 631 (1994).

[23] P. A. Norreys, M. Zepf, S. Moustaizis, A. P. Fews, J. Zhang, P. Lee, M. Bakarezos, C. N. Danson, A.Dyson, P. Gibbon, P. Loukakos, D. Neely, F. N. Walsh, J. S. Wark, and A. E. Dangor, *Efficient extreme UV harmonics generated from picosecond laser pulse interactions with solid targets*, Phys. Rev. Lett. **76**, 1832 (1996).

[24] S. V. Bulanov, N. M. Naumovs, and F. Pegoraro, *Interaction of an ultrashort, relativistically strong laser pulse with an overdense plasma*, Phys. Plasmas **1**, 745 (1994).

[25] R. Lichters, J. Meyer-ter-Vehn, and A. Pukhov, *Short-pulse laser harmonics from oscillating plasma surfaces driven at relativistic intensity*, Phys. Plasmas **3**, 3425 (1996).

[26] M. Tabak, J. Hammer, M. E. Glinski, W. L. Kruer, S. C. Wilks, and R. J. Mason, *Ignition and high gain with ultrapowerful lasers*, Phys. PLasmas **1**, 1626 (1994).

[27] E. P. Liang, Scott C. Wilks, and Max Tabak, *Pair Production by Ultraintense Lasers*, Phys. Rev. Lett. **81**, 4887 (1998).

[28] J. Kane, D. Arnett, B. A. Remington, S. G. Glendinning, G. Bazan, R. P. Drake, B. A. Fryxell, R. Teyssier, and K. Moore, *Scaling supernova hydrodynamics to the laboratory*, Phys. Plasmas **6**, 2065 (1999).

[29] D. R. Farley, K. G. Estabrook, S. G. Glendinning, S. H. Glenzer, B. A. Remington, K. Shigemori, J. M. Stone, R. J. Wallace, G. B. Zimmerman, and J. A. Harte1, *Radiative Jet Experiments of Astrophysical Interest Using Intense Lasers*, Phys. Rev. Lett. **83**, 1982 (1999).

[30] F. J. Rogers and C. A. Iglesias, *Astrophysical Opacity*, Science **263**, 50 (1994).

[31] C. Itzykson and J. B. Zuber, *Quantum field theory*, McGraw-Hill, ISBN: 0-07-032071-3, (1980).

[32] G. A. Askar'yan, *Effect of the gradient of a strong electromagnetic beam on electrons and atoms*, Sov. Phys. JETP **15**, 8 (1962).

[33] A. Pukhov and J. Meyer-ter-Vehn, *Relativistic Magnetic Self-Channeling of Light in Near-Critical Plasma: Three-Dimensional Particle-in-Cell Simulation*, Phys. Rev. Lett. **76**, 3975 (1996).

[34] C. Max *et al.*, *Self-Modulation and Self-Focusing of Electromagnetic Waves in Plasmas*, Phys. Rev. Lett. **33**, 209 (1974).

[35] L. Chen and R. N. Sudan, *Necessary and sufficient conditions for self-focusing of short ultraintense laser pulse in underdense plasma*, Phys. Rev. Lett. **70**, 2082 (1993).

[36] S. V. Bulanov, F. Pegoraro, and A. M. Pukhov, *Two-Dimensional Regimes of Self-Focusing, Wake Field Generation, and Induced Focusing of a Short Intense Laser Pulse in an Underdense Plasma*, Phys. Rev. Lett. **74**, 710 (1995).

[37] B. Quesnel, P. Mora, J. C. Adam, S. Guerin, A. Heron, and G. Laval, *Electron Parametric Instabilities of Ultraintense Short Laser Pulses Propagating in Plasma*, Phys. Rev. Lett. **78**, 2132 (1997).

[38] J. C. Adam, S. Guerin, G. Laval, P. Mora, and B. Quesnel, *Anomalous Absorption of Very High-Intensity Laser Pulses Propagating through Moderately Dense Plasma*, Phys. Rev. Lett. **78**, 4765 (1997).

[39] T. M. Antonson, Jr. and P. Mora, *Self-focusing and Raman scattering of laser pulses in tenuous plasmas*, Phys. Rev. Lett. **69**, 2204 (1992).

[40] N. E. Andreev *et al.*, *Resonant excitation of wakefields by a laser pulse in a plasma*, JETP Lett. **55**, 571 (1992).

[41] A. S. Sakharov and V. I. Kirsanov, *Theory of Raman scattering for a short ultrastrong laser pulse in a rarefied plasma*, Phys. Rev. E **49**, 3274 (1994).

[42] W. B. Mori, C. D. Decker, D. E. Hinkel, T. Katsouleas,*Raman forward scattering of short-pulse high-intensity lasers*, Phys. Rev. Lett. **72**, 1482 (1994).

[43] E. Esarey, J. Krall, and P. Sprangle, *Envelope Analysis of Intense Laser Pulse Self-Modulation in Plasmas*, Phys. Rev. Lett **72**, 2887 (1994).

[44] W. L. Kruer, *The Physics of Laser Plasma Interactions*, Addision-Wesley, New-York, ISBN: 0-201-15672-5, 78 (1988).

[45] N. Nakajima, D. Fisher, T. Kawakubo, H. Nakanishi, A. Ogata, Y. Kato, Y. Kitagawa, R. Kodama, K. Mima, H. Shiraga, K. Suzuki, K. Yamanka, T. Zhang, Y. Sakawa, T. Shoji, Y. Nishida, N. Yugami, M. Downer, and T. Tajima, *Observation of Ultrahigh Gradient Electron Acceleration by Self-Modulated Intense Short Laser pulse*, Phys. Rev. Lett. **74**, 4428 (1995).

[46] A. Modena, Z. Najmudin, A. E. Dangor, C. E. Clayton, K. A. Marsh, C. Joshi, V. Malka, C. B. Darrow, C. Danson, D. Neely, and F. N. Walsh, *Electron acceleration from the breaking of relativistic plasma waves*, Nature **377**, 606 (1995).

[47] D. Umstadter, S.-Y. Chen, A. Maksimchuk, G. Mourou, and R. Wagner, *Nonlinear Optics in Relativistic Plasmas and Laser Wake Field Acceleration of Electrons*, Science **273**, 472 (1996).

[48] L. Gorbunov, P. Mora, and T. M. Antonsen, Jr., *Magnetic Field of Plasma Wake Driven by Laser Pulse*, Phys. Rev. Lett. **76**, 2495 (1996).

[49] S. V. Bulanov, M. Lontano, T. Zh. Esirkepov, F. Pegoraro, and A. M. Pukhov, *Electron Vortices Produced by Ultrashort Laser Pulses*, Phys. Rev. Lett. **76**, 3562 (1996).

[50] A. Pukhov and J. Meyer-ter-Vehn, *Laser Hole Boring into Overdense Plasma and Relativistic Electron Currents for Fast Ignition of ICF Tragets*, Phys. Rev. Lett. **79**, 2686 (1997).

[51] S. C. Wilks, W. L. Kruer, M. Tabak, and A. B. Langdon, *Absorption of Ultra-Intense Laser Pulses*, Phy. Rev. Lett. **69**, 1383 (1992).

[52] D. F. Price, R. M. More, R. S. Walling, G. Guethlein, R. L. Shepherd, R. E. Stewart, and W. E. White, *Absorption of ultrashort laser pulses by solid targets heated rapidly to temperatures 1-1000 eV*, Phys. Rev. Lett. **75**, 252 (1995).

[53] W. Rozmus, R. Cauble, and V. T. Tikhonchuk, *A model of ultrashort laser pulse absorption in solid targets*, Phys. Plasmas **3**, 360 (1996).

[54] T. Feurer, W. Theobald, R. Sauerbrey, I. Uschmann, D. Altenbernd, U. Teubner, P. Gibbon, E. Förster, G. Malka, and J. L. Miquel, *Onset of diffuse reflectivity and fast electron current flux inhibition in 528-nm-laser-solid interactions at ultrahigh intensities*, Phys. Rev. E **56**, 4608, (1997).

[55] V. L. Ginzburg, *The propagation of Electromagnetic waves in Plasmas*, Pergamon Press, New York (1984).

[56] P. Mulser, *Resonance absorption and ponderomotive action*, Handbook of Plasma Physics **3**, North Holland, 435 (1991).

[57] A. Bergmann *at al.*, *Resonance Absorption by Nonlinear Electron Plasma Waves*, Europhys. Lett. **14**, 661 (1991).

[58] H. Ruhl and P. Mulser, *Relativistic Vlasov simulation of intense fs laser pulse-matter interaction*, Phys. Lett. A **205**, 388 (1995).

[59] F. Brunel, *Not-so-resonant, resonant absorption*, Phys. Rev. Lett **59**, 52 (1987).

[60] F. Brunel, *Anomalous absorption of high intensity subpicosecond laser pulses*, Phys. Fluids **31**, 2714 (1988).

[61] Paul Gibbon and A. R. Bell, *Collisionless absorption in sharp-edged plasmas*, Phys. Rev. Lett. **68**, 1535 (1992).

[62] E. S. Weibel, *Anomalous Skin Effect in a Plasma*, Phys. Fluids **10**, 741 (1967).

[63] W. L. Kruer and K. G. Estabrook, *J B heating by very intense laser light*, Phys. Fluids **28**, 430 (1985).

[64] R. N. Sudan, *Mechanism for the Generation of* $10^9 G$ *Magnetic Fields in the Interaction of Ultraintense Short Laser Pulse with an Overdense Plasma Traget*, Phys. Rev. Lett. **70**, 3075 (1993).

[65] V. I. Berezhiani, S. M. Mahajan, N. L. Shatashvili, *Theory of magnetic field genereation by relativistically strong laser radiation*, Phys. Rev. E **55**, 995 (1997).

[66] J. M. Wallace, J. U. Brackbill, C. W. Cranfill, D. W. Forslund, and R. J. Mason, *Collisional effcts on the Weibel instability*, Phys. Fluids **30**, 1085 (1987).

[67] K. Satou and T. Okada, *Self-Generated Magnetic Fields in Laser-Produced Plasmas with 3-D Particle-in-Cell Simulation*, Jpn. J. of Appl. Phys. **36**, 365 (1997).

[68] F. Pegoraro, S. V. Bulanov, F. Califano, and M. Lontano, *Nonlinear development of the weibel instability and magnetic field generation in collisionless plasmas*, Physica Scripta **T63**, 262 (1996).

[69] G. Kalman, C. Montes, and D. Quemada, *Anisotropic Temperature Plasma Instabilities*, Phys. Fluids **11**, 1797 (1968).

[70] S. R. De Groot, W. A. van Leeuwen, and Ch. G. van Weert, *Relativistic Kinetic Theory-Principles and Applications*, North Holland Publishing Company, ISBN: 0 444 85453 3, 22 (1980).

[71] J. D. Bjorken and S. D. Drell, *Relativistische Quantenmechanik*, Bibliographisches Institut Mannheim/Wien/Zürich, ISBN: 3-411-0098-8, 117 (1987).

[72] B. Trubnikov, *Review of Plasma Physics I*, Consultant Bureau, New York (1965).

[73] C. K. Li and R. D. Petrasso, *Stopping of directed energetic electrons in high-temperature hydrogenic plasmas*, Phys. Rev. E **70**, 067401 (2004).

[74] T. Takizuka and H. Abe, *A binary collision model for plasma simulation with a particle code*, J. Comput. Phys. **25**, 205 (1977).

[75] S. Ma, R. D. Sydora, and J. M. Dawson, *Binary collision model in gyrokinetic simulation plasma*, Comput. Phys. Commun. **77**, 190 (1993).

[76] D. Kremp, T. Bornath, M. Bonitz, and M. Schlanges, *Quantum kinetic theory of plasmas in strong laser fields*, Physical Review E bf 60, 4725 (1999).

[77] T. Bornath, M. Schlanges, P. Hilse, and D. Kremp, *Nonlinear collisional absorption in dense plasmas*, Physical Review E bf 64, 026414 (2001).

[78] D. O. Gericke and M. Schlanges, *Beam-plasma coupling effects on the stopping power of dense plasmas*, Physical Review E bf 60, 904 (1999).

[79] R. L. Morse and C. W. Nielson, *Numerical Simulation of the Weibel Instability in One and Two Dimensions*, Phys. Fluids **14**, (1971).

[80] J. Villasensor and O. Buneman, *Rigorous Charge Conservation for Local Electromagnetic Field Solvers*, Comp. Phys. Comm. **69**, 306 (1992).

[81] V. A. Vshivkov, M. A. Kraeva, and V. E. Malyshkin, *Parallel Implementation of the Particle-In-Cell Method*, Programming and Computer Software **23**, 87 (1997).

[82] A. B. Langdon, *On enforcing Gauss's law in electromagnetic Particle-In-Cell codes*, Comput. Phys. Comm. **70**, 447 (1992).

[83] B. Marder, *A method for incorporating Gauss's law into electromagnetic PIC codes*, J. Comput. Phys. **68**, 48 (1987).

[84] C. K. Birdsall and A. B. Langdon, *Plasma Physics via Computer Simulation*, Institute of Physics Publishing Bristol and Philadelphia, ISBN: 0-7503-0117-1, 356 (1995).

[85] W. K. H. Panofsky and M. Philips, *Classical Electricity and Magnetism*, Addison-Wesley, Reading, MA, (1962).

[86] E. N. Parker, *Cosmical magnetic fields, their origin and activity*, ISBN 0-19-851290-2, Clarendon Press, Oxford, (1979)

[87] M. Abramowitz and I. A. Stegun, *Handbook of mathematical functions*, ISBN 486-61272-4, Dover Publications, Inc., New York, (1972).

[88] V. Malka, E. De Wispelaere, F. Amiranoff, S. Baton, R. Bonadio, C. Coulaud, R. Haroutunian, A. Modena, D. Puissant, C. Stenz, S. Hüller, and M. Casanova, *Channel Formation in Long Laser Pulse Interaction with a Helium Gas Jet*, Phys. Rev. Lett. **79**, 2053 (1997).

[89] V. Malka, J. Fuchs, F. Amiranoff, S. D. Baton, R. Gaillard, J. L. Miquel, H. Pepin, C. Rousseaux, G. Bonnaud, M. Busquet, and L. Lours, *Suprathermal Electron Generation and Channel Formation by Ultrarelativistic Laser Pulse in Underdense Preformed Plasma*, Phys. Rev. Lett. **79**, 2979 (1997).

[90] P. Sprangle, E. Esarey, and A. Ting, *Nonlinear interaction of intense laser pulses in plasmas*, Phys. Rev. **A 41**, 4463 (1990).

[91] E. Esarey, A. Ting, P. Sprangle, D. Umstadter, and X. Liu, *Nonlinear Analysis of Relativistic Harmonic Generation by Intense Lasers in Plasmas*, IEEE Transactions on Plasma Science **21**, 95 (1993).

[92] P. Gibbon, *High-Order Harmonic Generation in Plasmas*, IEEE J. of Quantum Electronics **33**, 1915 (1997).

[93] J. Fuchs, G. Malka, J. C. Adam, F. Amiranoff, S. D. Baton, N. Blanchot, A. Heron, G. Laval, J. L. Miquel, P. Mora, H. Pepin, and C. Rousseaux, *Dynamics of Subpicosecond Relativistic Laser Pulse Self-Channeling in Underdense Preformed Plasma*, Phys. Rev. Lett, **80**, 1658 (1998).

[94] M. Borghesi, A. J. MacKinnon, L. Barringer, R. Gaillard, L. A. Gizzi, C. Meyer, O. Willi, A. Pukhov, and J. Meyer-ter-Vehn, *Relativistic Channeling of a Picosecond Laser Pulse in a Near-Critical Preformed Plasma*, Phys. Rev. Lett. **78**, 879 (1997).

[95] P. Gibbon, P. Monot, T. Auguste, and G. Mainfray, *Measurable signatures of relativistic self-focusing in underdense plasmas*, Phys. Plasmas **2**, 1305 (1995).

[96] J. A. Stamper, *Review on spontaneous magnetic fields in laser-produced plasmas: Phenomena and measurements*, Laser and Particle Beams **9**, 841 (1991).

[97] R. Fedosejevs, X. F. Wang, and G. D. Tsakiris, *Onset of relativistic self-focusing in high density gas jet targets*, Phys. Rev. **E 56**, 4615 (1997).

[98] W. B. Mori, C. D. Decker, D. E. Hinkel, and T. Katsouleas, *Raman Forward Scattering of Short-Pulse High-Intesity Lasers*, Phys. Rev. Lett. **72**, 1482 (1994).

[99] G. Shvets and J. S. Wurtele, *Instabilities of Short-Pulse Laser Propagation through Plasma Channels*, Phys. Rev. Lett. **73**, 3540 (1994).

[100] E. Esarey, P. Sprangle, J. Krall, and A Ting, *Self-Focusing and Guiding of Short Laser Pulses in Ionizing Gases and Plasmas*, IEEE J. of Quantum Electronics **33**, 1879 (1997).

[101] W. B. Mori, *The Physics of Nonlinear Optics of Plasmas at Relativistic Intensities for Short-Pulse Lasers*, IEEE J. of Quantum Electronics **33**, 1943 (1997).

[102] C. I. Moore, A. Ting, K. Krushelnick, E. Esarey, R. F. Hubbard, B. Hafizi, H. R. Burris, C. Manka, and P. Sprangle, *Electron Trapping in Self-Modulated Laser Wakefields by Raman Backscatter*, Phys. Rev. Lett. **79**, 3909 (1997).

[103] J. Krall, A. Ting, E. Esarey, and P. Sprangle, *Enhanced acceleration in self-modulated-laser wake-field accelerator*, Phys. Rev. **E 48**, 2157 (1993).

[104] C. D. Decker, W. B. Mori, and T. Katsouleas, *Particle-in-Cell simulation of Raman forward scattering from short-pulse high-intensity lasers*, Phys. Rev. **E 50**, 3338 (1994).

[105] S. Wilks, P. E. Young, J. Hammer, M. Tabak, and W. L. Kruer, *Spreading of Intense Laser Beams Due to Filamentation*, Phys. Rev. Lett **73**, 2994 (1994).

[106] P. K. Tien, J. P. Gordon, and J. R. Whinnery, *Focusing of a Light Beam of Gaussian Field Distribution in Continuous and Periodic Lens-Like Media*, Proc. IEEE **53**, 129 (1965).

[107] I. B. Bernstein, *Geometric optics in space- and time-varying plasmas*, Phys. Fluids **18**, 320 (1975).

[108] G-Z. Sun, E. Ott, Y. C. Lee, and P. Guzdar, *Self-focusing of short intense pulses in plasmas*, Phys. Fluids **30**, 526 (1987).

[109] E. E. Fill, *Focusing limits of ultrashort laser pulses: analytical theory*, J. Opt. Soc. Am. **B 11**, 2214 (1994).

[110] P. Sprangle, E. Esarey, and J Krall, *Laser driven electron acceleration in vacuum, gases, and plasmas*, Phys. Plasmas **3**, 2183 (1996).

[111] M. Lontano, G. Lampis, A. V. Kim, and A. M. Sergeev, *Intense Laser Pulse Dynamics in Dense Gases*, Physica Scripta **T63**, 147 (1996).

[112] V. K. Tripathi and C. S. Liu, *Self-generated magnetic field in an amplitude modulated laser filament in a plasma*, Phys. Plasmas **1**, 990 (1994).

[113] L. Gorbunov, P. Mora, and T. M. Antonsen, Jr., *Quasistatic magnetic field generated by a short laser pulse in an underdense plasma*, Phys. Plasmas **4**, 4358 (1997).

[114] T.J.M. Boyd, G. A. Coutts, and D. C. Marks, *Filamentation in magnetized plasma*, Phys. Fluids **30**, 533 (1987).

[115] J. Yoshii, C. H. Lai, T. Katsouleas, C. Joshi, and W. B. Mori, *Radiation from Cerenkov Wakes in a Magnetized Plasma*, Phys. Rev. Lett. **79**, 4194 (1997).

[116] R. J. Mason and M. Tabak, *Magnetic Field Generation in High-Intensity-Laser-Matter Interactions*, Phys. Rev. Lett. **80**, 524 (1998).

[117] H. Ruhl, *Electron jets produced by ultrashort laser pulses*, J. Opt. Soc. Am. B 13, 388 (1996)

[118] H. Ruhl, *Uphill acceleration of electrons and secular fields in laser produced plasmas*, Phys. Plasmas **3**, 3129 (1996).

[119] Paul Gibbon, *Efficient production of fast electrons from femtosecond laser interaction with solid targets*, Phys. Rev. Lett. **73**, 664 (1994).

[120] T.-Y. Brian Yang, William L. Kruer, A. Bruce Langdon, and Tudor W. Johnston, *Mechanisms for collisionless absorption of light waves obliquely incident on overdense plasmas with steep density gradients*, Phys. Plasmas **3**, 2702 (1996).

[121] A. Bourdier, *Oblique incidence of a strong electromagnetic wave on a cold inhomogeneous electron plasma. Relativistic effects*, Phys. Fluids **26**, 1804 (1983).